Performing Heavy Transfers for Offshore Wind Maintenance

by

Marius-Liviu Bălan

A thesis submitted to the University of Strathclyde

for the degree of

Master of Philosophy

Department of Design, Manufacture and Engineering Management

University of Strathclyde

Glasgow, UK

Declaration

This thesis is the result of the author's original research. It has been composed by the author and has not been previously submitted for examination which has led to the award of a degree.

Signed:  Date: 05/08/2023

Acknowledgements

I would like to start by expressing my sincere appreciation to my supervisors Prof. Paul Blackwell and Dr. Dorothy Evans for their support and guidance throughout my studies which led me to completing this thesis. Moreover, I am extremely grateful to my industrial mentors, Prof. Michael Grimble and Dr. Pawel Majecki, for their valuable technical expertise in answering the challenging questions posed by my research. Their insightful knowledge and advice not only helped me to progress through difficult times, but also enabled me to set a solid foundation of transferable skills, for which I am truly indebted.

I would also like to extend my sincere thanks to Industrial System and Control Ltd and their managing director Dr. Andrew Clegg, for welcoming me to their team. Working alongside them has had a great impact on my studies and shaped my career outlook as an engineering professional.

Lastly, my academic journey was supported by the EU INTERREG VA Programme, as well as the Department for the Economy in Northern Ireland and the Department of Enterprise, Trade and Employment in Republic of Ireland.

Publication

M. Balan, P. Majecki, M. Grimble and P. Blackwell, "Multiple Degrees of Freedom Active Motion Control of a Hydraulically Actuated Crane," OCEANS 2021: San Diego – Porto, 2021, pp. 1-6, doi: 10.23919/OCEANS44145.2021.9705747.

Abstract

As offshore wind farms become larger and further from the shore, there are strong economic and climate incentives to perform transfers required for operations and maintenance from floating vessels, rather than employing expensive and slow jack up rigs. However, successful transfers of heavy and sensitive equipment from a floating vessel (in all but benign sea/wind conditions) are heavily dependent on multiple degrees of freedom, high performance control.

This project aims to bring a novel modelling and simulation methodology in Simulink that could be used to assess offshore wind installation and maintenance procedures. More specifically, the goal is to demonstrate that a crane prototype assumed to be located on a floating ship can transfer loads of hundreds of tons onto a fixed platform. Furthermore, this process should be completed with good precision and minimal impact force during equipment loading onto the stand. This problem has not yet been answered in research, with the only relevant patent in the field being the Ampelmann platform, a motionless bridge allowing technicians to access the offshore turbine.

The first main contribution to knowledge of this thesis was the design of a 90 m crane that could handle a 660 tons load. This thesis presents a procedure, based on both mechanical/hydraulics design as well as empirical findings, which could be re-used for scaling the crane model to a more realistic dimension. It is worth noting that the goal here was to assess whether a realistically weighing piece of equipment could be stably handled, while the actual size of the crane was deemed unimportant.

Another missing gap in literature this project wanted to fill was achieving active motion compensation for a larger scale system such as the current one. This refers to balancing out the base motions on multiple axes, so the payload can be moved on a given trajectory unaffected by them. Currently, research in the field mainly consists of crane mechanisms that feature active heave compensation, which only refers to the vertical axis. Hence, two control design methods were employed to assess the viability of heavy payload positioning from floating vessels through the development of a simulation approach using Simulink. The crane prototype was designed and modelled to operate under simulated vessel motions given by sea states with a significant wave height of 5 m and maximum wave frequency of 1 rad/s. Then, traditional control (feedback and feedforward) was designed to achieve active motion compensation with steady-state position

errors under 20 cm. A second controller architecture was then designed/implemented as a comparison basis for the first one, with the aim being to find the most robust solution of the two. The nonlinear generalised minimum variance (NGMV) control algorithm was chosen for control design in this application. Due to its ability to compensate for significant system nonlinearities and the ease of implementation, NGMV was a good candidate for the task at hand. Tuning controller parameters to stabilize the system could also be based on the previously determined traditional control solutions.

An investigation of controllers' robustness against model mismatch was carried out by introducing various levels of uncertainty which influence actuators' natural frequency to assess system sensitivity. The outcome of the investigation determined that traditional and NGMV controllers provided comparable regulating performance in terms of reference tracking and disturbance rejection, for the nominal case. This confirmed the assertion that the PID-based NGMV weightings selection is a useful starting point for controller tuning. Increasing the mismatch between the nominal system based on which the controllers' were designed and the actual plant showed that the traditional control was marginally more robust in this application.

The final contribution to knowledge this thesis aimed to bring was minimising the impact force during load placement on a fixed and rigid platform. To that end, the contact forces between the payload and a platform were first successfully modelled and measured. A switching algorithm between position and force control was then developed based on a methodology found in literature but on a microscopic scale project. To execute smooth load placement, an automated hybrid force/position control scheme was implemented. The proposed algorithm enabled position control on x and y axes, while minimising impact forces on the z-axis. Unfortunately, preliminary findings showed that there is still work to be done to claim any success in this regard. However, the author hopes this offers a good starting point for future work.

TABLE OF CONTENTS

Table of Contents i

Table of Figures v

Table of Tables ix

1. Chapter 1: Introduction 1

1.1. Overview 1

1.2. Wind Energy 1

1.3. Operation and Maintenance 5

1.3.1. Accessibility against availability 7

1.3.2. Accessibility relative to sea level 8

1.4. Offshore Accessibility 9

1.4.1. Motion Compensation 9

1.4.2. Six Degrees of Freedom Active Motion Compensation 12

1.4.3. Service Operation Vessels 13

1.5. Research Aim and Objectives 13

1.6. Thesis Approach 15

2. Chapter 2: Modelling Waves and Ship Motions 17

2.1. Wave Modelling 17

2.1.1. Sea State Definition 17

2.1.2. Wave Spectrum 20

2.2. Vessel Motions 20
2.2.1. Reference Frames 20
2.2.2. Vessel response 22
2.3. Ship Platform Motion Modelling 24
2.4. Chapter Summary 26
3. Chapter 3: Crane Design and Modelling 28
3.1. Introduction 28
3.1.1. Serial Manipulator 28
3.1.2. Parallel manipulator 30
3.2. Crane System Description 34
3.3. Hydraulic Actuator Design 35
3.3.1. Description 35
3.3.2. Cylinder Sizing 38
3.4. Crane Kinematics 40
3.4.1. Introduction 40
3.4.2. Forward and Inverse Kinematics Implementation 43
3.5. Crane Dynamics 44
3.6. Chapter Summary 46
4. Chapter 4: Motion Control Design 48
4.1. Traditional Control 49

4.1.1. Introduction to Feedback and Feedforward Control 49

4.1.2. Design of Traditional Control 52

4.2. Advanced Control 54

4.2.1. Introduction 54

4.2.2. NGMV Control 60

4.3. Payload Position Control Results 70

4.3.1. Preliminary Results – Nominal Case 70

4.3.2. Mismatch Level 10% 74

4.3.3. Mismatch Level 20 % 77

4.3.4. Mismatch Level 40% 79

4.3.5. Analysing the Results 83

4.4. Chapter Summary 86

5. Chapter 5: Load Placement Modelling and Control 88

5.1. Introduction 88

5.1.1. Contact Force Modelling 88

5.1.2. Contact Force Control 92

5.2. Load Placement 92

5.3. Hybrid Motion to Contact Force Control 96

5.4. Summary 99

6. Chapter 6: Discussion 100

6.1. Sea State and Vessel Motions Modelling 100

6.2. Hydraulic Crane Design 100

6.3. Motion Control Design 101

6.4. Hybrid Motion/Force Control 102

6.5. Summary 102

7. Chapter 7: Conclusions 104

References 107

Appendix I

TABLE OF FIGURES

Figure 1.1: Levelised Cost of Electricity of major power generation technologies in Europe, 2018 2

Figure 1.2: Carbon emissions due to O&M of an offshore wind turbine..... 6

Figure 1.3: Relationship between wind farm availability and accessibility (van Bussel and Bierbooms, 2003)..... 7

Figure 1.4: Floating vessel motions: 3 translations and 3 rotations..... 9

Figure 1.5: Simplified diagram of an active heave compensation system..... 10

Figure 1.6: Left- Diagram of Ampelmann system mounted on a floating ship. Right- Stewart platform and its main components..... 12

Figure 1.7: Research approach and structure of the thesis..... 16

Figure 2.1: Diagram describing the procedure to simulate wave induced vessel motions in 6 Degrees of Freedom (DoF)..... 17

Figure 2.2: Sea surface with long-crested waves (Left) and Sea surface with short-crested waves (Right) (Anil et al., 2017)..... 18

Figure 2.3: JONSWAP and Pierson-Moskowitz wave spectra..... 20

Figure 2.4: Notation and sign convention of reference frames for ship motion description (David Salzmann, 2010)..... 21

Figure 2.5: Marine system components..... 24

Figure 2.6: Sea state realization and its corresponding JONSWAP spectrum..... 26

Figure 2.7 Six degrees-of-freedom vessel motion response..... 26

Figure 3.1: Diagram of a serial manipulator and four common types of joints..... 28

Figure 3.2: Diagram showing the work envelope of a generic robot arm gripper 30

Figure 3.3: Diagram of a Stewart platform arrangement 31

Figure 3.4: Real-life scenario is presented on the left and a simplified Simulink representation of the hydraulic crane is displayed on the right..... 34

Figure 3.5: Diagram of a hydraulic actuator 36

Figure 3.6: Coordinate frame assignment for general manipulators. (a) Position and orientation of two successive links are specified by two joint parameters. (b) Position and orientation between two successive joints are specified by two link parameters 41

Figure 3.7: Tree representation for the hydraulic crane showing the connectivity between its links and joints..... 43

Figure 4.1: High-level diagram consisting of the main components comprised in the control architecture of the crane system..... 48

Figure 4.2: Diagram of PID with double derivative control 49

Figure 4.3: Diagram of a feedback and feedforward control system 51

Figure 4.4: Diagram describing the principle of model predictive control 55

Figure 4.5: Basic structure of nonlinear model predictive control..... 57

Figure 4.6: Simplified architecture of the nonlinear generalised minimum variance controller . 58

Figure 4.7: NGMV control loop architecture..... 60

Figure 4.8: Feeback control system for a nonlinear plant model with the reference and disturbance signals 63

Figure 4.9: Joint rotations reference tracking comparison between traditional control and NGMV control 70

Figure 4.10: Joint angles errors comparison between traditional control against NGMV control71

Figure 4.11: Measured payload 3D trajectory relative to the fixed reference frame 71

Figure 4.12: Measured payload motion compared against the expected motion on each of the x, y, and z axes..... 72

Figure 4.13: Errors in reference tracking for each individual joint rotation 74

Figure 4.14: Payload positioning on x-y-z and errors to reference trajectory as a result of the errors in joint rotations tracking from Figure 4.13..... 75

Figure 4.15: Errors in joint rotations reference tracking..... 76

Figure 4.16: Payload positioning on x-y-z and errors to desired trajectory as a result of the errors in joint rotations tracking from Figure 4.15..... 76

Figure 4.17: Errors in each of the four joint angle rotations tracking..... 77

Figure 4.18: Payload positioning on x-y-z and errors to desired trajectory as a result of the errors in joint rotations tracking from Figure 4.17..... 78

Figure 4.19: Errors in each of the four joint angle rotations tracking..... 78

Figure 4.20: Payload positioning on x-y-z and errors to desired trajectory as a result of the errors in joint rotations tracking from Figure 4.19..... 79

Figure 4.21: Errors in each of the four joint angle rotations tracking..... 80

Figure 4.22: Payload positioning on x-y-z and errors to desired trajectory as a result of the errors in joint rotations tracking from Figure 4.21..... 80

Figure 4.23: Errors in each of the four joint angle rotations tracking..... 81

Figure 4.24: Payload positioning on x-y-z and errors to desired trajectory as a result of the errors in joint rotations tracking from Figure 4.23..... 81

Figure 4.25: Plotted root mean square errors for joints rotations and resulting payload trajectory on x-y-z across 0%, 10%, 20% and 40% mismatch levels 85

Figure 5.1: Generalised diagram describing the spatial contact force 89

Figure 5.2: Depiction of penalty method for contact and friction forces 90

Figure 5.3:Friction coefficient vs the relative tangential velocity near region of contact..... 91

Figure 5.4: Size of the interacting objects (rigid stand and cylindrical load) 93

Figure 5.5: Measuring the contact force between the interacting objects being decoupled from the crane 93

Figure 5.6: Measured contact force between payload and platform given the contact depth and collision velocity. 94

Figure 5.7: Contact force measurement during load placement following a given trajectory and considering active motion compensation 95

Figure 5.8: Block diagram describing the external hybrid motion to force control during load placement 96

Figure 5.9: Diagram showing the components of the enable control block, E 97

Figure 5.10: Block diagram describing incremental control for contact force task 98

Figure 5.11: Normal force between payload and platform during placement with the hybrid motion/force controller 98

TABLE OF TABLES

Table 1.1: Onshore and offshore wind energy- in the past and predictions (IRENA 2019, Executive Summary)..... 4

Table 1.2: Example of a scatter diagram of the yearly sea state distribution at the IJmuiden Munitiestortplaats in the Dutch North Sea (David Salzmann, 2010)..... 8

Table 3.1: Robotic grippers actuation. 29

Table 3.2: Gripper action. 29

Table 3.3: Computed hydraulic cylinder sizes..... 39

Table 3.4: Kinematic parameters for the hydraulic crane 43

Table 4.1: Effects of individual PID controller terms..... 50

Table 4.2: Root mean square error for reference tracking of each joint given in degrees across 0%, 10%, 20% and 40% mismatch levels 83

Table 4.3: Root mean square error for the measured payload trajectory against its reference on x-y-z axes given in meters computed across 0%, 10%, 20% and 40% mismatch levels 84

1. CHAPTER 1: INTRODUCTION

1.1. Overview

This chapter will start with an introduction to the wind energy sector and will cover the need for enabling technologies in offshore wind energy in particular. It will also provide a short overview of competing energy sources and then outline how this project fits into the offshore sector maintenance.

The chapter will then dive into current technologies employed in enhancing offshore wind accessibility. Accessibility to the offshore farms has been demonstrated to result in improved maintenance practices which in turn were shown to reduce costs and carbon emissions.

Thesis contribution to knowledge will be defined later on in the chapter. The goal of the project is to produce a novel modelling and simulation methodology in Simulink that could be used to assess offshore wind installation or maintenance procedures. More specifically, the target is to demonstrate that a crane prototype assumed to be located on a floating ship can transfer loads of hundreds of tons onto a fixed platform. Furthermore, this equipment transfer process should be achieved with good precision and minimal impact force during loading onto the stand. Doing so requires designing robust control techniques. Achieving good performance control over a 90-meter-tall crane prototype holding a 660 tons weight in the given scenario is one of the main contributions of the current research. Similar solutions could not be found in research, with the only relevant patent in the field being the Ampelmann platform, a motionless bridge allowing technicians to access the offshore turbine.

1.2. Wind Energy

In their 2019 annual report ("Renewable Energy Statistics," 2019), International Renewable Energy Agency (IRENA) estimated that renewable energy could supply more than 80% of the global demand and potentially reduce the annual energy-related CO2 emissions by about 75% within 30 years' time.

Costs of renewable energy have continued to decline rapidly; for example, in the case of solar photovoltaic (PV) the global average cost decreased by 73% since 2010 ("Wind energy in Europe in 2018," 2019). In Europe, offshore wind can now compete at market prices, showing its fast growth in the past few years (U.S. Energy Information Administration, 2020).

Because of the continuously increasing demand for green energy, solar and wind sectors were given a significant importance over the past decades. However, the processes behind enabling renewable energy generation cannot be made entirely clean at present moment. Thus, there is also a need for innovative technologies to optimise manufacturing, installation, maintenance, and decommissioning in order to minimise costs and climate impact of renewable sources.

Wind farms are cost-effective energy sources (see Figure 1.1, reproduced from Christoph Kost et al., 2018).

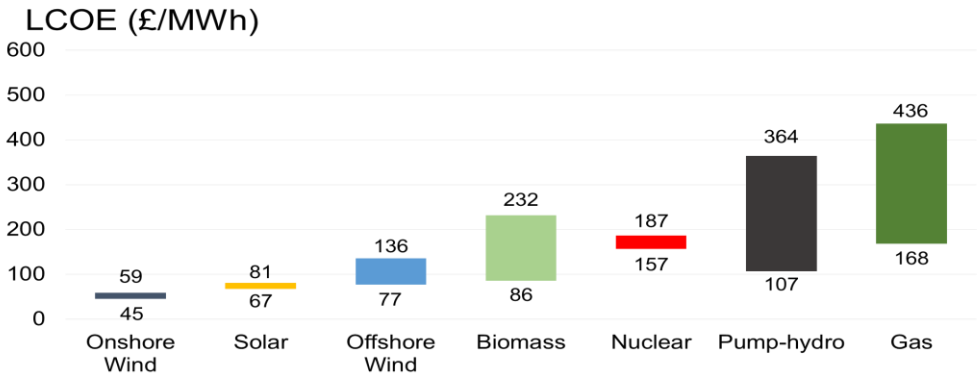

Figure 1.1: Levelised Cost of Electricity of major power generation technologies in Europe, 2018

An explanation for the significant LCOE fluctuations in competing technologies presented in Figure 1.1 is given below:

- Gas energy

LCOE calculation does not include the flexibility of power generation technology or the worth of the generated electricity. For example, the specific seasonal and daily generation of each technology is different. Differences due to the flexible use of power plants or the provision of ancillary services in relation to the market sales price of electricity obtained are not reflected in

the LCOE. Highly flexible gas turbines imply even higher electricity generation costs. They are, however, highly flexible and with fewer than 1000 full load hours/year makes them actually less expensive than other technologies due to their low acquisition costs. (Christoph Kost et al., 2018)

- Pump-hydro energy

For pump-hydro, the levelized cost of storage (LCOS) is equivalent to LCOE for generation technologies and represents an appropriate tool for cost comparison of electricity storage technologies. LCOS quantifies the discounted cost per unit of discharged electricity for a specific storage technology and application. Investment costs make up the largest proportion of LCOS, between 65% and 90% in 2015. Charging cost represents the second largest contributor at 7% to 25% due to the high annual cycle requirement (Schmidt et al., 2019). Therefore, the high difference seen in lower and upper bounds for pump-hydro energy in Figure 1.1 is explained by its high fluctuation in investment and charging costs.

- Biomass energy

Biomass power generation varies significantly by technology and country. The total installed costs of stoker boilers was between 1,495 £/kW and 3,388 £/kW in 2010, while those of circulating fluidised bed boilers were between 1726 £/kW and 3580 £/kW. Anaerobic digester power systems had capital costs between 2044 £/kW and 4851 £/kW. Gasification technologies, including fixed bed and fluidised bed solutions, had total installed capital costs of between 2044 £/kW and 4533 £/kW. Co-firing biomass at low levels in existing thermal plants typically requires additional investments of 318 £/kW up to 477 £/kW. Using landfill gas for power generation has capital costs of between 1527 £/kW and 1940 £/kW. The cost of combined heat and power plants is significantly higher than for the electricity-only configuration ("Renewable Power Generation Costs in 2012 An Overview," 2013).

- Onshore versus offshore wind energy

Moving wind energy generation from onshore to offshore locations comes at a price. The total costs of wind energy can be separated into two types of costs: the investment costs and the operation and maintenance (O&M) costs. The investment costs include the costs of turbine, foundation, grid connection and installation. The O&M costs comprise the costs of regular

maintenance, repairs and spare parts. The investment costs for a wind farm offshore are considerably higher than onshore, mainly due to the required integration with the electrical grid, larger and more complex support structures and expensive installation methods.

Levelised Cost of Electricity (LCOE) in the case of onshore wind farms is predicted to decline further in the next years when compared to fossil fuel generation due to increased performance and installed costs, according to IRENA 2019. In 2018, the global LCOE for onshore farms was 45 GBP/MWh and the prediction for 2050 shows a drop by more than 50%. LCOE of offshore farms is expected to decrease from twice the value of onshore wind LCOE in 2010 to almost an equal value in 2050. An in-depth comparison between onshore and offshore wind energy indicators was tabulated in Table 1.1.

Table 1.1: Onshore and offshore wind energy- in the past and predictions (IRENA 2019, Executive Summary).

	2010	**2018**	**2030**	**2050**
Onshore and offshore wind generation share (%)				
	1.7	6	21	35
Total installed capacity				
Onshore (GW)	178	542	1787	5044
Offshore (GW)	3	23	228	1000
Annual Deployment				
Onshore (GW/year)	30	45	147	2022
Offshore (GW/year)	0.9	4.5	28	45
Total installation cost				
Onshore (USD/kWh)	1913	1497	800 – 1350	650-1000
Offshore (USD/kWh)	4572	4353	1700 – 3200	1400 – 2800
Levelised cost of electricity (LCOE)				
Onshore (USD/kWh)	0.08	0.06	0.03 – 0.05	0.02 – 0.03
Offshore (USD/kWh)	0.16	0.13	0.05 – 0.09	0.03 – 0.07
Average annual investment				
Onshore (USD billion/year)	57	67	146	211
Offshore (USD billion/year)	4.2	19.4	61	100
Capacity factors				
Onshore (%)	27	34	30 – 55	32 – 58
Offshore (%)	38	43	36 – 58	43 – 60

According to Table 1.1, it is evident that offshore farms are more costly than onshore farms, but they can produce more energy as shown by their capacity factor. The capacity factor (CF) is defined as the ratio of the average delivered power to the theoretical maximum power output and is typically higher offshore as a direct result of the higher and constant wind speeds.

Furthermore, due to a wider available surface and steadier wind at sea, offshore wind turbines are built larger in size and thus are able to increase their capacity at a fast rate ("Wind energy in Europe in 2018," 2019). Moving wind farms to offshore sites involves however a larger investment than onshore, because of the required integration with the electrical grid, larger and more complex support structures, and expensive installation methods.

Generally, the total costs of wind energy can be separated into investment costs (expended on turbine foundation, grid connection and installation) and Operation and Maintenance (O&M) costs for regular maintenance, repairs, and spare parts.

According to recent studies, O&M account for around 25% of an offshore wind turbine lifetime cost (Röckmann et al., 2017) and of its carbon emissions (Reimers et al., 2014). Therefore, there is a strong incentive to finding a technical innovation that could reduce the impact of O&M conducted for an offshore wind farm in terms of expenditures and emissions.

1.3. Operation and Maintenance

O&M includes monitoring and repairs performed after a turbine has been commissioned in order to maintain it functioning. There are two types of maintenance, preventive, or corrective. The first category includes planned maintenance (conducted at or during pre-established time intervals) and condition-based maintenance (after detection of a degraded component). Under the second category lies the unplanned maintenance (in case of unexpected failure) (Rademakers et al., 2007). Unplanned maintenance compared to planned maintenance correspond to a 60% - 40% ratio in terms of costs (Rademakers, 2003).

Size and reliability of the turbine, water depth, distance to port, number of turbines in the wind farm, wind and wave climate are all factors that need consideration for minimisation of O&M costs. However, they are accounted for prior to the installation of the farm to optimise the expenditures.

Once the turbines have been put in place, the only factor dictating O&M costs and greenhouse gas (GHG) emissions is accessibility to the wind farm. Research (David Salzmann, 2010) shows that there is a proportional relation between accessibility to wind farm, turbine's availability and expenses minimisation.

Accessibility refers to the means of transport to the wind turbine and the process of transferring technicians and equipment onto the wind turbine. As stated previously, O&M activities contribute more than 20% to the total life cycle carbon emissions impacts of an offshore wind farm, and it is significantly higher than in the case of an onshore farm due to accessibility being more challenging (Thomson and Harrison, 2015). Thus, more in-depth research needs to be done to understand what the main drivers of carbon emissions are.

According to a couple of Life Cycle Assessment studies (Reimers et al., 2014) (Raadal et al., 2014), the largest share of GHG emissions comes from manufacturing and decommissioning (M&D) spare parts (Figure 1.2- reproduced from Reimers et al., 2014). However, the rest of emissions come from two main sources. First, transfers by ship or helicopter contribute 3% (for planned maintenance) and 14% (for unplanned maintenance). Then, the jack-up rigs, used for transferring heavy equipment, account for approximately 33% of CO_2 emissions.

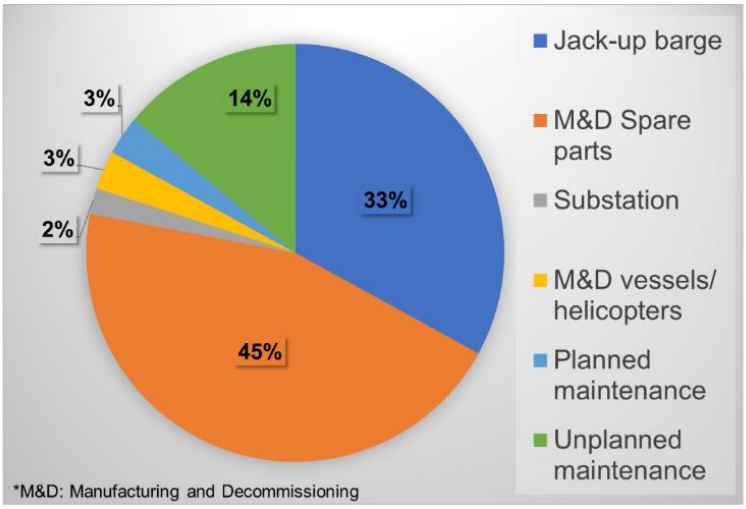

Figure 1.2: Carbon emissions due to O&M of an offshore wind turbine

From Figure 1.2, it is evident that optimising accessibility to the windfarm during maintenance will also lower the GHG emissions. This could mean reducing the time of helicopters use and replacing the slow and expensive jack-up rigs with a more cost-effective and "greener" solution.

The requirements for improved accessibility include of: employing a floating vessel, featuring multiple degrees of freedom (DoF) active motion control and operation in sea states with wave heights of 2.8 m. The solution should not require any special provisions on the turbine (such as landing pads for helicopter access). The explanations for the above statements are provided below.

1.3.1. Accessibility against availability

The availability of a offshore wind farm thus depends largely on the accessibility of the turbines. For a case study farm of 80 turbines located 43 km off the Dutch coast, the Dutch DOWEC project used a sophisticated Monte Carlo simulation model to examine the relationship between a wind farm's accessibility and its resulting availability (van Bussel and Bierbooms, 2003).

The result in Figure 1.3 shows any increase in accessibility up to about 90% results in a direct significant increase in the wind farm's availability. Beyond an accessibility of 90%, the influence on the increase in availability is much smaller. It seems justified to conclude that any increase in accessibility up to approximately 90% directly results in an increase of a turbine's availability,

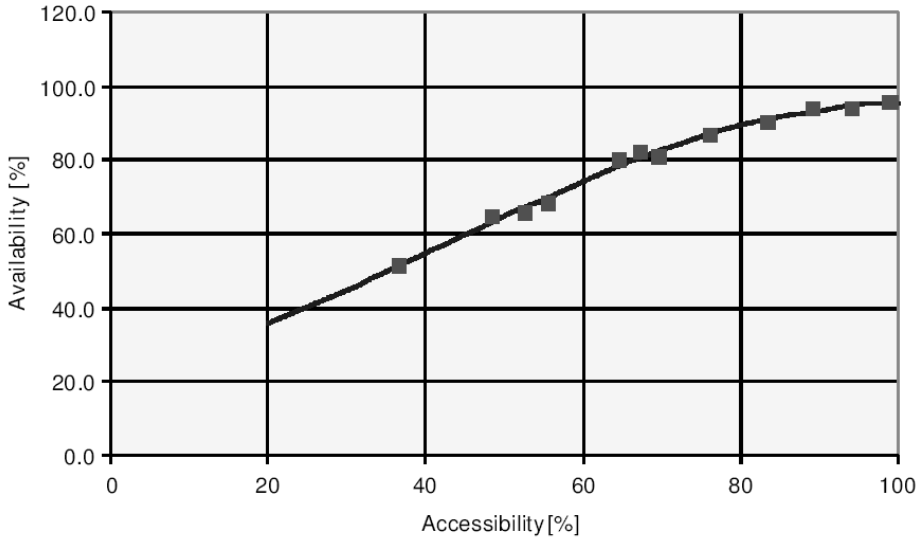

Figure 1.3: Relationship between wind farm availability and accessibility (van Bussel and Bierbooms, 2003)

and thus power delivery and revenue. Therefore, to minimize revenue losses, any maintenance strategy should aim for a high accessibility.

1.3.2. Accessibility relative to sea level

To predict which percentage of time offshore access can be performed safely, the long term distribution of sea states at a given location is required. The long-term distribution of sea states is normally presented in a scatter diagram, which gives the probability of occurrence for combinations of significant wave height H_s and the mean zero-crossing wave period $T(z)$. A scatter diagram can correspond to the yearly, monthly or seasonal distribution of sea states, preferably based on many years of measurements or hindcast data.

The present research considered the Ampelmann study as a starting point where a significant wave height $H(s) = 2.8\,m$ was chosen as a design requirement. Generally, offshore maintenance is carried out at wave heights of 1.5 m. However, the present research is trying to determine whether a model of a crane system could attain acceptable performance at a higher sea level than that, hence the 2.8 m sea state.

The provide the context for the above selection, Table 1.2 is an example of a scatter diagram showing the yearly distribution (given in percentage) of sea states at a typical Dutch offshore location and is based on measurements from 1989 to 2008. The probability of sea states up to any significant wave height in a year can easily be deduced. For example, the cumulative probability of sea states that can rise up to wave height of 2.8 metres equals 95.2%. If access is only allowed in sea states up to a significant wave height of 1.5 metre, the accessibility of a turbine for the given location will theoretically be 68.3% per year.

Table 1.2: Example of a scatter diagram of the yearly sea state distribution at the IJmuiden Munitiestortplaats in the Dutch North Sea (David Salzmann, 2010)

$T_z\,[s]$ / $H(s)[m]$	2 – 3	3 – 4	4 – 5	5 – 6	6 – 7	7 – 8	8 – 9	9 – 10	**Total**
0 – 0.5	1.2	9.4	3.5	0.5	0.1	<0.05	<0.05		**14.6%**
0.5 – 1	0.2	15	11.6	3.2	0.3	<0.05	<0.05		**30.4%**
1 – 1.5		3.8	15.2	3.9	0.4	<0.05			**23.3%**

1.5 – 2		0.1	8.9	5	0.3	<0.05	<0.05		**14.3%**
2 – 2.5			1.7	5.9	0.4	<0.05			**8.1%**
2.5 – 3			0.1	3.6	0.8	<0.05	<0.05		**4.5%**
3 – 3.5			<0.05	1.0	1.3	0.1	<0.05		**2.4%**
3.5 – 4				0.1	1.1	0.1	<0.05		**1.3%**
4 – 4.5				<0.05	0.4	0.2			**0.6%**
4.5 – 5					0.1	0.2	<0.05		**0.3%**
5 – 5.5					<0.05	0.1	<0.05		**0.1%**
5.5 – 6						<0.05	<0.05		**0.1%**
6 – 6.5							<0.05	<0.05	**<0.05%**

1.4. Offshore Accessibility

Work presented in the Ampelmann project (David Salzmann, 2010) has shown that the requirements for a accessing an offshore wind farm during O&M are a self-supporting vessel that can operate under sea states with wave heights of up to 2.8 m with no need for special provisions on the turbines. Safe access can be achieved via active motion compensation systems.

The following subsections will present in detail the most common motion compensation systems existing in industry.

1.4.1. Motion Compensation

The main issue of safe transfers (during maintenance of offshore wind farms) is caused by the relative motions between the moving vessel and a fixed landing point on the offshore structure.

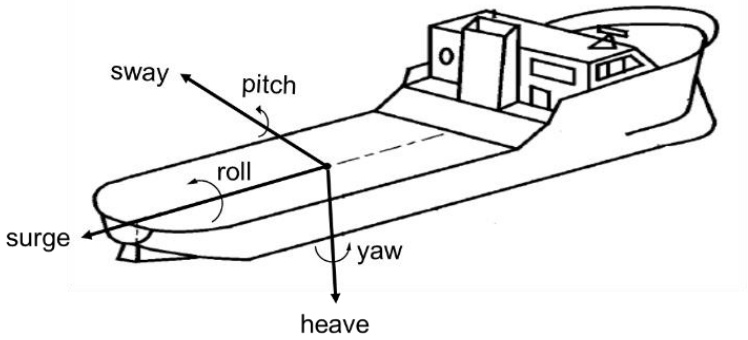

Figure 1.4: Floating vessel motions: 3 translations and 3 rotations

The wave induced ship motions can be described by the six degrees of freedom (DoF) motions that a ship can experience relative to a fixed frame of reference: three translations (surge, sway and heave) and three rotations (roll, pitch and yaw) as shown in Figure 1.4.

Several special cases of ship-based motion compensation platforms and systems are presented below:

1. Active heave compensation (AHC)

AHC controls the vertical motion of a crane (see Figure 1.5) affected by waves forces, by minimising the impact forces on the load attached to the crane through a cable.

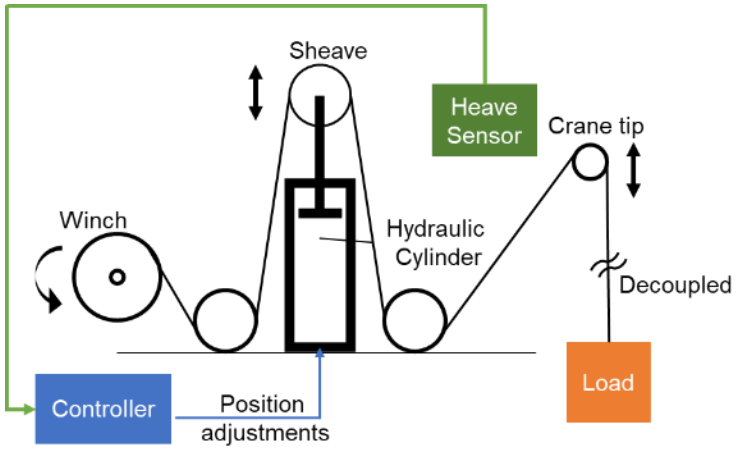

Figure 1.5: Simplified diagram of an active heave compensation system

The crane tip vertical displacement can be measured in real-time with an inertial measurement unit (IMU) consisting of accelerometers and gyroscopes or a GPS (Woodacre et al., 2015). Then, a controller together with a prediction algorithm that identifies peak waves in advance can overcome any delay within the system (Richter et al., 2017) and promptly modify the hydraulic cylinder extension/retraction accordingly. As the cylinder is attached to one of the sheaves the lifting cable is wound on, heave can be compensated for and the load maintains a desired position, being decoupled from any displacement in the crane tip.

2. Stabilization Platforms

Below are listed some relevant patented technologies:

- Gyroscopic stabilisation platforms (Votrubec, 2014) and gyrostabilisers (Poh et al., 2017) are used for reducing roll and pitch motions of marine ships to increase crew comfort and reduce cargo damage. “Motion compensated apparatus” patent (Powell, 1995) is frequently used as a stabilising platform. This technology might be improved through an augmented GPS to provide information to estimate vertical displacement as GPS has low sample rate. However, GPS provide no measurement of angular rates which will induce heave motion unless the platform is located exactly at the ship center-of-gravity. That can be compensated by the existing accelerometers and gyroscopes.

- Bargemaster (Koppert, 2009) is a roll-pitch-heave compensation platform with 3 vertically placed cylinders on spherical joints. Planar movements are constrained by 3 tension beams, with a side effect limiting the maximal extension.

- Helipad (Hovland and Vatn, 2006), (Ying, 2013) or “Helicopter landing pad” can stabilise for roll and/or pitch motions so that the helicopter experiences a smooth landing.

3. Dynamic positioning (DP)

DP control maintains the horizontal position and orientation of a ship (in 3 DoFs: surge, sway and yaw) as thrusters balance the environmental forces caused by wind, waves, and currents. Vessel horizontal control has been extensively studied in the past, such as in these research studies (Grimble et al., 1980), (Balchen et al., 1980) and (Leira et al., 2004).

An alternative to floating boats featuring DP are the jack-up rigs, usually found in offshore industries such as drilling, lifting and subsea installations. They maintain a fixed position by lowering their legs onto the seabed but are limited by water depths that exceed 150 m (e.g. Hyundai, CJ70-150MC jack-up model). Moreover, jack-ups are expensive and come in a limited number on the market (Baldock et al., 2014), which means that the owner of a wind farm is required to book them in advance and for a constrained amount of time. This can be extremely inconvenient especially in case of unplanned maintenance.

1.4.2. Six Degrees of Freedom Active Motion Compensation

Ampelmann system (David Salzmann, 2010) is at the core of state-of-the-art O&M vessels that enable safe transfer of personnel and gear via a motionless bridge. This gangway is supported by a Stewart platform (Figure 1.6, right) fixed on the deck, which allows motion with six degrees of freedom (DoF) due to its six hydraulic cylinders.

Accurate measurements of the ship motions are gathered in real-time by sensors and are converted into control signals that serve as inputs to the Stewart platform. Safe transfers are possible thanks to a fast motion control that compensates for waves effect on the vessel, thus making the transfer deck stationary. A diagram of this patent is presented in Figure 1.6 (left) ("Stewart Platform - MATLAB & Simulink - MathWorks," n.d.).

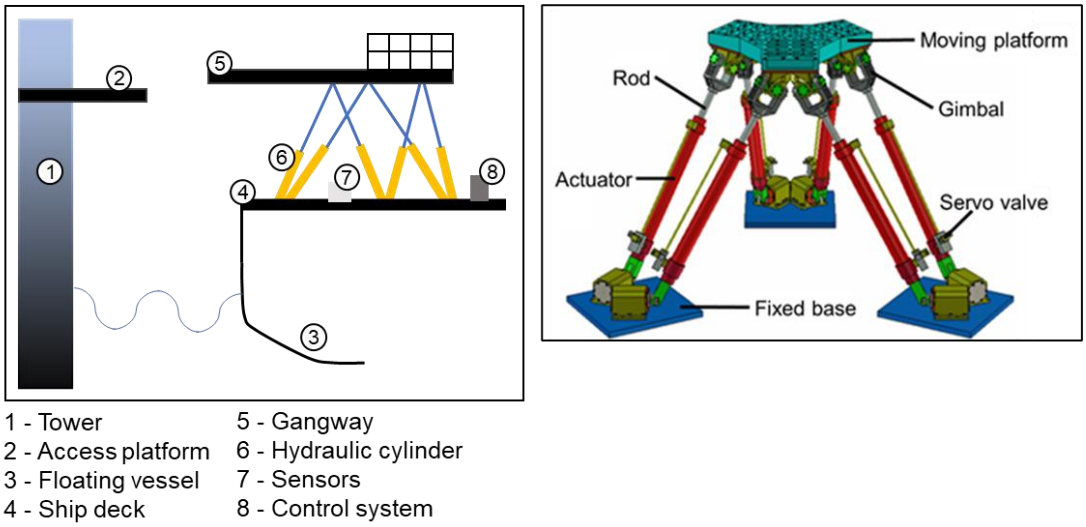

Figure 1.6: Left- Diagram of Ampelmann system mounted on a floating ship. Right- Stewart platform and its main components

Ampelmann technology has proven to be a safe method that facilitated personnel transfer to fixed offshore structures in sea states with a significant wave height of up to 2.8 meters. The system has been commercially available since 2010 and has been utilized in offshore wind, oil, and gas projects.

1.4.3. Service Operation Vessels

Service operation vessels (SOVs) are purpose-built vessels for the deployment and retention of offshore support and maintenance engineers, ranging between 50 - 100 m in length. Generally, an SOV has on-site work and storage facilities plus accommodation for maintenance personnel, management, and a crew for voyages of up to one month. The ship features dynamic positioning control and a motion-compensated transfer bridge to allow maintenance personnel to walk between vessel and offshore structure. SOV uses diesel-electric propulsion system and DC power system that enables optimised fuel/energy efficiency and ultimately has low carbon emissions impact. Some of the producers on the market for this type of vessel are Royal IHC, Esvagt, Ulstein Group and Damen Shipyards.

Research on Ampelmann (David Salzmann, 2010) and related modern technology, however, has not shown that lifts of very heavy and sensitive equipment (in the tens/hundreds of tons range) can be supported by floating vessels. Moreover, residual motions of the transfer deck are allowed in Ampelmann, which in the case of precise handling of large payloads can be detrimental. Therefore, this research will focus on controlling the positioning and placement of such equipment such that its contact with an offshore platform is unaffected by residual motions/forces to avoid any damage.

1.5. Research Aim and Objectives

The goal of this project is to study the viability of performing heavy transfers from floating vessels during offshore wind O&M with the aid of advanced control methods. The entirety of the work is carried out via a simulation approach in Simulink. The additional Simscape toolbox facilitates accurate design of mechanical, hydraulic, and electrical systems along with a visualisation feature that allows thorough examination of design components. Marine System Simulator (MSS) toolbox for Simulink (Perez et al., 2006a) provides the necessary resources for rapid implementation of mathematical models of marine systems.

The project scenario includes a moving ship that supports, on its deck, a hydraulically actuated crane holding a generator/gearbox. Assuming the component was already lifted from the deck (for example, via an active heave compensation system (Shi et al., 2014) and gripped by the

manipulator, the aim is to steadily place the component on a fixed offshore platform located on the turbine.

Real-life tests of the proposed prototype are not part of the scope of this project. Future work could use a validated Simulink model based on the design procedure presented in this thesis to manufacture a small-scale prototype that could be physically tested rather than in simulation. Moreover, modelling the wind turbine is unnecessary as the goal is transferring a load onto a fixed platform (located somewhere on a turbine). This can be modelled as a standalone immovable object in Simulink. Therefore, a full design of the turbine was deemed unnecessary as it would not have an effect over the task at hand.

The objectives established to achieve the project goal are:

1. **Wave-induced vessel motions modelling**. Wave modelling and generated vessel motions are essential when designing active motion compensation systems to counteract wave induced ship motions. Thus, the sea state will be defined given a desired set of requirements so the ship platform motions could be produced.
2. **Mechanical and hydraulic design of the crane**. A crane system prototype was designed to allow motion of the payload in 3 Degrees-of-Freedom (DoF), translations along x, y and z axes.
3. **Active motion compensation control of hydraulic actuators**. A controller was implemented on the crane actuators to compensate for the simulated platform motions while achieving a desired payload translation on x-y-z cartesian coordinates system.
4. **Motion control robustness investigation**. Two controllers, traditional (feedback and feedforward) and an optimal architecture (nonlinear generalised minimum variance – NGMV) were compared. A sensitivity analysis was conducted to verify the robustness of each controller against model mismatch. Various levels of uncertainty (10%, 20% and 40%) were introduced to the hydraulic fluid bulk modulus, cylinder radius, valve area and links and payload masses. These alterations in the crane design directly influence system natural frequency and therefore, by tuning controllers' parameters, system sensitivity can be assessed.
5. **Modelling contact forces between payload and platform**. Contact force between a pair of rigid bodies needed to be modelled for load placement analysis. The normal and frictional forces were calculated using the force equation of the classical spring-damper system and the

penalty method. They are proportional to the depth and velocity as bodies were allowed to penetrate a small amount within each other's surfaces.

6. **Motion to force control switch**. Assuming the payload is above the stand it is intended to be placed on, this task requires steadily lowering the component while avoiding any excessive impact forces due to the crane motions. To that end, a hybrid controller was implemented to switch between the motion control for load positioning and lowering, and force control while placing the load on the rigid offshore platform.

1.6. Thesis Approach

Figure 1.7 illustrates the approach of the research methodology, showing the layout of the remainder of this thesis.

Section 2 presents wave modelling given a desired sea state and vessel motion response is generated. Accurate modelling is essential when designing active motion compensation systems that counteract wave motions. The Marine System Simulator is used to model vessel motions for a given set of requirements defined by the user.

Section 3 includes a presentation of the main robot types existing in industry, serial and parallel manipulators. Then, the crane prototype is depicted, detailing its sizing and the design of the hydraulic actuators that control its motion; crane dynamics and kinematics are also presented.

Section 4 presents various control algorithms with respect to crane positioning. The design of two control algorithms, traditional and optimal, employed to achieve active motion compensation for the hydraulically actuated crane are detailed. Simulation results show the performance comparison between the control architectures.

Section 5 covers the topic of contact forces modelling and control. Then, a hybrid motion/force control architecture is described and implemented for the crane system. The goal is to perform a smooth switch between the payload maneuvering and placement onto a platform.

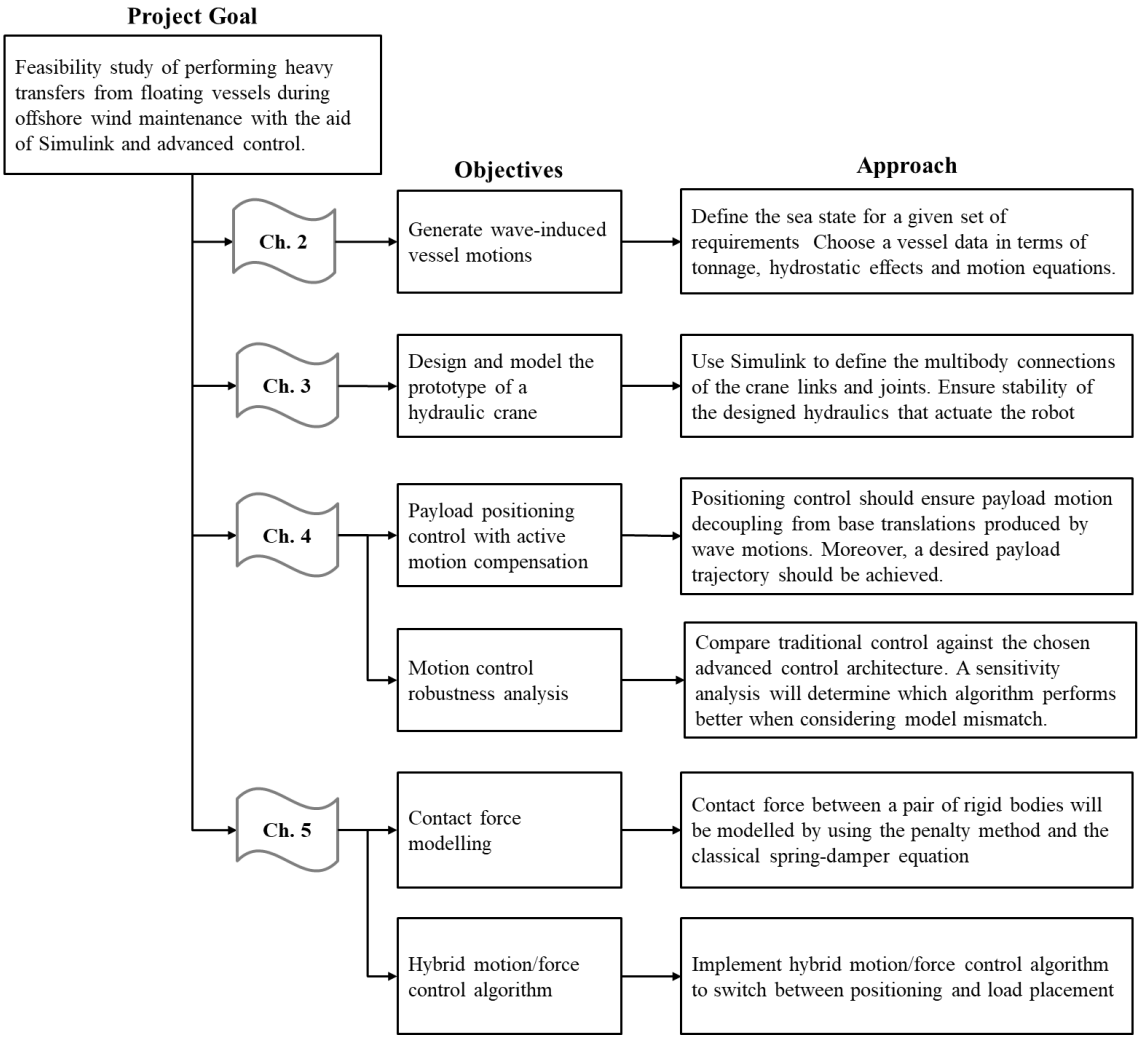

Figure 1.7: Research approach and structure of the thesis

2. CHAPTER 2: MODELLING WAVES AND SHIP MOTIONS

Wave modelling and corresponding vessel motion are essential elements when designing active motion compensation systems that counteract wave induced ship motions. The main components involved in simulating wave-induced vessel motions in 6 degrees of freedom (DoF) are shown in Figure 2.1.

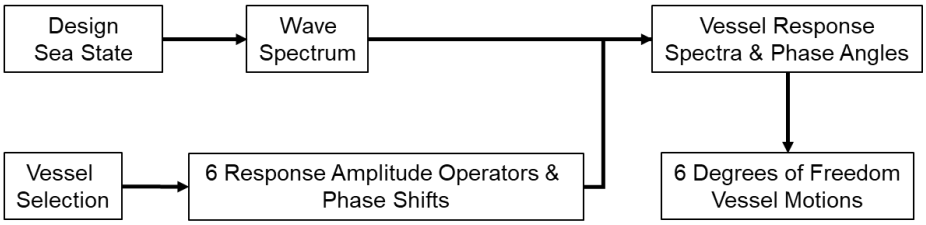

Figure 2.1: Diagram describing the procedure to simulate wave induced vessel motions in 6 Degrees of Freedom (DoF)

2.1. Wave Modelling

Waves are generated by the interaction of wind and water surface. The irregularities of the sea surface elevation in the presence of waves is a phenomenon of stochastic nature. Over a wide area and for a period of 30 minutes or more, the sea can be considered nearly statistically stationary, and thus sea elevation is considered Gaussian. If there is no wave breaking, a superposition of independent random components can describe the sea.

2.1.1. Sea State Definition

Sea state refers to the wave conditions taken at a particular wind farm location over a period of three hours. Waves significant height H_s and their mean zero-crossing period T_p are generally used to define the sea state. The statistical properties of marine waves are assumed constant during this three-hour window.

Wave period T_p is defined as the average value of all upward (or downward) zero crossing periods within the series. Significant wave height is defined as the average height of the largest 1/3 of all waves in this series. Therefore, some individual waves within a sea state will be larger than the significant wave height H_s. The maximum expected wave height H_{max} in a three-hour period can

be estimated by taking the highest of 1000 waves. Probabilistic calculations based on the Rayleigh distribution have led to the following rule of thumb (Journée and Massie, 2000):

$$H_{max} = 1.86 * H_s \tag{2.1}$$

There are three types of sea states:

1) Fully developed sea is when the wind speed is steady, so the sea conditions eventually reach a statistical stationary characteristic

2) Long crested sea is when wave components become nearly parallel and the length of the crest becomes longer than the wave height.

3) Short crested sea consists of other disturbances such as coastal reflection, so there is angular dispersion, and the wave components arrive from different directions.

An example of long-crested and short-crested irregular wave surfaces are shown in Figure 2.2.

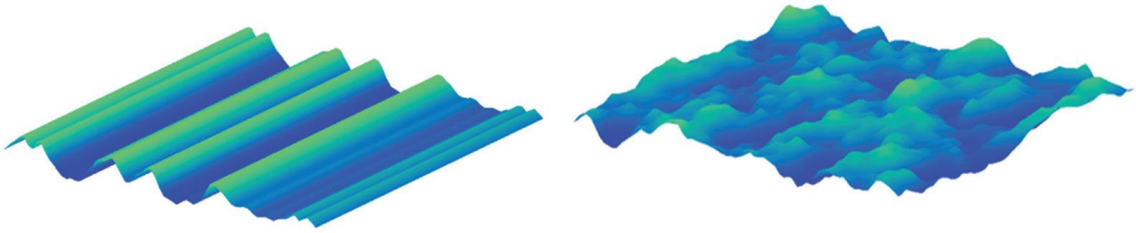

Figure 2.2: Sea surface with long-crested waves (Left) and Sea surface with short-crested waves (Right) (Anil et al., 2017)

Wave-induced ship motions are predicted more accurately using short crested waves by adding independent harmonic waves with different directions (David Salzmann, 2010):

$$\zeta(t) = \sum_{m=1}^{M} \sum_{n=1}^{N} \zeta_{a,n,m} \cdot cos\left(\omega_n \cdot t + \varepsilon_{n,m}\right) \tag{2.2}$$

where:

$\zeta(t)$	Sea surface elevation
m	Wave direction index number [-]
n	Wave number [-]
M	Number of wave directions [-]
N	Number of wave frequencies [-]
$\zeta_{a,n,m}$	Amplitude of wave component n travelling in direction m [m]
ω_n	Angular frequency of wave n [$\frac{\text{rad}}{\text{s}}$]
$\varepsilon_{n,m}$	Phase shift of wave n travelling in direction m [rad]

A short-crested wave time series can be derived from the product of a directional spreading function and a unidirectional wave variance density spectrum (David Salzmann, 2010):

$$S_\zeta(\omega,\mu) = D(\mu) \cdot S_\zeta(\omega) \tag{2.3}$$

with:

$S_\zeta(\omega,\mu)$	Directional wave variance density spectrum $\left[\frac{\text{m}^2\cdot\text{s}}{\text{rad}^2}\right]$
μ	Wave direction [rad]
$D(\mu)$	Directional spreading function [rad^{-1}]
$S_\zeta(\omega)$	Uni-directional wave variance density spectrum $\left[\frac{\text{m}^2\cdot\text{s}}{\text{rad}}\right]$

Directional spreading functions were developed since 1955 in Pierson, Neuman and James in their spectral wave forecasting method (Goda, 2018). Standard forms of directional spreading functions found in literature include the cosine 2l-power, half cosine 2s, circular-normal and the Mitsuyasu types; cosine-2s model.

2.1.2. Wave Spectrum

Wave variance density spectrum or wave spectrum plots the distribution of the variance of wave elevations as a function of the wave frequencies. Two frequently used standard wave spectra are Pierson-Moskowitz (PM) for fully developed seas and Joint North Sea Wave Project (JONSWAP)

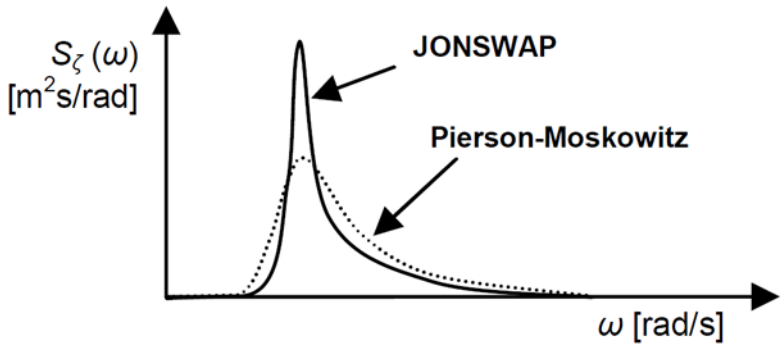

Figure 2.3: JONSWAP and Pierson-Moskowitz wave spectra

for fetch limited wind generated seas (Young, 1999). These two frequently used standard wave spectra are shown in Figure 2.3.

The continuous wave spectrum can be divided into discrete components, which are then converted to time domain as a summation of harmonics (Fourier series). Each angular frequency corresponds to a wave amplitude and a phase shift which lies within $[-\pi; +\pi]$ interval to comply with the random-phase/amplitude model (Holthuijsen, 2007).

2.2. Vessel Motions

This section discusses the procedure of deriving vessel motions for a given sea state. The relationship between wave surface elevation and vessel motion response in terms of amplitude and phase difference needs to be established.

2.2.1. Reference Frames

Body-fixed frame (b-frame) and hydrodynamic frame (h-frame) are chosen to describe the motion of an arbitrary point on a floating vessel (see Figure 2.4). They are represented with respect to North-East-Down frame.

1) b-frame is fixed to the hull and its origin coincides with the vessel centre of gravity (CoG); its axes are aligned as follows: x_b points towards the bow, y_b towards starboard and z_b downwards.

2) h-frame (O_h) is fixed when the average speed of the vessel is zero. At equilibrium (in still water), its orientation aligns with b-frame orientation.

3) The hydrodynamic frame is an inertial frame, which is by definition a frame of reference in which the motion of a particle not subject to forces is a straight line. This implies that an inertial frame is either "fixed" to the "fixed" world, or travels in this world with a constant speed in a straight line. When the vessel is positioned next to a wind turbine, the average speed of the vessel is zero thus the hydrodynamic frame is fixed. The origin O_h is defined in such a way that when the vessel is in its equilibrium position, the z_h-axis passes through the CoG of the vessel.
    - The $x_h - y_h$ plane is placed parallel to the still-water plane, the x_h-axis points towards the bow, the y_h-axis towards portside and the z_h-axis upwards. The origin O_h is chosen to coincide with the equilibrium position of the CoG here. Since the orientation of the h-frame axes is the same as the orientation in the b-frame, the h-frame and the b-frame will coincide when the vessel is in its equilibrium position, i.e. in still water.

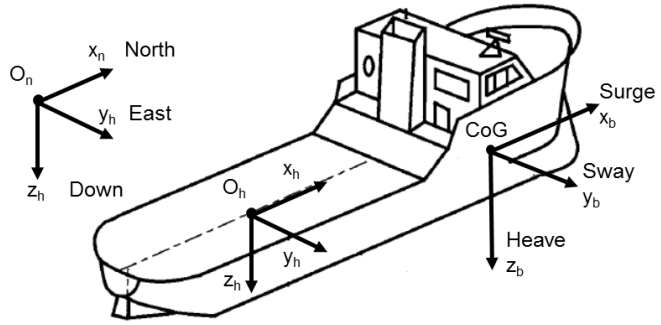

Figure 2.4: Notation and sign convention of reference frames for ship motion description (David Salzmann, 2010)

2.2.2. Vessel response

Vessel motion can be related to wave motions on all six axes through:

1. Motion Response Amplitude Operators (RAO), defined as ratio between vessel and wave amplitudes and

2. Phase differences between wave surface elevation and vessel motion

$$surge: RAO_x(\omega) = \frac{x_a}{\zeta_a}(\omega)\ \left[\frac{m}{m}\right] \quad roll: RAO_\varphi(\omega) = \frac{\varphi_a}{\zeta_a}(\omega)\ \left[\frac{rad}{m}\right]$$

$$sway: RAO_y(\omega) = \frac{y_a}{\zeta_a}(\omega)\ \left[\frac{m}{m}\right] \quad pitch: RAO_\varphi(\omega) = \frac{\theta_a}{\zeta_a}(\omega)\ \left[\frac{rad}{m}\right] \tag{2.4}$$

$$heave: RAO_z(\omega) = \frac{z_a}{\zeta_a}(\omega)\ \left[\frac{m}{m}\right] \quad yaw: RAO_\varphi(\omega) = \frac{\psi_a}{\zeta_a}(\omega)\ \left[\frac{rad}{m}\right]$$

with:

$x_a, y_a, z_a, \varphi_a, \theta_a, \psi_a$	Motion amplitudes in [m] and [rad]
ζ_a	Sea surface elevation [m]
ω	Angular frequency of wave and responses [rad/s]
t	Time [s]

Vessel motion time series response in irregular waves are required when designing active motion compensation systems. They can be determined similarly to Section 2.1, i.e. through Fourier series (assuming linear proportionality between wave and vessel motion in any DoF) and wave variance density spectrum.

Heave motion in short-crested waves (for example) can be expressed as (David Salzmann, 2010):

$$r_z(t) = \sum_{m=1}^{M}\sum_{n=1}^{N} RAO_z(\omega_n, \mu_m) \cdot \zeta_{a,n,m}\, cos\left[\omega_n t + \varepsilon_{n,m} + \varepsilon_{z\zeta}(\omega_n, \mu_m)\right] \tag{2.5}$$

with:

r_z	Heave [m]	ω_n	Angular frequency of wave n [rad/s]
m	Wave direction index number [-]	μ_m	Wave direction m [rad]
M	Number of wave directions [-]	$\zeta_{a,n,m}$	Amplitude of wave n travelling in direction m [m]
n	Harmonic wave index number [-]	ε_n	Phase shift of wave n travelling in direction n [rad]
N	Number of wave frequencies [-]	$\varepsilon_{z\zeta}$	Wave elevation to heave phase difference [rad]
RAO_z	Heave Response Amplitude Operator [-], defined as the ratio between vessel and wave amplitudes		

2.3. Ship Platform Motion Modelling

The Marine System Simulator in Simulink enables the implementation of mathematical models of marine systems with focus on control system design. The required equations of motion and forces were incorporated in Simulink blocks to characterize real-life case of marine systems elements

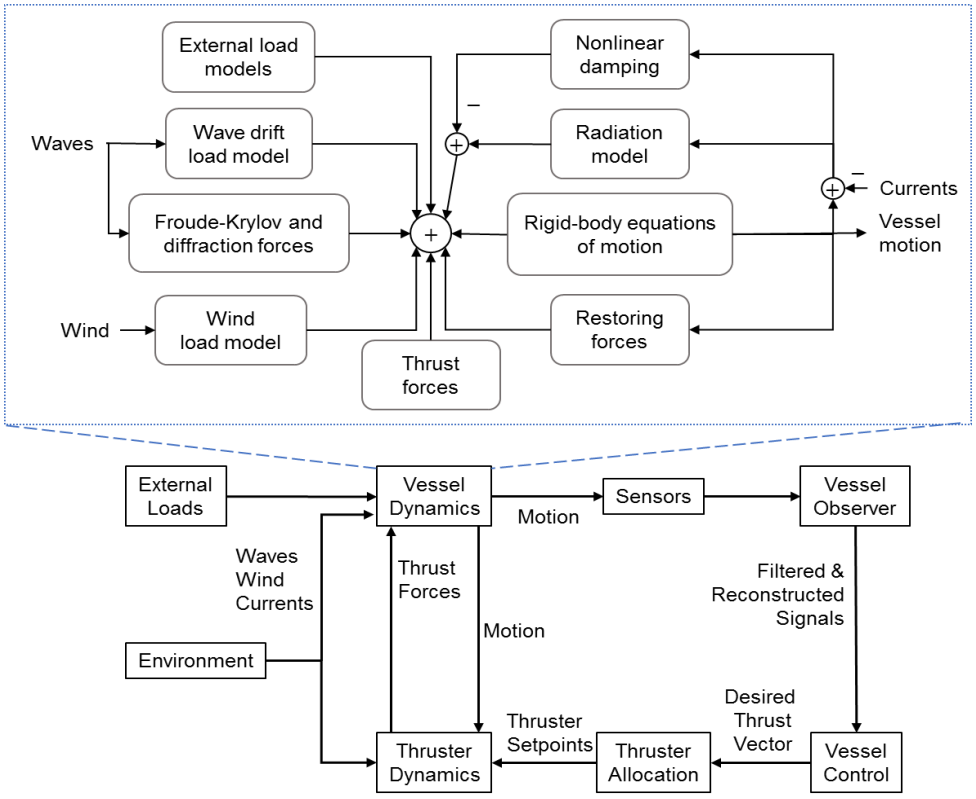

Figure 2.5: Marine system components

interactions (Figure 2.5 reproduced from (Perez et al., 2006b)).

Marine GNC Toolbox is a core component of Marine System Simulator (MSS) and incorporates Simulink dedicated modules to define environmental conditions and the resulting vessel motions in 6 Degrees-of-Freedom.

Vessel motions in MSS are expressed relative to the b-frame and the equations are given by its dynamics. These forces include Coriolis and centripetal accelerations effect, linear damping of ship generated waves due to gravity and buoyancy (restoring forces), viscous effects and

environmental disturbances. GNC features dynamic positioning controller to counteract the resulting horizontal vessel movement.

Another useful tool in MSS is Marine Hydro add-in, which includes vessel models to simulate and obtain reference time series of vessel response motions on all 6 axes. Due to its reliability, the current project will use the MSS toolbox for generating wave-induced ship motion profiles.

The sea state selected for the purpose of this work features a 5 m significant wave height H_s and is a superposition of independent random harmonics with maximum wave frequency of 1 rad/s or 6.3 seconds period T_p. The reason behind choosing this set of parameters was to provide a worst-case scenario for the sea state and ensure the crane design can satisfy these requirements. However, in real-life the sea state would vary depending on the location of the wind farm and weather conditions. Thus, it would be impractical to carry out O&M when waves have a significant height of 5 m, and a H_s=1.5 m might be usually the case.

A JONSWAP spectrum (Young, 1999) was employed to obtain the wave components in terms of frequency and directionality. An example of sea state realization and wave spectrum corresponding to the selected design are displayed in Figure 2.6.

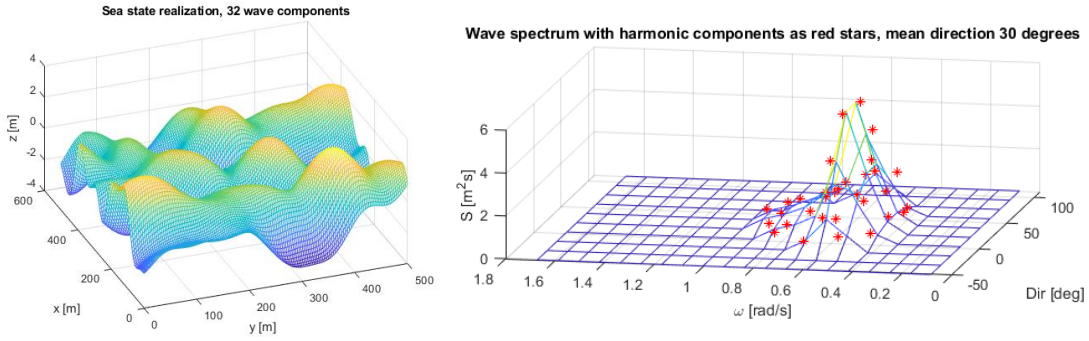

Figure 2.6: Sea state realization and its corresponding JONSWAP spectrum

A vessel of length 175 m (S175 model available ins MSS) was chosen for this application to accommodate the hydraulic crane. Having selected the sea state and the vessel dimension, the Marine System Simulator (MSS) toolbox in Simulink was used to generate wave-induced ship motion profiles for translation and rotation axes on x-y-z as shown in Figure 2.7.

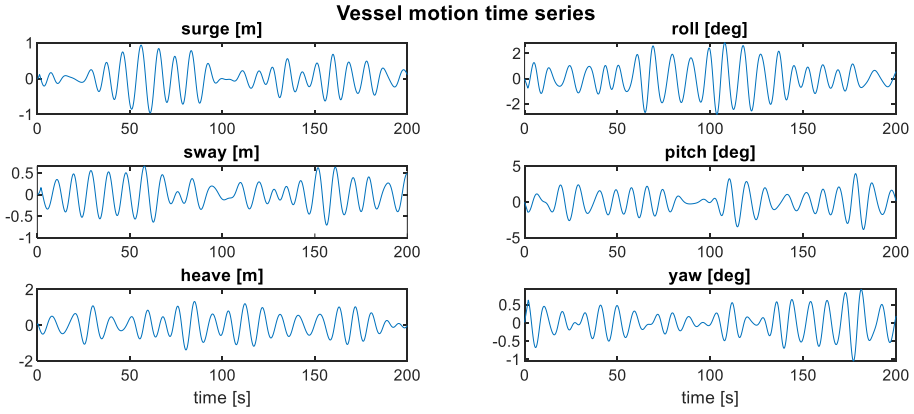

Figure 2.7 Six degrees-of-freedom vessel motion response

2.4. Chapter Summary

The sea state selected for the purpose of this work features a 5 m significant wave height H_s and is a superposition of independent random harmonics with maximum wave frequency of 1 rad/s or approximately 6.3 seconds period T_p. Research was carried out with respect to finding appropriate design choices for the task at hand and an appropriate example in the field was found in another PhD thesis (David Salzmann, 2010). The reason behind choosing this set of parameters was to

provide a worst-case scenario for the sea state and ensure the crane design can satisfy these requirements. However, in real-life the sea state would be different depending on the location of the wind farm. Thus, it would be impractical to carry out O&M when waves have a significant height of 5 m, and a H_s=1.5 m might be usually the case. Finding the tools to model the right tools to model the wave-induced vessel motions was also part of the research. This report reviewed the Marine System Simulator robust methodology that incorporated various marine components to be able to describe the sea states and generate vessel motions in Simulink (Perez et al., 2006b).

3. CHAPTER 3: CRANE DESIGN AND MODELLING

3.1. Introduction

One of the objectives of the present research is designing and modelling in Simulink a robot structure. This handling mechanism should be able to transfer heavy loads in the range of tens of tons onto a platform while being placed on a moving base. This chapter aims at introducing the main types of industrial robot manipulators, which can be serial or open chain. While open-chain/ parallel robots will not be considered in the present work, they will be presented due to being part of a relevant project in the field of offshore maintenance (David Salzmann, 2010). Finally, an appropriate robot architecture will be determined to be designed and modelled.

3.1.1. Serial Manipulator

Open-chain manipulators are made up of joints that connect links together sequentially (example given in Figure 3.1). Generally, there are manipulators with only a few axes and they have the ability to reach on six axes (therefore 6 DoF) and the gripper can only change its orientation; wrist point is a frame associated with the end of the last link of the robot arm.

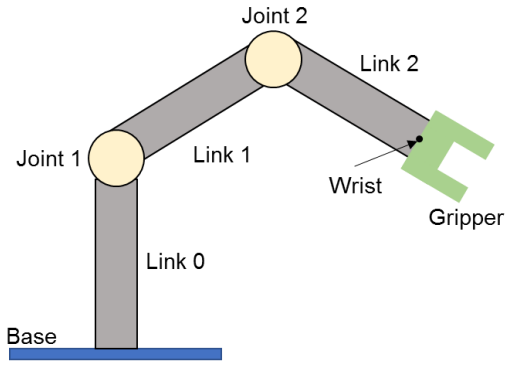

Joint Type	Number of DoF	Typical Form
Universal/Hooke	2	
Spherical/Ball	3	
Prismatic/Slider	1	
Cylindrical	2	

Figure 3.1: Diagram of a serial manipulator and four common types of joints

For the purpose of this project, a robotic structure should be able to maneuver a load attached to its gripper to the base of the wind turbine platform to transfer any required component (gearbox, generator) during maintenance. A telescopic arm robot (Brudniok et al., 2009), that is mounted on

the vessel deck and extends/retracts its cylindrical tubes to lift an attached load, could be suitable for such application, however it was not used in this project. However, such a mechanism would only provide motion compensation on the vertical axis (heave) thus requiring an additional system to balance out motions on the other axes. An attempt was made to model such a mechanism at the initial design stages; a different robot structure was opted for ultimately. The choice for the handling system will be presented and detailed later in this chapterdexte.

Grippers

Grippers activate jaws or fingers to pick up, hold, or move work pieces. The gripping elements can be fingers that pivot about base points or jaws that slide parallel or in the same plane with each other like clamps or chuck jaws. Characteristics of robotic grippers were listed in Table 3.1 and Table 3.2.

Table 3.1: Robotic grippers actuation.

Actuation type	**Actuator**
Manual	hand crank, wheel, levers
Electrical	electric motor, solenoid
Pneumatic	compressed air
Hydraulic	hydraulic fluid

Table 3.2: Gripper action.

Gripper action type	**Description**
Single action	Drive in only one direction but incorporate a return spring to the unpowered position (supply pressure or electricity off.)
Double action	Actuated both open and closed. Force ratings can differ in the two directions
Double action spring assist open	Actuation method that opens and closes the gripper, but with spring assist in open direction
Double action spring assist close	Actuation method that opens and closes the gripper, but with spring assist in the close direction

Workspace

A robot work envelope is the locus of points in 3D space that can be reached by the end effector (e.g. a wrist point) as shown in Figure 3.2.

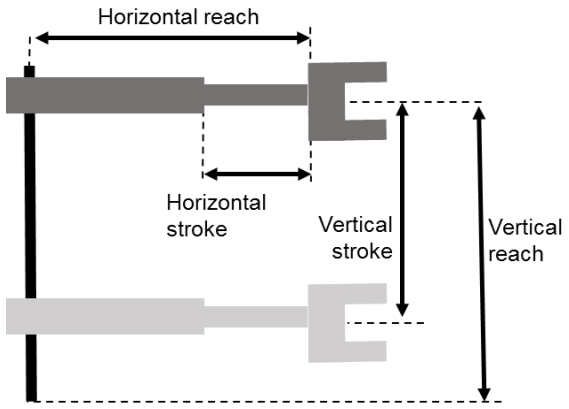

Figure 3.2: Diagram showing the work envelope of a generic robot arm gripper

For a simple case of a rectangular robot arm given in Figure 3.2, stroke is the total distance the wrist can travel horizontally and vertically. Horizontal reach is the maximum radial distance of the wrist from the vertical axis about which the robot rotates. Vertical reach is the maximum elevation above the work surface.

3.1.2. Parallel manipulator

Parallel manipulators are closed-chain mechanisms with two platforms (fixed base and moving platform), connected by at least two independent kinematic chains. They feature higher stiffness and greater load-to-weight ratio, which result in improved accuracy, high speed, and stiffness but have limited workspace capacity when compared to serial manipulators.

A Stewart platform is a parallel manipulator and its architecture (Figure 3.3) is determined by the choice of top and base radii, separation between gimbal pairs at top and base, cylinder stroke and cylinder dead length.

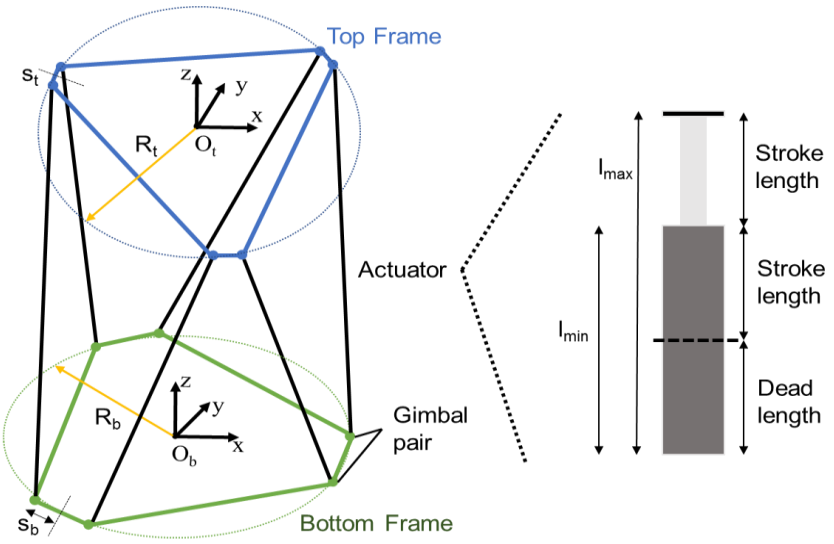

Figure 3.3: Diagram of a Stewart platform arrangement

Stroke length (l_{stroke}) corresponds to the extendable part of the cylinder and dead length (l_{dead}) accounts for the part that is unused for extension. A minimum dead length is necessary to fit the gimbals and their connections to the cylinder. Total cylinder length is defined as the distance between the two gimbal centers. Minimum and maximum cylinder lengths (l_{min}, l_{max}) are related to stroke and dead length according to:

$$l_{min} = l_{dead} + l_{stroke};\ l_{max} = l_{dead} + 2 \cdot l_{stroke} \tag{3.1}$$

Half separation distances between top and base gimbal pairs are denoted as s_t and s_b, while the radii of top and base frames are R_t and R_b as shown in Figure 3.3.

The joints connecting each hydraulic cylinder to both top and bottom frame need to add up to six DoF to achieve complete motion compensation in all axes. In offshore maintenance, universal joints are generally preferred over spherical joints due to lower costs and higher robustness, so they are used at both connection ends. A prerequisite for this option is that the cylinders function as a cylindrical joint: the rod should be able to rotate freely around its axis relative to the casing (David Salzmann, 2010).

Workspace, dexterity, and cylinder forces are features that need to be considered when selecting an optimal Stewart Platform design for a given set of its architecture parameters, size constraints and platform loading. Size constraints are related to the on-deck area available, which thus dictates the top and base radii of the platform to be installed. Platform loading refers to the effect of forces, caused by the weight of a load on the hydraulic actuators.

Workspace

The workspace refers to total motion range of the platform and includes all poses in which the cylinder lengths meet the following criterion:

$$l_{min} \leq l_i \leq l_{max}, \qquad i = 1,2,\dots,6 \tag{3.2}$$

A simplified and accepted manner to describe the properties of a workspace is to present the maximum non-simultaneous excursions of the platform in each degree of freedom. These excursions can be determined by varying the translation or rotation in one DoF at a time until the criterion in (3.2) is no longer met, i.e. until at least one of the actuators hit minimum/maximum limits. For practical reasons, the starting point of this calculation is the neutral position of the platform, i.e. at half of its maximum heave.

Dexterity

Dexterity is a characteristic of a Stewart platform pose and it is assigned values in the interval [0;1], with 0 indicating the occurrence of singularity. Mechanical singularity means a configuration in which the platform behaves unpredictably, that is introducing more degrees of freedom.

High dexterity means an efficient use of the actuator length changes relative to the Stewart platform motions. According to Ampelmann thesis (David Salzmann, 2010), dexterity should be at least 0.2 for the actuator forces and velocities to be within reasonable limits and avoid singularities (Advani, 1998). Moreover, this MSc study (Anders Lohmann Madsen and Søren Giessing Kristensen, 2012) concluded that the primary objective for wave compensation was achieving good dexterity.

Computing Dexterity of a Stewart Platform

This property is calculated as follows:

- Changes in platform positions and in cylinder lengths are stored in the Jacobian J:

$$\underline{\dot{l}} = \frac{\partial \underline{l}}{\partial \underline{x}} . \underline{\dot{x}} = J . \underline{\dot{x}} \tag{3.3}$$

where $x = [x\ y\ z\ \varphi\ \theta\ \psi]^T$ is the platform position vector and $l = [l_1\ l_2\ l_3\ l_4\ l_5\ l_6]^T$ is the cylinder length vector.

Every column in the Jacobian matrix is calculated by implementing a slight change of value in one DoF and then calculating the rate of change in each cylinder length.

- Obtain the condition number k:

$$\kappa = \|J\| . \|J^{-1}\| \tag{3.4}$$

Singular value decomposition can be used to produce the diagonal matrix of singular values of J:

$$J_s = \begin{bmatrix} \sigma_1 & 0 & 0 & 0 & 0 & 0 \\ 0 & \sigma_2 & 0 & 0 & 0 & 0 \\ 0 & 0 & \sigma_3 & 0 & 0 & 0 \\ 0 & 0 & 0 & \sigma_4 & 0 & 0 \\ 0 & 0 & 0 & 0 & \sigma_5 & 0 \\ 0 & 0 & 0 & 0 & 0 & \sigma_6 \end{bmatrix} = \sigma_i . I_6, \quad i = 1, \dots, 6 \tag{3.5}$$

Using the minimum and maximum singular values from J_s gives another method to derive the condition number of the Jacobian and thus the dexterity:

$$Dexterity = \frac{1}{k} = \frac{\sigma_{max}(J_s)}{\sigma_{max}(J_s)} \tag{3.6}$$

Cylinder Forces

The maximum expected axial loads on the hydraulic cylinders are an important aspect to be considered, and they depend on the architecture and pose of the Stewart platform. These loads are caused by the displacements (surge, sway, heave) and rotations (roll, pitch, yaw) of the bottom frame relative to the top frame and are counteracted by the normal forces in each actuator.

3.2. Crane System Description

The prototype designed for the purpose of this project is a 90 m tall hydraulic crane robot. It holds a 660 ton payload and it is placed on a moving base with 4 degrees of freedom (DoF) that can achieve payload translations along the x, y and z axes, as shown in Figure 3.4.

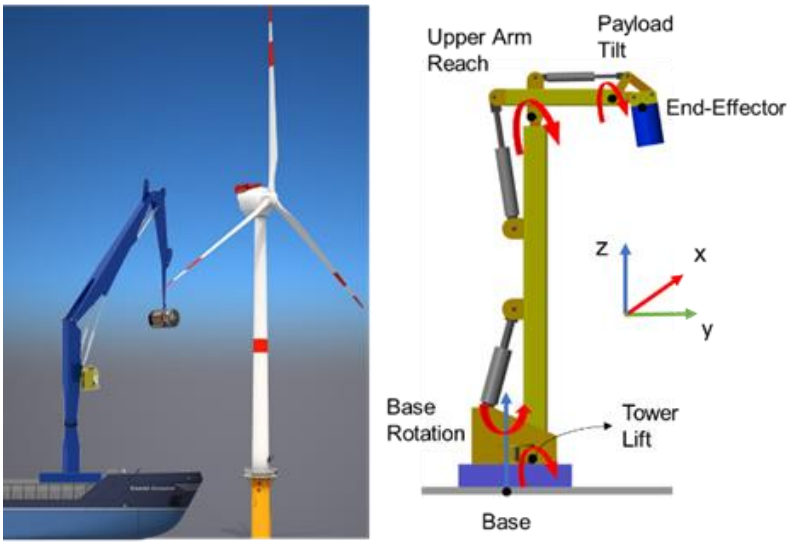

Figure 3.4: Real-life scenario is presented on the left and a simplified Simulink representation of the hydraulic crane is displayed on the right

The design choices were arbitrary, as the initial purpose was placing the load (nacelle) on top of the wind turbine tower, therefore the need to model such a tall structure. A key note is that real-life considerations of implementing this particular crane design were not accounted for. Thus, it might be impractical or even impossible to use a crane of this size for the considered vessel size, and instead a smaller robot could be used. However, a crane of reduced dimensions would imply re-designing the hydraulics and control architecture. This is not trivial and can prove to be a lengthy process until system stability could be ensured. Thus, due to time constraints, such work could be

covered in a future project. As a final remark on implementing the real-life system, scaled prototypes should be built and tested on land and on water to determine whether the control approach would match simulation expectations to actual performance. A thorough risk analysis would also be required to establish the insurances, certification and regulations before commercialization. However, development for production of such a system is outside the scope of the present project.

The goal is to move the payload over a predefined 3D trajectory (in the earth-based frame) while compensating for the vessel motions. To achieve that, four actuators (three hydraulic cylinders and one motion actuator for the robot base) rotate the crane joints. The desired payload trajectory is converted into corresponding joint rotations via Inverse Kinematics (IK). The measured payload position is taken by placing a motion sensor at the crane end-effector (EE) relative to a fixed world reference frame.

With respect to the diagram on the right in Figure 3.4, payload translations are achieved by rotation of the four joints: ‘Base Rotation’ provides payload translation on x-axis, ‘Tower Lift’ moves the payload on the y-axis, ‘Arm Reach’ covers the up/down motion on the z-axis, while the last joint 'Payload Tilt' rotate the payload to provide a finer adjustment of the pitch angle. However, the four actuators included in the crane system were employed to only control the x-y-z position of the payload. Crane base rotation compensation around y-axis (pitch) could also be achieved as there are 4 actuators on the crane, but the decision was not to include it. The reason was to minimise the complexity of the task and improve control performance, thus achieving payload translation with better precision. Including the additional base rotation as motion reference was found to deteriorate the controller performance.

3.3. Hydraulic Actuator Design

3.3.1. Description

A double acting hydraulic actuator was employed to control each of the three joints presented in Figure 3.4. The schematic diagram presented in Figure 3.5 consists of a constant pressure supply pump, a servo valve, and the hydraulic cylinder.

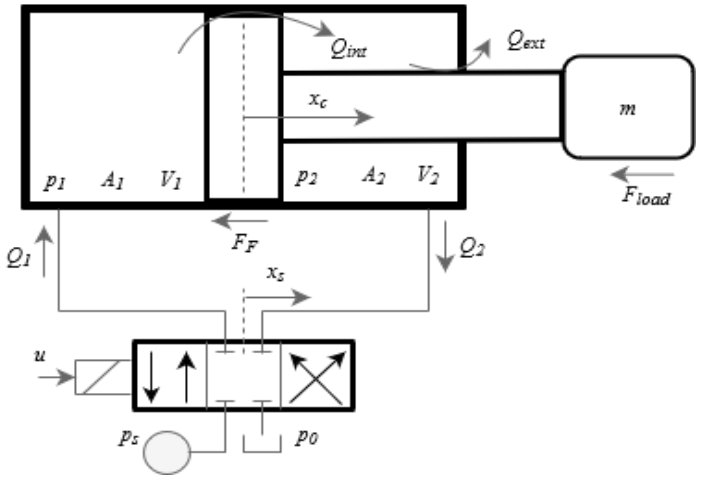

Figure 3.5: Diagram of a hydraulic actuator

An example of modelling a nonlinear hydraulic actuator is presented in (Šulc and Jan, 2002) along with the derivation of its state-space representation, which is given below in eq. (3.7):

$$\dot{x}_1 = x_2$$

$$\dot{x}_2 = \frac{1}{m}\left[x_3 A_1 - x_4 A_2 - F_F(x_2) - F_{load}\right]$$

$$\dot{x}_3 = \frac{\beta(x_3)}{V_{0,1} + A_1 x_1}\cdot\left[Q_1(x_3, x_5) - A_1 x_2 - Q_{int}(x_3, x_4)\right] \tag{3.7}$$

$$\dot{x}_4 = \frac{\beta(x_4)}{V_{0,2} + A_2 x_1}\cdot\left[Q_{int}(x_4, x_5) - Q_{ext}(x_4) - A_2 x_2 + Q_2(x_4, x_5)\right]$$

$$\dot{x}_5 = x_6$$

$$\dot{x}_6 = \omega_n^2 u - 2B\omega_n x_6 - \omega_n^2 x_5$$

where:

x_1, x_c	Position of cylinder piston [m]	$Q_{1,2}$	Flow rate to chambers 1 and 2 [m^3/s]
x_2, v_c	Velocity of cylinder piston [m/s]	Q_{int}, Q_{ext}	Internal and external leakage flows [m^3/s]

x_3,p_1	Fluid pressure in chamber 1 [Pa]	$V_{0,1/2}$	Initial fluid volume in chambers [m^3]
x_4,p_2	Fluid pressure in chamber 2 [Pa]	F_F, F_{load}	Friction and load forces [N]
x_5,x_s	Position of valve spool [m]	β	Fluid bulk modulus [Pa]
x_6,v_s	Velocity of valve spool [m/s]	m	Load mass [kg]
A_1,A_2	Chambers 1 and 2 areas [m^2]	B, ω_n, u	Valve damping [-], natural frequency [rad/s] and input voltage [V]

Systems with overall high natural frequency (including member flexion in the links) are easier to control. As a rule of thumb system natural frequency should be at least 4 times the desired frequency of acceleration. In this application, the required frequency of acceleration is directly related to the frequency of the wave and vessel motions to be compensated.

Cylinder pressure equations and piston motion given in (3.7) describe the dynamics of the system. Applying Laplace and solving them simultaneously, gave:

$$\dot{x}_1 = \frac{\frac{1}{m}s}{s^2 + \frac{B}{m}s + \frac{A^2\beta}{m}(\frac{1}{V_{0,1}} + \frac{1}{V_{0,2}})} \tag{3.8}$$

Note that chambers areas were considered equal so that $A_1 = A_2 = A$ which gave the relation above.

Comparing the coefficients in the denominator with a standard second order system, the natural frequency and damping ratio were given as:

$$\omega = A\sqrt{\frac{\beta}{m}(\frac{1}{V_{0,1}} + \frac{1}{V_{0,2}})}$$

$$\zeta = \frac{B}{2A}\sqrt{\frac{V_{0,1}V_{0,2}}{m\beta(V_{0,1} + V_{0,2})}} \tag{3.9}$$

When the piston is in its central position, the initial chamber volumes are equal, so the natural frequency can be increased by adjusting the parameters in eq.(3.10) (Chapter 3, Andersen, 2003):

$$\omega = \sqrt{\frac{2\beta A^2}{V * m}} \tag{3.10}$$

The parameters in (3.10) can be modified to achieve the desired natural frequency. A fluid with a larger bulk modulus, larger piton areas (but smaller fluid volumes) or a reduced load mass, all result in increased ω.

3.3.2. Cylinder Sizing

The cylinder bore and rod diameters are usually determined by the maximum expected loads. In the case of the hydraulic crane, these are functions of the crane links and payload masses and the poses of the individual crane links due to motion compensation. As the cylinder sizes are the critical components of the hydraulic system model, they needed to be defined before running any simulations.

The cylinder load forces F_{max} to be compensated by the pressure in the hydraulic cylinders were estimated. The individual cylinder force balance then follows as (for cylinder compression case):

$$F_{cyl} = P_a S_a - P_b S_b \tag{3.11}$$

where:

F_{cyl}	Force acting on the cylinder piston to extend/retract
P_a	Chamber A pressure
P_b	Chamber B pressure
S_a	Chamber A area
S_b	Chamber B area

F_{cyl} needs to balance the static load F_{load} (due to gravity) and exert additional force, the direction of which depends on which way the load should move. In general, the force acting on the piston is:

$$F_{pist} = F_{cyl} - F_{load} \tag{3.12}$$

This then determines the acceleration, velocity, and displacement of the piston with the effective inertia and force varying with the pose. Too small F_{cyl} may cause cavitation in the cylinder where the system is not controllable but 'falls' due to gravity.

Solution: increase cylinder size (S_a and S_b), supply pressure P_s, or simply reduce the mass of the machine (which will reduce F_{load})

The following assumptions were made for the calculations:

- The ratio of diameters set to: $\alpha_D = \frac{D}{d} = 2.22$, where D is the bore diameter, and d is the piston diameter
- Supply pressure P_s = 350 bar

The resulting diameters for the three cylinders named as shown in Figure 3.4 are collected in Table 3.3. The table also includes the cylinder strokes, however these parameters are not relevant for the power and flow calculations and were selected to be large enough for the worst-case sea states considered (the buckling and other effects are ignored).

Table 3.3: Computed hydraulic cylinder sizes

Cylinder	**Bore diameter, D (m)**	**Rod diameter, d (m)**	**Stroke, h (m)**
Tower Lift	4.65	2.09	13.5
Arm Reach	3.75	1.5	18.24
Payload Tilt	2.4	0.9	11.34

In general, the larger the cylinders are, the smaller the supply pressure needs to be to produce the required forces. On the other hand, large cylinders mean high flows to generate piston velocities for motion compensation. Either way, the pump power rating (product of supply pressure and maximum flow) must also be sufficient. These various hydraulic system parameters will of course need further optimization to achieve the best trade-offs between the available power and flow rates, and the system size and cost.

As a note with respect to Table 3.3, the largest cylinders available in fabrication have a bore sized at 1.5 m, whereas calculations showed a required Tower Lift bore at around 5 m. This indeed shows that the setup is unrealistic, however the emphasis of this present work is on proving a concept through simulation. Therefore, the focus is on showing that a crane system this size can be stabilizable and, moreover, controlled to achieve active motion compensation while safely placing the load on a fixed platform. Further work would involve resizing this system to more realistic dimensions and adjusting the controllers as required.

3.4. Crane Kinematics

3.4.1. Introduction

Kinematics studies the motion of bodies without considering the forces or moments that cause it. In robotics, kinematics refers to the motion of a manipulator, which can be mathematically derived through direct displacement analysis (forward kinematics) and inverse kinematics.

Inverse kinematics, in the case of serial link manipulators, compute the angles of the revolute joints and displacements of the prismatic joints while the pose of the tool tip is given in order to control the position of the robot (Peng et al., 2012). Solving the inverse kinematics is computationally expensive for this type of manipulators (no closed-form solutions exists), therefore impractical in the real time control (Kucuk and Bingul, 2006).

For the Inverse Kinematics (IK) algorithm, a robust numerical solution can be computed via Levenberg-Marquardt method in Simulink (Sugihara, 2009). Even in cases where the problem does not have solutions or has many solutions, the method converges to the optimum solution in the sense that it minimizes the residual from the target points with the smallest joint deviations. Moreover, the method is remarkably stable and fast no matter how far the target point is from the

solvable range. Some numerical evaluations on a kinematic model of a redundant manipulator show that it stably converges without a close initial guess.

Forward kinematics for a robot mechanism is required to calculate the position and orientation of the end-effector in terms of joint variables. Denavit-Hartenberg (DH) is the most common method for describing the robot kinematics (Lipkin, 2008) and uses four parameters, link length l_i, link twist α_i, link offset d_i and joint angle θ_i. A coordinate frame is attached to each joint to determine DH parameters with z_i axis pointing along the rotary or sliding direction of the joints, as shown in Figure 3.6.

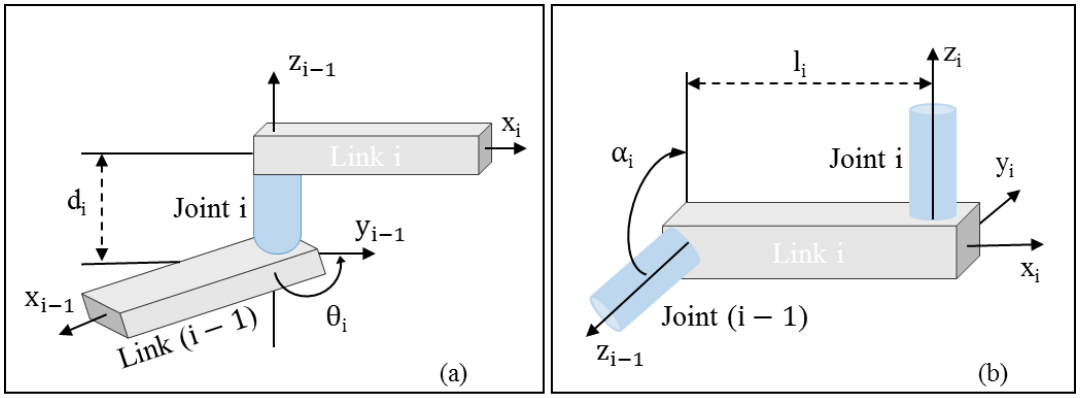

Figure 3.6: Coordinate frame assignment for general manipulators. (a) Position and orientation of two successive links are specified by two joint parameters. (b) Position and orientation between two successive joints are specified by two link parameters

The parameters presented in Figure 3.6 are described as:

θ_i: Rotation about z_{i-1} such that x_{i-1} is parallel to x_i.

d_i: Translation along z_{i-1} such that x_{i-1} intersects x_i.

l_i: Translation along x_i such that z_{i-1} intersects z_i.

α_i: Rotation about x_i such that z_{i-1} is parallel to z_i; multiple of $\pi/2$.

The general transformation matrix ${}^{i-1}_{i}T$ for a single link can be obtained from the DH algorithm as follows:

$$ {}^{i-1}_{i}T = R(z_{i-1}, \theta_i) \cdot Tr(z_{i-1}, d_i) \cdot Tr(x_i, l_i) \cdot R(x_i, \alpha_i) = \begin{bmatrix} c\theta_i & -c\alpha_i s\theta_i & s\alpha_i s\theta_i & l_i c\theta_i \\ s\theta_i & c\alpha_i c\theta_i & -s\alpha_i c\theta_i & l_i s\theta_i \\ 0 & s\alpha_i & c\alpha_i & d_i \\ 0 & 0 & 0 & 1 \end{bmatrix} \quad (3.13) $$

with s: sine( ); c: cosine( )

$R( )$ describes a pure rotation and $Tr( )$ a pure translation. The order of multiplication of matrices in the procedure describes a frame F_i relative to a frame F_{i-1}.

The forward kinematics of the end-effector with respect to the base frame is determined by multiplying all of the ${}^{i-1}_{i}T$ matrices:

$$ {}^{base}_{end-effector}T = {}^{0}_{1}T * {}^{1}_{2}T * \cdots * {}^{n-1}_{n}T = \begin{bmatrix} r_{11} & r_{12} & r_{13} & p_x \\ r_{21} & r_{22} & r_{23} & p_y \\ r_{31} & r_{32} & r_{33} & p_z \\ 0 & 0 & 0 & 1 \end{bmatrix} \quad (3.14) $$

where r_{kj} terms represent the rotational elements of transformation matrix (k and j=1, 2 and 3). p_x, p_y and p_z denote the elements of the position vector.

3.4.2. Forward and Inverse Kinematics Implementation

In order to compute the Inverse Kinematics of the robotic manipulator considered in this work, its forward kinematics needed to be determined first. Thus, following the approach presented in the previous section, the Denavit-Hartenberg representation needed to be completed first. Thus, its frames for all the joints were displayed in Figure 3.7, from which the kinematic parameters could be extracted in Table 3.4.

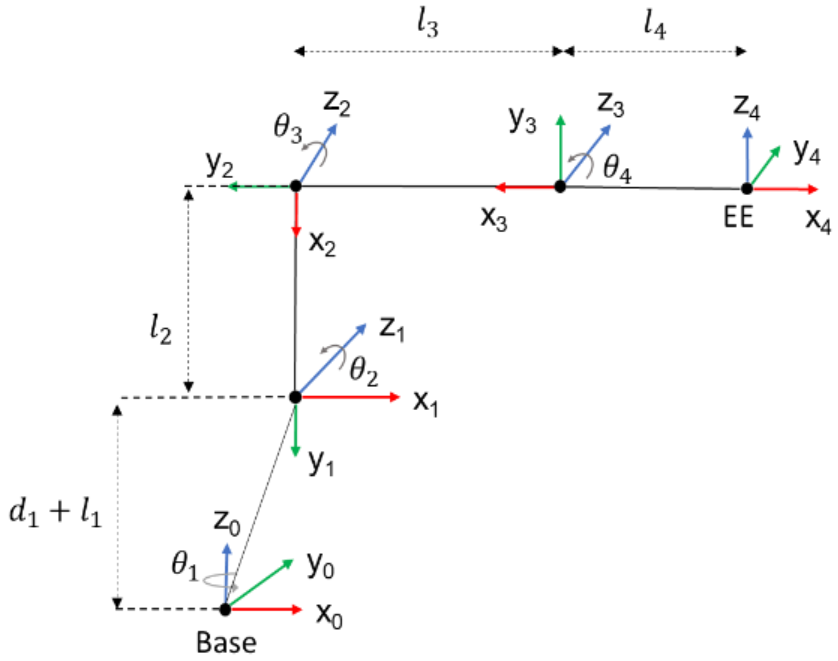

Figure 3.7: Tree representation for the hydraulic crane showing the connectivity between its links and joints

Table 3.4: Kinematic parameters for the hydraulic crane

Axis	$\boldsymbol{\theta_n}$	$\boldsymbol{\alpha_n}$	$\boldsymbol{l_n}$	$\boldsymbol{d_n}$
1	θ_1	$\pi/2$	5.4	9.33
2	θ_2	0	88.65	0
3	θ_3	0	26.5	0
4	θ_4	$-\pi/2$	3.5	0

The transforms required to express the end-effector of the robot relative to its base can be evaluated by substituting the values from Table 3.4 into equation (3.13) for each of the axes of the robot. The result is as shown next:

$$
{}^{0}_{1}T = \begin{bmatrix} c\theta_1 & 0 & s\theta_1 & 5.4 * c\theta_1 \\ s\theta_1 & 0 & -c\theta_1 & 5.4 * s\theta_1 \\ 0 & 1 & 0 & 9.33 \\ 0 & 0 & 0 & 1 \end{bmatrix}
$$

$$
{}^{1}_{2}T = \begin{bmatrix} c\theta_2 & -s\theta_2 & 0 & 88.65 * c\theta_2 \\ s\theta_2 & c\theta_2 & 0 & 88.65 * s\theta_2 \\ 0 & 0 & 1 & 0 \\ 0 & 0 & 0 & 1 \end{bmatrix}
$$

$$
{}^{2}_{3}T = \begin{bmatrix} c\theta_3 & -s\theta_3 & 0 & 26.5 * c\theta_3 \\ s\theta_3 & c\theta_3 & 0 & 26.5 * s\theta_3 \\ 0 & 0 & 1 & 0 \\ 0 & 0 & 0 & 1 \end{bmatrix} \tag{3.15}
$$

$$
{}^{3}_{4}T = \begin{bmatrix} c\theta_4 & 0 & -s\theta_4 & 3.5 * c\theta_4 \\ s\theta_4 & 0 & c\theta_4 & 3.5 * s\theta_4 \\ 0 & 1 & 0 & 0 \\ 0 & 0 & 0 & 1 \end{bmatrix}
$$

The forward kinematics of the crane system can be thus determined by multiplying all of the ${}^{i-1}_{i}T$ matrices, with i=1,…,4 giving the ${}^{0}_{4}T$ matrix as presented in eq.(3.14).

Knowing the initial guess of the crane configuration in terms of joint positions, i.e. $[0, -95, 0, -10]°$ with respect to its pose in Figure 3.7, Levenberg-Marquardt algorithm could be computed in Matlab to generate the joint angles for a given payload trajectory.

3.5. Crane Dynamics

The dynamics of serial-link manipulators are usually solved via the inverse dynamics as it is straightforward and computationally simpler than forward dynamics (Angeles, 2014). Inverse dynamics problem is generally solved with Newton-Euler algorithm to compute torque or force at different actuated joints, given past states of cartesian or joint coordinates, along with the architecture and inertial parameters of the system.

Crane dynamics refer to how each piston displacement influence its corresponding joint rotation. The dynamics are determined by the inertia and loads 'seen' by each actuator, and these vary according to the mechanism pose. For example, the lift actuator experiences more force when the tower is lowered compared to its initial upright position.

The *Model Linearizer Toolbox* was used to correlate the piston displacement data to joint rotational data obtained after simulating the crane model in Simulink. Their linearized transfer functions at initial conditions for sampling time $T_s = 10\ ms$ are given as:

$$H_{Lift(pist2jnt)} = \frac{-0.05034 * z^{-1} + 0.1047 * z^{-2} - 0.05436 * z^{-3}}{z - 2.988 * z^{-1} + 2.979 * z^{-2} - 0.9907 * z^{-3}}$$

$$H_{Reach(pist2jnt)} = \frac{0.8924 * z^{-1} - 1.858 * z^{-2} + 0.9661 * z^{-3}}{1 - 2.795 * z^{-1} + 2.602 * z^{-2} - 0.8071 * z^{-3}} \quad (3.16)$$

$$H_{Tilt(pist2jnt)} = \frac{9.312z^{-1} - 14.83 * z^{-2} + 5.515 * z^{-3}}{1 - 2.357 * z^{-1} + 2.005 * z^{-2} - 0.6485 * z^{-3}}$$

For the base rotation, a time-delayed motion actuation signal is assumed to directly controls the revolute joint according to transfer function $H_{base} = \frac{1}{1-z^{-1}}$.

The servo valves input commands were set to 0 V to keep the crane in its upright configuration as shown in Figure 3.4. That set the hydraulic pistons in their initial position (half of the hydraulic cylinder stroke length) in order to generate the transfer functions given above.

The above transfer functions are valid however only for the nominal position of the crane in the worst-case sea states. A more in-depth investigation would be necessary to determine the crane dynamics across its entire set of operating points, which depend on its configuration and sea states.

The present study did not require derivation of crane dynamics equations, this step could provide the basis for future work. Crane dynamics are modelled physically in Simulink via its Simscape library. As it will be shown in the following chapter, the algorithms employed to control the system either need simplified equations or a blackbox model. Therefore, it was deemed beyond the scope

of the project to either derive the dynamic equations mathematically or empirically using *Model Linearizer Toolbox* in Matlab.

Given the research focus would be to investigate a control algorithm that requires accurate knowledge of nonlinear crane dynamics, a set of linear parameter-varying (LPV) systems can be developed. For instance, state representation of a nonlinear system via the LPV approach was shown to generate an optimal and robust solution (Grimble and Majecki, 2020, Chapter 10). However, due to the complexity of the LPV approach, the decision was to follow more straightforward and simplistic procedures, which will be presented in Chapter 5.

3.6. Chapter Summary

A hydraulic crane was designed to be 90 m tall, and it could hold and actuate a 660-ton payload placed on a moving base with 4 degrees of freedom (DoF) that can achieve payload translations along the x, y and z axes, as well as rotation about z-axis. The design choices were arbitrary, as the initial purpose was placing the load (nacelle) on top of the wind turbine tower, therefore the need to model such a tall structure. Moreover, it is important to note that only a considerable sized crane could such a heavy load in the range of hundreds of tons. An important aspect to note is that real-life considerations of implementing this particular crane design were not accounted for. Thus, it might be impractical and impossible to manufacture a crane this size for the considered vessel size, and instead a smaller crane could be used. However, a crane of reduced dimensions would imply re-designing the hydraulics and control architecture. Doing that is not trivial and can prove to be a lengthy process until system stability could be ensured. Thus, such work could be covered in a future project due to time constraints.

This chapter also derived the forward kinematics of the crane through the Denavit-Hartenberg method. The inverse kinematics were then computed in Matlab via the Levenberg-Marquardt algorithm.

Crane dynamics were briefly discussed in the last section of this chapter. A simple method to generate the crane dynamics was shown, i.e. *Model Linearizer Toolbox* in Matlab. The transfer functions provided are valid however only for the nominal position of the crane in the worst-case sea states. A more in-depth investigation would be necessary to determine the crane dynamics

across its entire set of operating points, which depend on its configuration and sea states. However, that was deemed to be part of future work. The present algorithms implemented to control the system required either simplified state equations to describe the system hydraulics or a blackbox model.

4. CHAPTER 4: MOTION CONTROL DESIGN

A high-level diagram describing the control implementation within the crane system is presented in Figure 4.1.

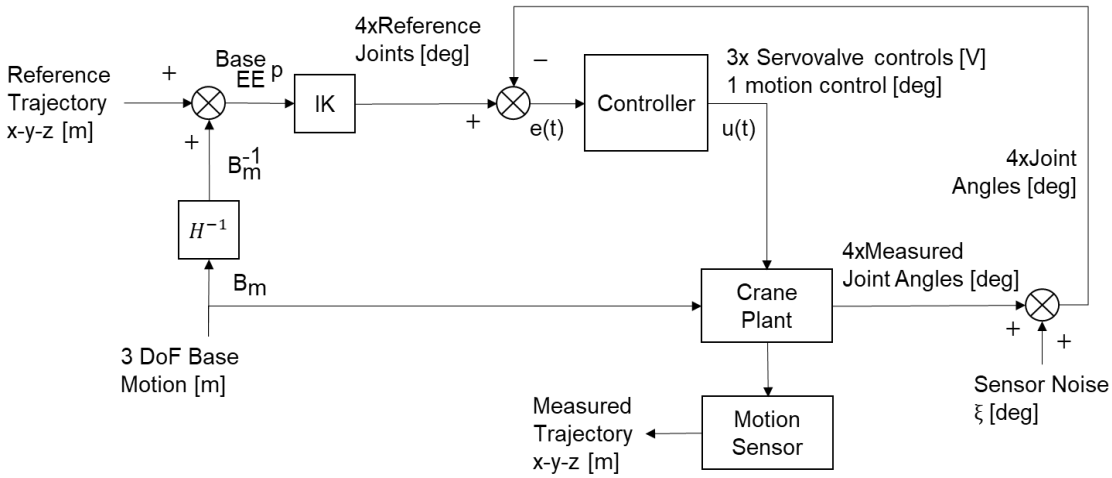

Figure 4.1: High-level diagram consisting of the main components comprised in the control architecture of the crane system

The reference payload trajectory is given only in translations on x-y-z axes without considering any rotations, as stated in Section 3.2. The reason for that was reducing the control task complexity and ensuring translations references could be tracked as best as possible in this scenario. Including rotation tracking would otherwise reduce performance through adding another DoF to be controlled.

The measured trajectory is obtained by placing a virtual motion sensor at the end-effector relative to the fixed world frame that coincides with the initial location of the robot base.

The position vector ${}^{Base}_{EE}p$ describes the translation of the end-effector relative to the robot base as 3-element column vector $[x \quad y \quad z]$; this is obtained by summing the desired payload trajectory and the inverted robot base translations on x, y and z (the compensation of wave motions).

The matrices B_m and B_m^{-1} are the base and inverted base translation matrices that contain column vectors for translations obtained from the MSS toolbox given as: $B_m=[r_x \quad r_y \quad r_z]$ with r_x- surge, r_y – sway, and r_z – heave.

4.1. Traditional Control

4.1.1. Introduction to Feedback and Feedforward Control

Feedback and feedforward controls are used in conjunction to allow compensation for measured and unmeasured disturbances (Mokhatab and Poe, 2012). Feedforward is commonly used in the servo valve control of hydraulic pistons in robotic arms. Given a desired trajectory reference, cylinder velocity, acceleration and jerk can be derived and multiplied by feedforward gain then summed with the PID terms. For example, Küchler and Sawodny (Küchler and Sawodny, 2010) studied a two-stage feedforward control algorithm for active heave compensation. First, a feedforward controller decoupled payload motion from vessel crane tip. Then, a 2 DoF feedforward controller and state feedback were used for trajectory tracking and disturbances stabilisation. This stage considers the time-delay between motions of hydraulic winch and payload due to long rope length. Future work on the research should include an observer-based estimation to remediate undesired payload displacement offset caused by parameter uncertainties.

PID with double derivative

PID is a traditional three-term controller that is widely used in industry due to its simplicity in single-input single-output plants. PID is designed to follow a frequently changing reference signal or to keep a setpoint steady for long periods while rejecting any disturbance (Wilkie et al., 2002). A double derivative term is the gain multiplied by the error in velocity and is used to place a 4th pole over the total closed-loop system (including the controller and the hydraulic system), thus creating the PIDD. A diagram illustrating the double derivative PID control structure is presented in Figure 4.2.

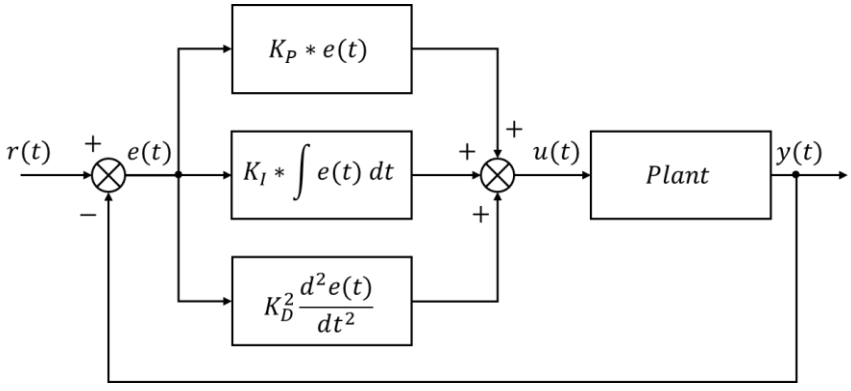

Figure 4.2: Diagram of PID with double derivative control

The components shown in Figure 4.2 are as follows:

$r(t)$ reference signal or set point

$y(t)$ output signal or manipulated variable

$u(t)$ control signal

$e(t)$ error signal, as difference between the reference signal and the output signal

K_P proportional control gain

K_I integral control gain

K_D^2 double derivative control gain

Proportional gain K_P speeds up the response and reduces steady-state (ss) error, integral term K_I eliminates ss error but may lead to overshoot and derivative K_D term acts as a brake and stabilising factor with respect to the integral term. A double derivative term K_D^2 can be included to offer a more precise control by making it possible to place all system poles in the desired locations. That in turn has an influence on the overall system's natural frequency and damping, which would otherwise be dictated by mechanical/hydraulic design only.

The importance of each control component is summarised in Table 4.1.

Table 4.1: Effects of individual PID controller terms

Control Term	**Reference tracking and Disturbance rejection**		**Frequency response**
	Transient	Steady state (ss)	
Proportional, P (Gain, K_P)	Speeds up the response	Reduces ss error	Suitable for low phase plants Gain proportional to K_P No effect on phase
Integral, I (Gain, K_I)	Varying response types	Eliminates ss error	Lifts gain at low frequencies Infinite ss gain and phase lag Unstable

Derivative, D (Gain, K_D)	Tunes response damping	No effect	High gain at low frequencies Phase lead at high frequency
Double Derivative (Gain, K_{DD})	Speeds up the response	No effect	Controls system damping and natural frequency Large gains produce noise

This type of control has been employed in multiple robotics motion control research papers. A position-based impedance controller for a hydraulic robot was proposed in Heinrichs et al., 1996 (Heinrichs et al., 1996) with a nonlinear PI controller to meet accurate positioning requirements; system stability was not discussed however. PD action in impedance control of a teleoperated excavator (Tafazoli et al., 2002 (Tafazoli et al., 2002)) ensured system stability for a single DoF hydraulic cylinder. Another position-based PD control strategy for creating a stable and compliant manipulator was presented in (Lee and Chung, 2017) (Lee and Chung, 2019), accounting for highly dynamic motions that result in unpredictable robot-environment interactions.

Feedforward Control

Feedforward control makes use of a measurable disturbance or reference signal and adjusts the manipulated variable so that tracking errors in the controlled variable are minimized. The controller thus rejects disturbances before they affect the controlled variable. Feedforward and feedback controls are used in conjunction (Figure 4.3) to allow compensation for measured and unmeasured disturbances as well as model mismatch (Mokhatab and Poe, 2012).

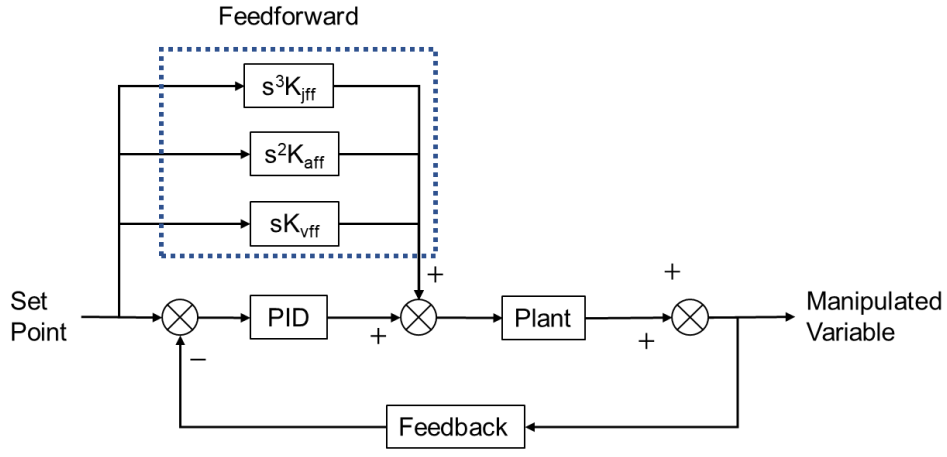

Figure 4.3: Diagram of a feedback and feedforward control system

Feedforward is commonly used in the servo valve control of hydraulic pistons in robotic arms. Given a desired reference trajectory, cylinder velocity, acceleration and even jerk can be derived and multiplied by feedforward gain then summed with the PID terms.

4.1.2. Design of Traditional Control

The feedback and feedforward control design for hydraulic motion control are based upon the second order approximation of the hydraulic cylinder, which can be modelled as a mass between two springs. The transfer function between servo valve input voltage and piston displacement can be written as in eq. (4.1):

$$H_{cyl}(s)=\frac{x_c}{u}=\frac{K*\omega_n^2}{s*(s^2+2*\zeta\omega_n s+\omega_n^2)} \tag{4.1}$$

with damping ζ and natural frequency ω_n

PID with double derivative feedback control

The unfiltered controller transfer function of the PID with double derivative or PIDD is given in eq. (4.2):

$$C_{PIDD}(s)=K_P+\frac{1}{s}K_I+sK_D+s^2K_{DD} \tag{4.2}$$

The closed loop transfer function can be written as:

$$H(s)=\frac{H_{cyl}(s)*C_{PIDD}(s)}{1+H_{cyl}(s)*C_{PIDD}(s)}=\frac{(sK_P+K_I+s^2K_D+s^3K_{DD})K\omega_n^2}{s^4+(2\zeta\omega_n+K\omega_n^2+K_{DD})s^3+(\omega_n^2+K_DK\omega_n^2)s^2+K\omega_n^2K_Ps+K\omega_n^2K_I} \tag{4.3}$$

The response of the characteristic equation (4.3) will be that of a low-pass filter's in series.

Due to the large size of the crane, it is desirable to design a slow response PIDD. Thus, the characteristic equation can be designed with two pairs of real poles (at -λ and -μ):

$$(s+\lambda)^2 * (s+\mu)^2 = s^4 + 2s^3(\mu+\lambda) + s^2(\mu^2 + 4\mu\lambda + \lambda^2) + 2s(\mu^2\lambda + \mu\lambda^2) + \mu^2\lambda^2 \quad (4.4)$$

Equating the coefficients for each power of s between the actual characteristic equation in (4.3) and the desired characteristic equation (4.4) gave the PIDD gains:

$$K_I = \lambda^2 \frac{\mu^2}{K\omega_n^2};\ K_P = 2\lambda\mu \frac{\mu+\lambda}{K\omega_n^2};\ K_D = \frac{2\lambda\mu^2 + 2\lambda^2\mu - \omega_n^2}{K\omega_n^2};\ K_{DD} = 2\frac{\mu+\lambda-\zeta\omega_n^2}{K\omega_n^2} \quad (4.5)$$

For stability, the following condition needs to apply: $\lambda + \mu \geq \zeta * \omega_n$. If λ is small, μ should be large enough so that K_d and K_{dd} are not negative. However, $e^{-\lambda t}$ will take longer to decay to zero so the response will be slower given changes in target positions and disturbances. If λ increases, then μ should decrease; the fastest response will occur when $\lambda = \mu = \frac{\zeta\omega_n}{2}$.

Feedforward control design

The ideal feedforward control gains can be extracted from the inverted transfer function of the hydraulic cylinder from eq. (4.1) as follows in eq. (4.6):

$$u_{FF} = H_{cyl}^{-1}(s)x_c = \frac{s(s^2 + 2\zeta\omega_n s + \omega_{n)}^2}{K\omega_n^2}x_c = \frac{1}{K}sx_c + \frac{2\zeta}{K\omega_n}s^2x_c + \frac{1}{k\omega_n^2}s^3x_c \quad (4.6)$$

with feedforward velocity gain, $K_v = \frac{1}{K}x_c$; feedforward acceleration gain, $K_a = \frac{2*\zeta}{K*\omega_n}x_c$; feedforward jerk gain, $K_j = \frac{1}{K\omega_n^2}x_c$; feedforward steady-state slope, $K = \frac{v_c}{u}$

A real system cannot be precisely modelled. Implementing the ideal feedforward controller could result in reference tracking errors due to model mismatch. System mismatch was created by introducing various levels of uncertainty on system parameters described in eq. (3.10) in order to modify the hydraulic/mechanical systems response to be then controlled.

While PIDD parameters can be tuned to minimize the errors caused by model mismatch, an optimal controller needed to be implemented to tackle the challenge created by the high dynamic

nonlinearities of the crane system. The next section will review possible options to be implemented on the crane prototype.

4.2. Advanced Control

4.2.1. Introduction

A review of selected advanced control architectures will be presented over the following subsections as part of this chapter introduction. The main reason for choosing these particular controllers is their applicability on industrial systems, which is the case of the current crane plant. One of the listed algorithms will be implemented on the system studied in the present work.

Linear and Nonlinear Model Predictive Control

In many industries, model predictive control is employed to deliver optimal plant performance by optimising setpoints, reducing interaction effects and improving control systems responses. In this type of algorithm, a dynamic model of the plant is used to predict and optimise the future outputs of the process (Grimble and Majecki, 2020 Chapter 7 (Grimble and Majecki, 2020)).

1. Linear model predictive control (MPC)

MPC is an advanced control technique widely accepted in industry due to its simplicity, easy tuning on linear systems and supervisory mode that acts as a switch off. This type of controller handles multivariable control problems, accounts for actuator limitations and allows operation close to constraints (Maciejowski, 2002).

This type of predictive control calculates the output of a linear discrete system model over a “prediction horizon” based on the current and past states of the plant (see diagram Figure 4.4 for a visual representation).

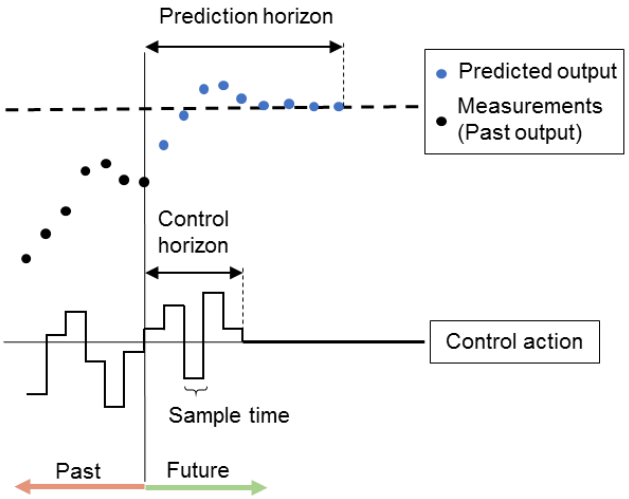

Figure 4.4: Diagram describing the principle of model predictive control

An optimal control sequence is found by minimising a cost function *J* (usually quadratic) that consists of tracking performance and control effort. The optimal solution is subject to constraints on the input (e.g. actuator force constraints) and on the predicted output.

$$J(t) = \sum_{j=N_1}^{N_2} [\hat{y}(t+j|t) - r(t+j)]^2 + \lambda \sum_{j=0}^{N_u-1} \Delta u(t+j)^2 \tag{4.7}$$

where:

$N = N_2 - N_1$	prediction horizon
N_u	control horizon
$\hat{y}(t+j\|t)$	predicted/estimated outputs with current time t
$r(t+j)$	reference trajectory
λ	control weighting
$\Delta u(t+j)$	future control increments to be computed

MPC is a preferred technique employed in multiple research studies. A comparison between the effects of three linear controllers on a linearised model of a helicopter landing on a ship was presented in (Sandino et al., 2011) (similar to the application of this study). The authors concluded that MPC outperformed Linear Quadratic Integral control (LQI) and Loop-Shaping Design (LSD) in achieving a smooth landing despite complex trajectories caused by vessel movements.

MPC could also be utilized in solving force control problems. In their study, Heybroek and Sjöberg have cascaded a force index controller (FIC) with an MPC in a four cylinder chamber hydraulic actuator system (Heybroek and Sjöberg, 2018). The challenge was to achieve accurate force control (MPC part) while preserving energy efficiency as FIC acted as a feed-forward filter to calculate pressure references used as inputs to the MPC.

2. Nonlinear Model Predictive Control (NMPC)

Often, the operation of a process requires frequent changes from one operation point to another and, therefore, a Nonlinear Model Predictive Control could be employed (Camacho and Bordons, 2007). The reason for adopting a nonlinear MPC is because the underlying system dynamics are nonlinear and cannot adequately be captured through linearisation.

Since the predicted system behavior will in general differ from the closed-loop one, precaution must be taken to achieve closed-loop stability and reasonable closed-loop performance. As in traditional linear MPC, nonlinear MPC calculates control actions at each control interval using a combination of model-based prediction and constrained optimization. The key differences are:

- The prediction model can be nonlinear and include time-varying parameters.
- The equality and inequality constraints can be nonlinear.
- The scalar cost function to be minimized can be a nonquadratic (linear or nonlinear) function of the decision variables.

The principle of operation is similar to MPC; this iterative process measures the system states, then computes an optimal input signal by minimising an on-line performance criterion over a prediction horizon and updates once new state estimates are available (Findeisen and Allgöwer, 2002). Summarizing, a standard NMPC scheme works as follows:

1) Obtain estimates of the states of the system.
2) Calculate an optimal input minimizing the desired cost function over the prediction horizon using the system model for prediction.
3) Implement the first part of the optimal input until the next sampling instant.
4) Continue with (2).

The overall structure of a NMPC control loop is illustrated in Figure 4.5.

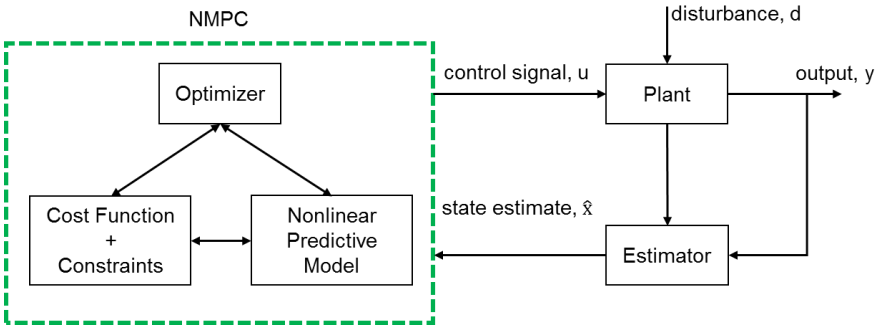

Figure 4.5: Basic structure of nonlinear model predictive control

As shown in (De Zeeuw, 2012), this type of control was suitable in the case of a system with a vessel and a 3 DoF motion compensation Sarrus platform (heave-roll-pitch) for high payloads. The research thesis integrated nonlinearities resulted from the kinematics and dynamics of the vessel and of the robotic manipulator, the mechanical coupling between vessel and platform, hydrodynamics frequency dependency and hydrostatics. The outcome of the study was that NMPC performed better in terms of stability and energy efficiency than a naïve quasi-static controller when applied to the system.

Nonlinear Generalised Minimum Variance Control

The Nonlinear Generalised Minimum Variance (NGMV) control was developed for nonlinear multivariable processes in both state-space and polynomial versions (Grimble, 2006). This scheme is employed to compensate for the nonlinearities in all relevant parts of the model. NGMV control applied for state dependent multivariable models (Grimble and Majecki, 2015) involves the plant nonlinearities directly and does not rely on linearization techniques as opposed to some other nonlinear controllers. This controller structure includes a delay free exact model of the plant, and error and the control weightings that addresses the mismatch with the actual plant.

The structure of the system and the cost-function are chosen so that a simple feedback controller and solution are obtained. The nonlinear optimal control problem considered here is defined so that the resulting NGMV control solution is straightforward to implement. That is a priority considered in the case of industrial applications even before performance requirements were considered.

A high-level diagram of the NGMV controller is presented in Figure 4.6.

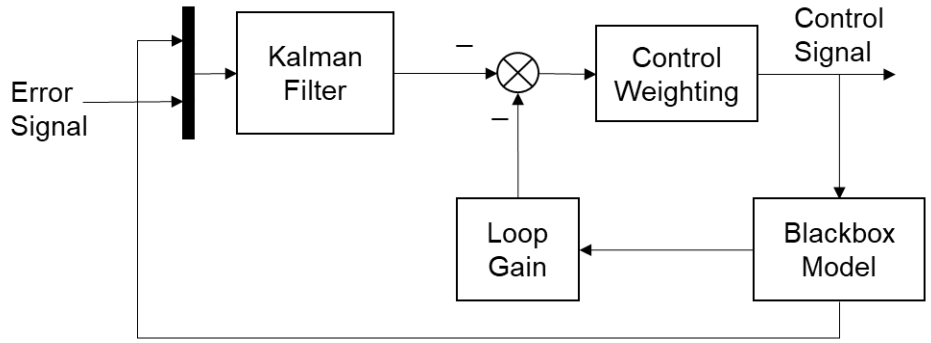

Figure 4.6: Simplified architecture of the nonlinear generalised minimum variance controller

The main blocks shown in Figure 4.6 are described below:

Kalman filter

A Kalman filter can be used as a recursive algorithm for state estimation, which is described in Chapter 15 (Grimble and Majecki, 2020). System states cannot be usually measured (due to noisy measurements of the system output) but can be estimated using a state observer such as the Kalman filter.

Kalman filter is very robust and reliable across various industrial sectors, as process models and noise variances do not have to be entirely known. Even with large errors in noise and disturbance variance estimates, performance of the filter remains unaffected. Filter's prediction performance can deteriorate when significant mismatch occurs between the modelled system dynamics and the nominal plant.

Loop Gain

The optimal control problem involves the minimization of a cost function that is based on the loop gain design, which is based on the selection of the dynamic weighting; this will be discussed in section 4.2.2.

Control weighting

The control weighting is a nonlinear operator which is normally chosen to be linear and has a high-pass characteristic. It is assumed to be normal full rank and to be invertible. The weighting will

often be chosen to be a linear operator and can be used to compensate for the plant input nonlinearities.

Black-box model

The model is defined as a combination of finite-gain stable nonlinear input subsystem and a linear output subsystem. All that is needed is the ability to compute an output for a given input to this subsystem.

The choice to study the nonlinear GMV control architecture for the present work was determined by the following list of properties which make it a better choice than other nonlinear controllers (Grimble and Majecki, 2020, Ch 4).

Black box model: The plant model can be in a very general nonlinear operator form, which is unusual for a model-based control approach. This model can include non-smooth and severe static nonlinearities, complex nonlinear dynamic equations, nonlinear state-space equations and transfer-operators (Isidori, 1995). It might represent valves, or a servo-system with a software model but not in a known equation form. The optimal solution reveals that the model equations do not need to be known within this subsystem. However, due to minimal information, this subsystem must be assumed open-loop stable if closed-loop stability is to be ensured. The possibility of introducing a very general plant subsystem is a key advantage of the method.

Simplicity and properties: A major advantage is that the solution is very simple, which is a feature that only applies to a few nonlinear control methods such as feedback linearization (Goodwin et al., 2001, Ch.1). However, feedback linearization methods do not provide a general solution for disturbance rejection and tracking. An advantage of the NGMV solution is that it relates to a wider class of problems. For example, the plant model does not need to be affine in the control. A nonlinear system in which the control appears linearly is called a control/input-affine nonlinear system or simply control/input-affine system, where the nonlinearity with respect to the state is automatically implied.

4.2.2. NGMV Control

System Description

Given its features presented in section 4.2.1, the nonlinear generalised minimum variance control was chosen as the advanced control technique to be investigated as part of the current research.

The architecture of NGMV control is illustrated in Figure 4.7. The NGMV controller diagram along with its description, equations and components explanations were extracted from Grimble and Majecki, 2020.

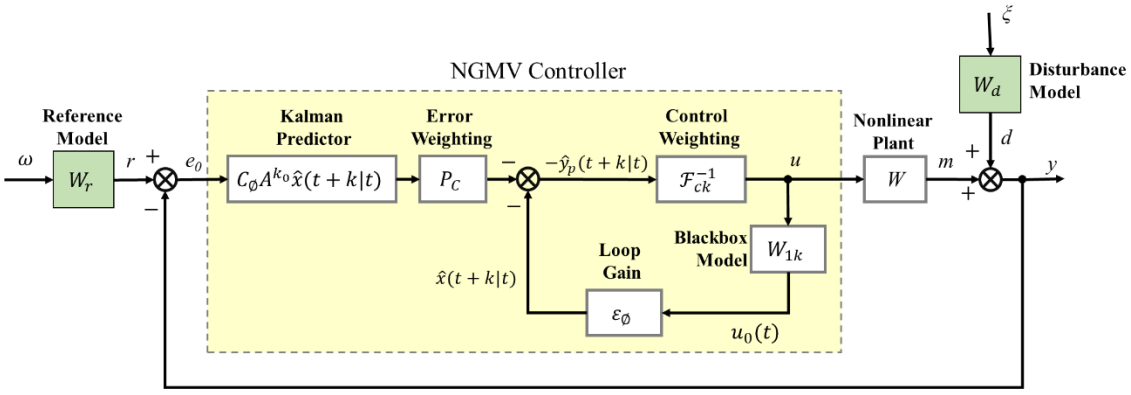

Figure 4.7: NGMV control loop architecture

The blocks presented in the diagram above, Figure 4.7, are:

- Linear reference model, W_r
- Disturbance model, W_d
- Nonlinear plant model, W
- NGMV controller architecture consists of the following:
    - Kalman predictor, $C_\emptyset A^{k_0}\hat{x}(t+k|t)$
    - Control weighting, F_{ck}^{-1}
    - Blackbox model, W_{1k}
    - Loop gain, $\varepsilon_\emptyset$

The reference (r) and disturbance (d) signals are assumed to have linear time-invariant model representations. This is often valid since in many applications the stochastic disturbance and

reference signals are represented by Linear Time-Invariant (LTI) approximations. The zero-mean white noise source $\xi(t)$ has identity covariance matrices so it does not result in a loss of generality.

The plant system W can be nonlinear and can be defined as two cascaded subsystems. Thus, the plant model can be separated into a nonlinear input subsystem W_{1k} and a linear output subsystem W_{0k}. In the case of a multivariable system, this output subsystem often contains the main system interactions.

In an open loop unstable plant, the input nonlinear subsystem W_{1k} contains the stable modes. Any unstable modes of the linear plant subsystem are included in a linear time-invariant block of state-space matrix form $W_{0k} = A^{-1}B_{0k}$. This approach enables open-loop unstable processes to be stabilised.

The operator forms of the plant model can be introduced as:

Delay free plant model $$(W_{1k}u_k)(t) = W_{0k}(W_{1k}u)(t) = A^{-1}B_{0k}(W_{1k}u)(t) \quad (4.8)$$

where $u(t)$: control signal

Total plant model $$(Wu)(t) = z^{-k}W_{0k}(W_{1k}u)(t) \quad (4.9)$$

The input subsystem nonlinear model W_{1k} is assumed to be finite-gain stable. There is some loss of accuracy in assuming that the reference and disturbance models are represented by linear subsystems, but this is normally acceptable. The signals shown in the system model of Figure 4.7 may be defined as:

Error signal $$e(t) = r(t) - y(t) \quad (4.10)$$

Plant output $$y(t) = d(t) + (Wu)(t) \quad (4.11)$$

Reference $r(t) = W_r\omega(t)$ (4.12)

Disturbance signal $d(t) = W_d\xi(t)$ (4.13)

The crane model is defined as:

$$(Wu)(t) = z^{-k}\, W_{0k}(W_{1k}u)(t) \tag{4.14}$$

where W_{1k} is finite-gain stable nonlinear input subsystem and W_{0k} is the linear output subsystem (and it can be designed to be unstable). In this case, let W_{1k} describe the entire crane system as a black-box model term and $W_{0k} = I_4$ (4 x 4 identity matrix to match the four-input four-output crane system).

Signal definitions

Assume that the outputs to be controlled are different to the actual measured outputs. Thus, consider the output $y(t)$ includes the deterministic $d(t)$ as well as a stochastic $y_d(t)$ components of the disturbance. Hence, the total disturbance is $d_0(t) = d(t) + y_d(t)$.

Let a zero-mean white measurement noise on the measured output be denoted by $v_m(t)$, with a covariance matrix R_m. The measured output is then $z_m(t) = y_m(t) + v_m(t)$.

The control output $y(t)$ is required to follow a reference signal $r_0(t)$, which is assumed to consist of a stochastic component $r(t)$ and a known set-point component $r_d(t)$. The total reference signal $r_0(t) = r(t) + r_d(t)$ may be corrupted by a zero-mean measurement noise $v_r(t)$ with covariance matrix R_r. Assume that the reference signal is known p-steps into the future, where $p \geq 0$.

The measured output $y_m(t)$, which could be different to the controlled output $y(t)$, includes deterministic $d_m(t)$ and stochastic $y_{dm}(t)$ components of the disturbance signal, so the total disturbance is expressed as $d_{0m}(t) = d_m(t) + y_{dm}(t)$.

Note: For simplicity, the stochastic signals as well as the measured signals for each of the above (input, output and disturbance) were not included in Figure 4.7. However, they were introduced in Figure 4.8.

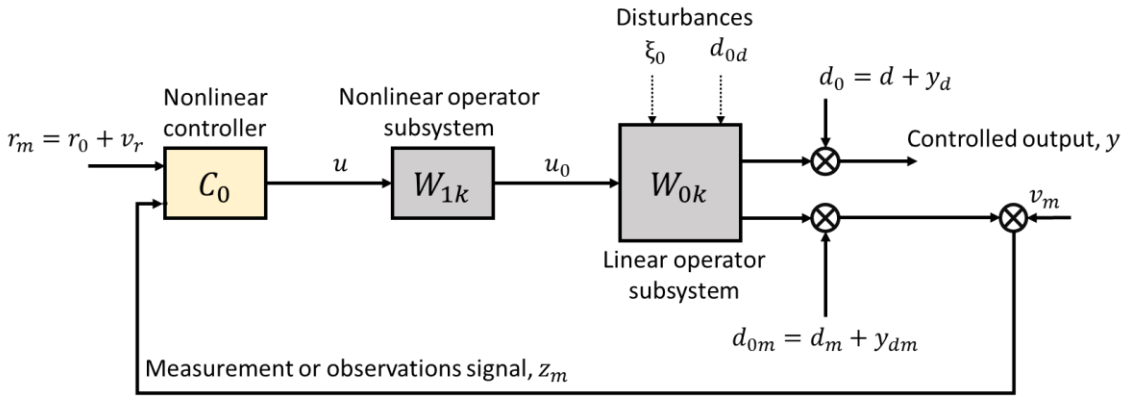

Figure 4.8: Feeback control system for a nonlinear plant model with the reference and disturbance signals

The signals in Figure 4.8 and considered in the formulation of the Kalman filter estimation used in the NGMV control scheme are defined as follows:

$x_0(t)$	Vector of n states in plant subsystem and the input disturbance model
$u_0(t)$	Vector of m_0 input signals to the qLPV subsystem
$u(t)$	Vector of m control signals applied to the nonlinear subsystem
$y(t)$	Vector of r plant output signals to be controlled
$d(t)$	Vector of r deterministic disturbance signal values on the controlled output
$y_d(t)$	Vector of r stochastic disturbance signal values on the controlled output
$y_m(t)$	Vector of r_m plant output signals that are measured
$d_m(t)$	Vector of r_m deterministic disturbance signal values on the measured output
$y_{dm}(t)$	Vector of r_m stochastic disturbance signal values on the measured output
$z_m(t)$	Vector of r_m observations on the measured plant outputs
$r_0(t)$	Vector of r setpoint or reference signal values
$d_0(t)$	Vector of r known output-disturbance signal values
$d_{0d}(t)$	Vector of q known input-disturbance signal values

Tracking control and reference generation

The optimal control solution will apply to the tracking of either stochastic or deterministic reference or setpoint signals. The future values of the reference signal are known for *p* time steps ahead. The noise-free signal $r_o(t+p)$ denotes the desired future values of the reference signal *p* steps ahead.

The model for the stochastic component of the reference $r(t+p)$ is driven by zero-mean white-noise $\omega_r(t)$, and is determined by the state equation modelled subsystem:

Reference state model
$$x_{r0}(t+1) = A_{r0}x_{r0}(t) + D_{r0}\omega_{r0}(t), x_{r0}(t) \in \mathbb{R}^{n_{r0}} \quad (4.15)$$

Stochastic component of reference
$$r(t+p) = C_{r0}x_{r0}(t) \quad (4.16)$$

The future stochastic components of the reference model may be collected in:

Future reference model
$$x_r(t+1) = A_r x_r(t) + D_r\omega_r(t), x_{r0}(t) \in \mathbb{R}^{n_{r0}}$$
$$r(t+p) = C_{r0}x_{r0}(t) = C_r x_r(t) \quad (4.17)$$

The noise-corrupted measurement of the stochastic and deterministic components of the future reference signal may be written as:

$$r_m(t+p) = v_r(t) + C_{r0}x_{r0}(t) + r_d(t+p) = v_r(t) + C_r x_r(t) + r_d(t+p) \quad (4.18)$$

Error and observation signals

The error tracking of the signal is given by:

$$e(t) = r_o(t) - y(t) = x_{rp}(t) + r_d(t) - y(t) = C_{rp}x_r(t) + r_d(t) - y(t) \quad (4.19)$$

with the matrix to pick out the reference at the current time $C_{rp} = [0 \quad ... \quad 0 \quad I]$.

The plant observation signal is:

$$z_m(t) = y_m(t) + v_m(t) \tag{4.20}$$

Then, the weighted tracking error may be implemented in state-equation form:

$$x_P(t+1) = A_P x_P(t) + B_P e(t), x_P \in \mathbb{R}^{n_p} \tag{4.21}$$

$$e_P(t) = C_P x_P(t) + \varepsilon_P e(t) \tag{4.22}$$

Total augmented system

Given the relationship between the augmented system matrices for the plant, disturbance, reference and weightings derived in Ch.10 (Grimble and Majecki, 2020), the state equation of the total system is:

$$\begin{bmatrix} x_0(t+1) \\ x_d(t+1) \\ x_r(t+1) \\ x_p(t+1) \end{bmatrix} = \begin{bmatrix} A_0 & 0 & 0 & 0 \\ 0 & A_d & 0 & 0 \\ 0 & 0 & A_r & 0 \\ -B_P C_0 & -B_P C_d & B_P C_{rp} & A_P \end{bmatrix} \begin{bmatrix} x_0(t) \\ x_d(t) \\ x_r(t) \\ x_P(t) \end{bmatrix} + \begin{bmatrix} B_0 \\ 0 \\ 0 \\ -B_P \varepsilon_0 \end{bmatrix} + \\ + \begin{bmatrix} D_0 & 0 & 0 \\ 0 & D_d & 0 \\ 0 & 0 & D_r \\ 0 & 0 & 0 \end{bmatrix} \begin{bmatrix} \xi_0(t) \\ \omega_d(t) \\ \omega_r(t) \end{bmatrix} + \begin{bmatrix} G_0 & 0 \\ 0 & 0 \\ 0 & 0 \\ 0 & B_P \end{bmatrix} \begin{bmatrix} d_{0d}(t) \\ r_d(t) - d(t) \end{bmatrix} \tag{4.23}$$

The above may be written as:

$$x(t+1) = A_t x(t) + B_t u_0(t-k) + D_t \xi(t) + d_d(t) \tag{4.24}$$

where: $A_t = \begin{bmatrix} A_0 & 0 & 0 & 0 \\ 0 & A_d & 0 & 0 \\ 0 & 0 & A_r & 0 \\ -B_P C_0 & -B_P C_d & B_P C_{rp} & A_P \end{bmatrix}, B_t = \begin{bmatrix} B_0 \\ 0 \\ 0 \\ -B_P \varepsilon_0 \end{bmatrix}, D_t = \begin{bmatrix} D_0 & 0 & 0 \\ 0 & D_d & 0 \\ 0 & 0 & D_r \\ 0 & 0 & 0 \end{bmatrix}, G_t = \begin{bmatrix} G_0 & 0 \\ 0 & 0 \\ 0 & 0 \\ 0 & B_P \end{bmatrix}$

and $d_d(t) = G_t \begin{bmatrix} d_{0d}(t) \\ r_d(t) - d(t) \end{bmatrix} = \begin{bmatrix} G_0 d_{0d}(t) \\ 0 \\ 0 \\ B_P(r_d(t) - d(t)) \end{bmatrix}$

Kalman filter

The Kalman predictor stage is required so that the predicted values of the weighted error and control signal may be obtained. GMV and NGMV state estimates solutions can be computed via a Kalman filter as part of a feedback control loop. The Kalman estimator uses the plant, the disturbance model states as well as the states of the dynamic cost-function weightings to estimate system states.

The i-step predicted state, noting the stochastic disturbance is zero-mean, can be expressed as:

$$\hat{x}(t+i|t) = A_t^k \hat{x}(t|t) + \sum_{j=1}^{k} A_{t+j}^{i-j} B_{t+j-1} u_0(t+j-1-k) + d_{dd}(t+i-1) \tag{4.25}$$

where

$A_{t+j}^{i-j} = A_{t+i-1} A_{t+i-2} \dots A_{t+j}$ and $d_{dd}(t+i-1) = \sum_{t+j}^{k-j} d_d(t+j-1)$, but if i= 0, define $d_{dd}(t-1) = 0$.

The k-step predicted weighted error is given as:

$$\hat{e}_p(t+i|t) = d_P(t+i) + C_{P_{t+k}} \hat{x}(t+i|t) + \varepsilon_{P_{t+k}} u_0(t+i-k) \tag{4.26}$$

The Kalman filter input involves the noisy plant observations, $z_m(t)$ and the measured reference signal, $r(t)$. For the design of the filter, the combined observations signal:

$$z(t) = \begin{bmatrix} z_m(t) \\ r_m(t+p) \end{bmatrix} = \begin{bmatrix} v_m(t) + d_m(t) + C_m^t x(t) + \varepsilon_t^m u_0(t-k) \\ v_r(t) + r_d(t+p) + C_r x_r(t) \end{bmatrix} \tag{4.27}$$

The total observations input to the filter may now be written as:

$$z(t) = v(t) + d_f(t) + C_t^f x(t) + \varepsilon_t^f u_0(t-k) \tag{4.28}$$

where

$$v(t) = \begin{bmatrix} v_m(t) \\ v_r(t) \end{bmatrix}, \qquad d_f t(t) = \begin{bmatrix} d_m(t) \\ r_d(t) \end{bmatrix}, \qquad C_t^f = \begin{bmatrix} C_m & C_{dm} & 0 & 0 \\ 0 & 0 & C_r & 0 \end{bmatrix}, \qquad \varepsilon_t^f = \begin{bmatrix} \varepsilon_t^m \\ 0 \end{bmatrix} \tag{4.29}$$

The process and measurement noise covariance matrices have the form:

$$Q_t^f = diag\{Q_0, Q_d, Q_r\} \text{ and } R_t^f = diag\{R_m, R_r\}$$

Note: If the stochastic component of the reference is zero the corresponding covariance can be set to zero. Similarly, if there is no measurement noise on the reference, the covariance can be set to zero. However, a small measurement noise covariance for the reference may help the numerical solution for the filter gain. In practical applications, the covariance matrices Q_d, Q_r, R_r may often be treated as tuning variables (depending on the application involved).

The computation of the *Kalman filter* for state-estimation is similar to those for a known time-varying linear system if the states determining the state matrices are assumed known.

The augmented plant model is given as:

$$x(t+1) = A_t x(t) + B_t u_0(t-k) + D_t \xi(t) + d_d(t) \tag{4.30}$$

The observation signal:

$$z(t) = v(t) + d_f(t) + C_t^f x(t) + \varepsilon_t^f u_0(t-k) \tag{4.31}$$

Optimal control signal

Theorem: The nonlinear operator of the generalised plant ($P_c W_k - \mathcal{F}_{ck}$) is assumed to have a stable causal inverse, due to the choice of weighting operators P_c and $\mathcal{F}_c$. The NGMV optimal controller is required to minimise the variance of the weighted error and control signals (Grimble and Majecki, 2020, Ch. 8).

The optimal control problem involves the minimization of the cost function:

$$J = E\{\phi_0^T(t+k)\phi_0(t+k)|t\} \tag{4.32}$$

where:

$$\phi_0(t) = P_c(z^{-1})e(t) + (\mathcal{F}_c u)(t) \tag{4.33}$$

with

error signal $e(t)$, error weighting $P_c(z^{-1}) = P_{cd}^{-l}(z^{-1})P_{cn}(z^{-1})$ as a low-pass transfer function, control signal $u(t)$ and control weighting $\mathcal{F}_c(u)(t) = z^{-k}(\mathcal{F}_{ck}u)(t)$ as a high-pass transfer function.

The cascade compensator and the loop gain are dictated by the selection of the reference model W_r, disturbance model W_d, linear subsystem W_{0k}, error weighting and control weighting.

The reference model was defined as a near integrator, which is the stochastic equivalent of step reference changes in the input payload trajectory:

$$W_r = \frac{1}{1 - n_{int} * z^{-1}} * I_4 \tag{4.34}$$

where $n_{int} = 0.9999$ and is the near-integrator term.

The disturbance model was written as a 2nd order system to match the wave motion profiles:

$$W_d = \frac{1}{\frac{1}{\omega_n}s^2 + \frac{2 * \zeta}{\omega_n}s + 1} * \frac{1}{n_{int} * s} \tag{4.35}$$

with natural frequency equal to wave frequency, ω_n = 1 rad/s and an arbitrary selected damping $\zeta = 0.5$.

A near-integrator term was also added to account for unmeasured output disturbances.

Dynamic weightings

The properties of the NGMV controller are often critically dependent on the selection of the dynamic cost-function weightings P_c and $\mathcal{F}_{ck}$ (Grimble and Majecki, 2020, Ch. 5).

The error weighting was designed based on tuning the PID parameters determined in the previous experiments (Section 4.1) for each actuator. Thus, a transfer function can be created:

$$C(z^{-1}) = K_P + \frac{K_I}{1 - n_{int} * z^{-1}} + K_D * (1 - z^{-1}) \tag{4.36}$$

The formula for control weighting is given as:

$$F_{ck}(z^{-1}) = -\frac{\rho(1 - \gamma z^{-1})}{1 - \gamma} \tag{4.37}$$

with:

ρ positive scalar; reducing ρ produces a faster response and a more aggressive control action

γ a lead term that influences controller's high frequency gain, $\gamma \in [0,1]$; $\frac{1}{1-\gamma}$ term decouples the lead term from the overall gain.

4.3. Payload Position Control Results

Simulations of the crane system were run in Simulink with each of the controllers used in the loop, i.e. with traditional (feedback and feedforward) and NGMV. Initially, the nominal case is considered where the plant to be controlled is identical to the system model the controller was designed for. Then, a sensitivity analysis was carried out to verify the robustness of each controller against model mismatch. Various levels of uncertainty (10%, 20% and 40%) were introduced to the hydraulic fluid bulk modulus, cylinder radius, valve area and links and payload masses. These alterations in the crane design directly influence actuators' natural frequency and therefore, by tuning controllers' parameters, system sensitivity can be assessed.

4.3.1. Preliminary Results – Nominal Case

The four joint rotations reference tracking are displayed in Figure 4.9, while the error between the desired and measured outputs (joint angles) are displayed in Figure 4.10.

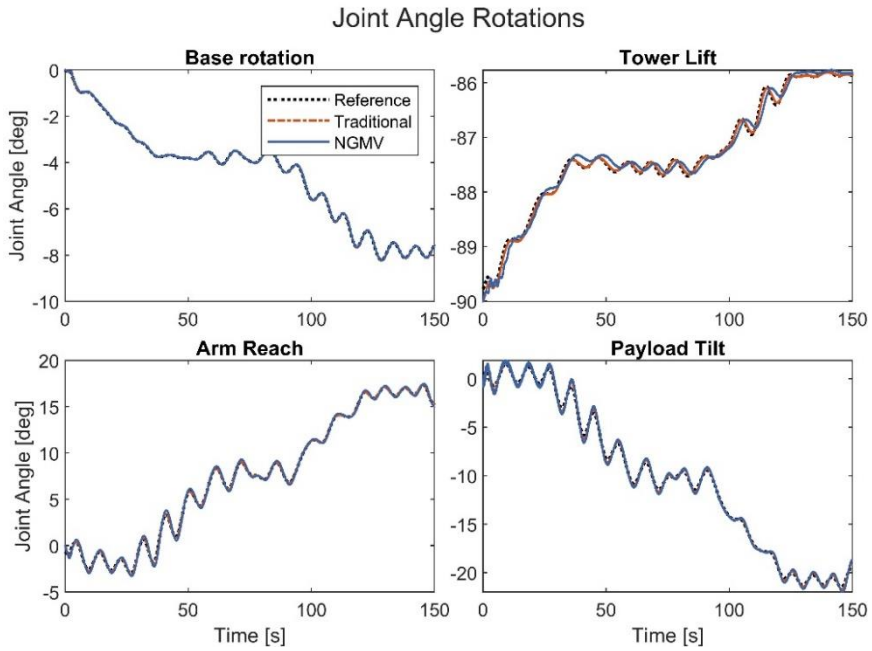

Figure 4.9: Joint rotations reference tracking comparison between traditional control and NGMV control

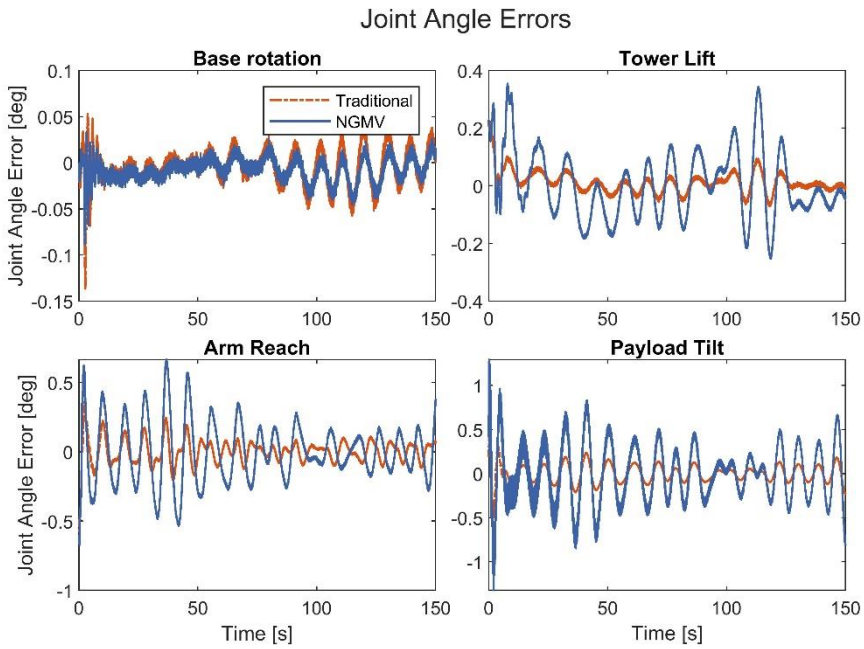

Figure 4.10: Joint angles errors comparison between traditional control against NGMV control

The recorded payload trajectory was taken with respect to the fixed reference frame. The payload motion was displayed as a 3D profile -Figure 4.12 and for each independent axis -Figure 4.11.

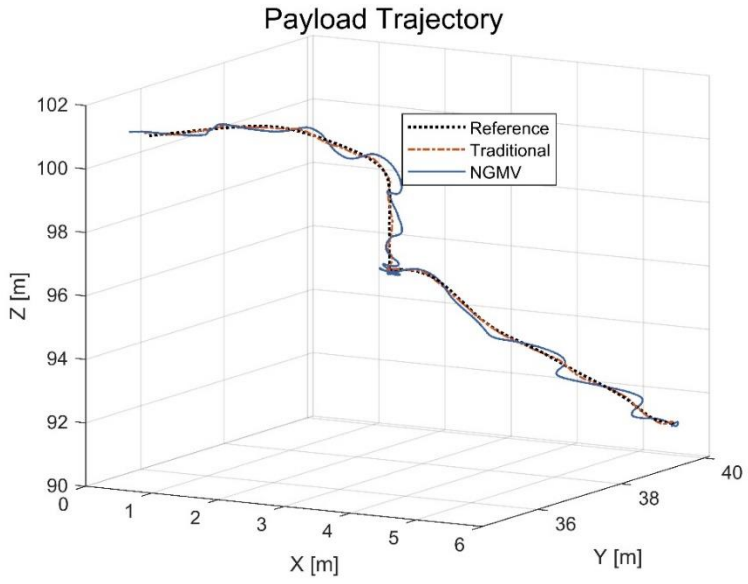

Figure 4.11: Measured payload 3D trajectory relative to the fixed reference frame

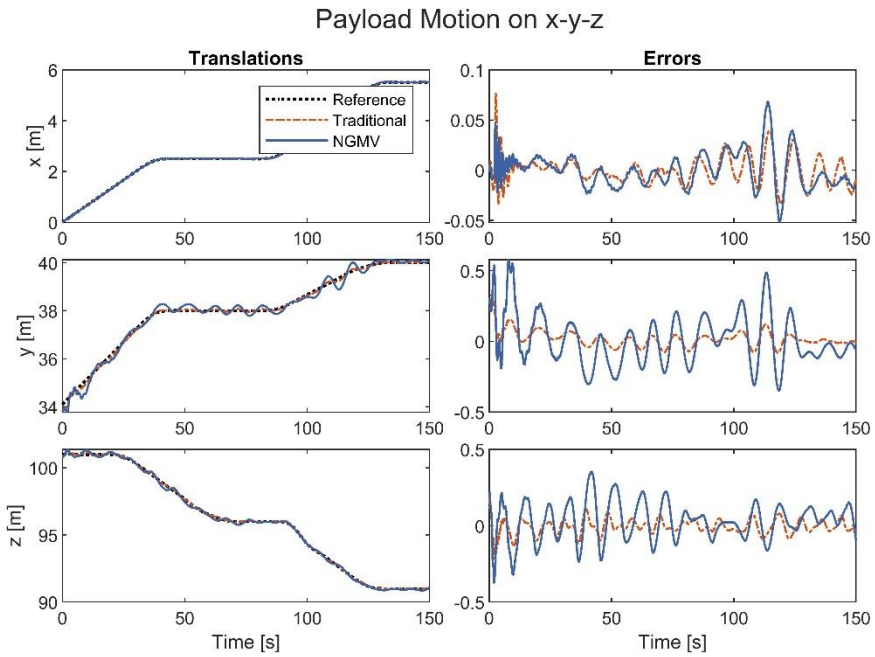

Figure 4.12: Measured payload motion compared against the expected motion on each of the x, y, and z axes

The simulations results for the nominal case were presented in Figure 4.9 - Figure 4.11, where no model mismatch was introduced (i.e. no unceratainties in model parameters). From these plots, it seemed that controllers performance was similar in most part. The traditional controller had a slightly larger overshoot but then reached a steady-state error somewhat smaller than the NGMV controller.

Note that the 60% and 20% initial overshoot (OS) of the traditional controller and NGMV controller respectively on the the *Tower Lift* actuator joint rotation (Figure 4.10) were due to the piston having to support the largest load of the crane system as well as the payload. Similarly, the NGMV controller showed a significant 80% OS on the *Arm Reach* joint, while the traditional controller produced only a 25% OS. This could be expected in a real-life application as well given the dynamics involved. Furthermore, one can simply disregard that initial OS until the motion controller stabilises and positioning could be done safely. This could be explained as at that initial stage of simulation, the wave-induced vessel data had a highly nonlinear profile which signficantly contributed to the degradation in controller performance. Hence, the 1m error (for traditional control) and 50 cm error (associated with NGMV control) seen in the first 5 seconds of simlation on the y-axis (Figure 4.12) showed a decent controller action given the above reasons. Finally, it

is worth mentioning that the payload positioning on x-y-z axes stayed within 20 cm error for most part of the 150 simulated seconds in both controllers.

This set of simulations for the nominal case will serve as a reference to which the experiments in the following sections are going to be compared against. The next sets of results were obtained while introducing six levels of hydraulic system parameters uncertainties. The controllers had to be retuned to compensate for the model mismatch and their performance was reflected in the payload positioning task.

As shown in equation (3.10), hydraulic parameters can be modified to alter the system's natural frequency. A fluid with a larger bulk modulus, larger piton areas (but smaller fluid volumes) and a reduced load mass, all result in increased ω. The aim of the following subsections was to assess eq. (3.10), by introducing 10%, 20% and 40% levels of uncertainty to the above parameters. Furthermore, according to eq. (3.10), these parameters are uncoupled to each other and therefore only the extremals were considered.

A more in-depth assessment of the investigated experiments will be provided in the Section 4.3.5. The results for the payload positioning controller schemes will be analysed, thus determining which of the two had the better perforamance.

4.3.2. Mismatch Level 10%

10% mismatch below nominal case

The values of hydraulic fluid bulk modulus and piston area were first increased by 10% while the links and payload masses were decreased by 10% to offset the overall response of the transfer function below nominal setting. Running simulations with each controller, their performance can be observed in Figure 4.13 and Figure 4.14.

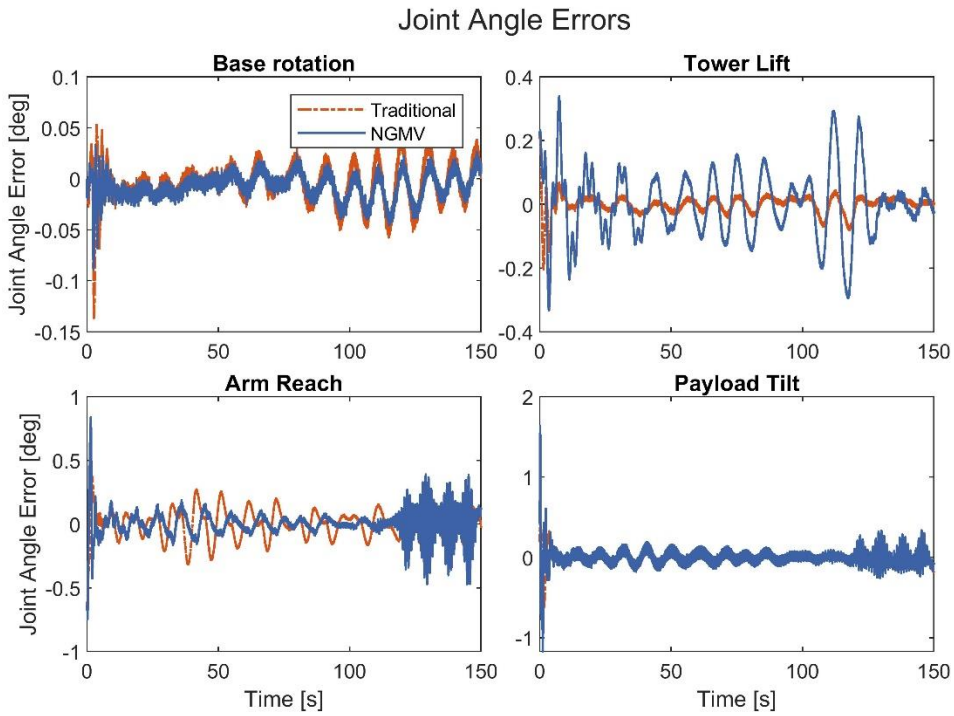

Figure 4.13: Errors in reference tracking for each individual joint rotation

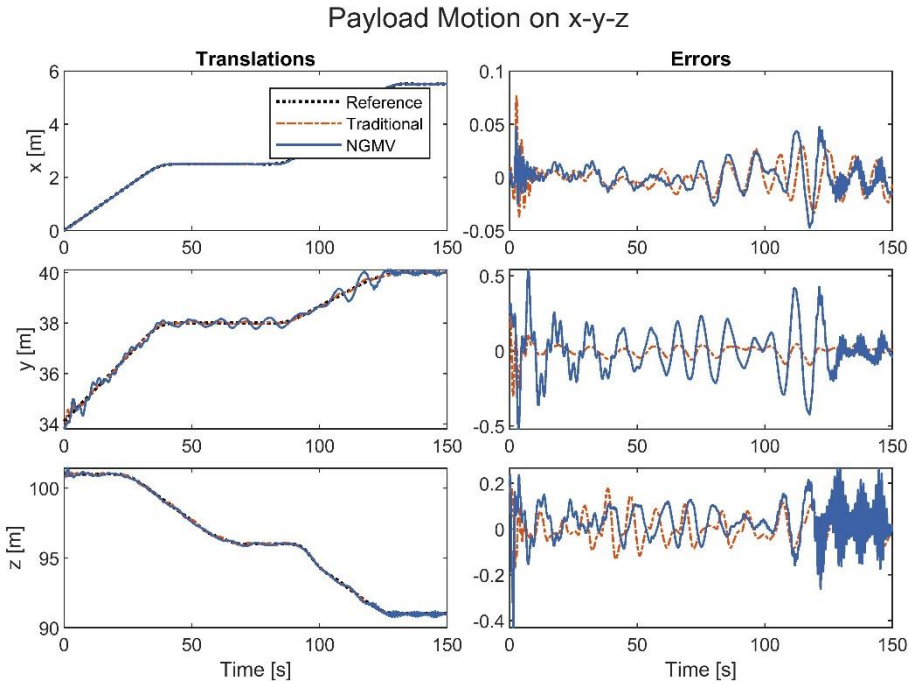

Figure 4.14: Payload positioning on x-y-z and errors to reference trajectory as a result of the errors in joint rotations tracking from Figure 4.13

10% mismatch above the nominal case

The values of hydraulic fluid bulk modulus and piston area were then decreased by 10% while the links and payload masses were increased by 10% to offset the overall response of the transfer function above nominal setting. Running simulations with each controller, their performance can be observed in Figure 4.15 and Figure 4.16.

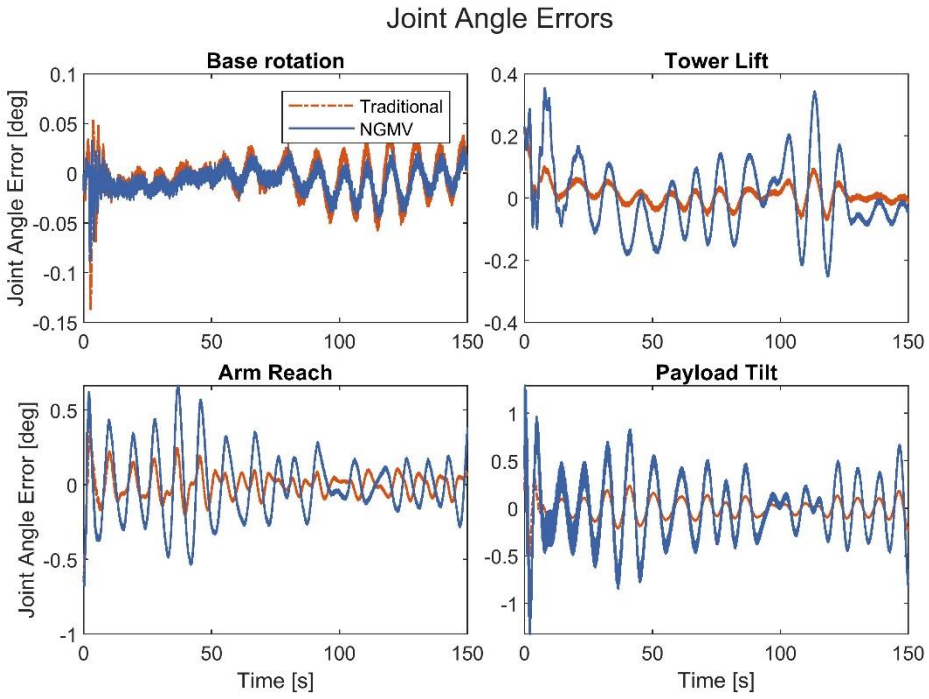

Figure 4.15: Errors in joint rotations reference tracking

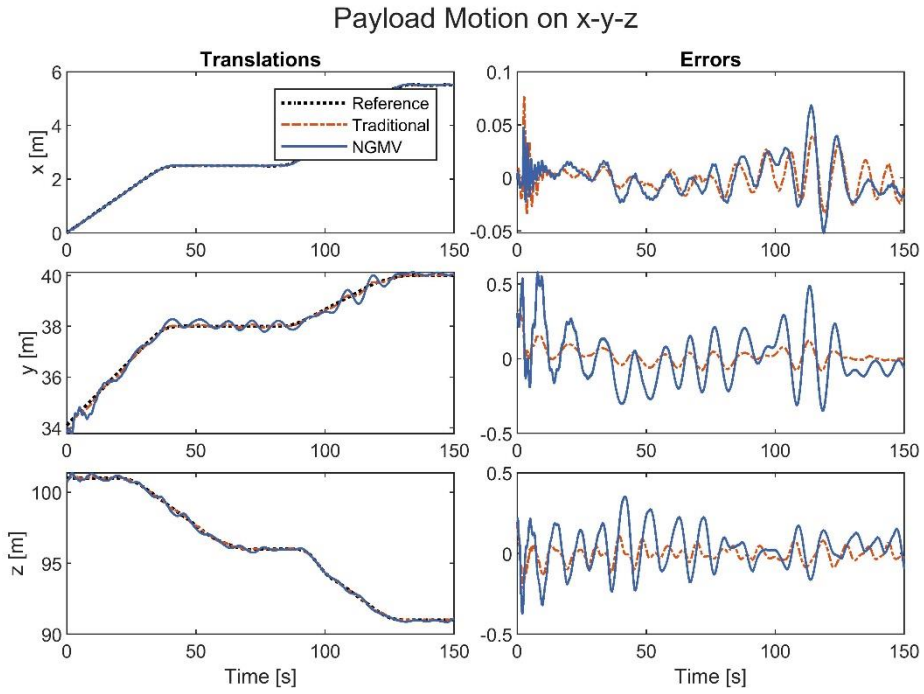

Figure 4.16: Payload positioning on x-y-z and errors to desired trajectory as a result of the errors in joint rotations tracking from Figure 4.15

Summary of results

Performance of both controllers is comparable to their performance in the nominal case, with NGMV being slightly more unstable than traditional control. That can be noticed towards the end of the simulation for the case where system parameters were increased in size, with regards to Figure 4.15 and Figure 4.16. That can be the result of creating a plant with a faster natural frequency which could be more difficult to control by controllers designed for a system with slower natural frequency.

4.3.3. Mismatch Level 20 %

Similarly to Section 4.3.2, the values of hydraulic fluid bulk modulus, cylinder radius, valve area and links and payload masses were modified to create a 20% mismatch above and below the nominal case. Running simulations with each controller, their performance can be observed in Figure 4.17 - Figure 4.20.

20% mismatch below nominal case

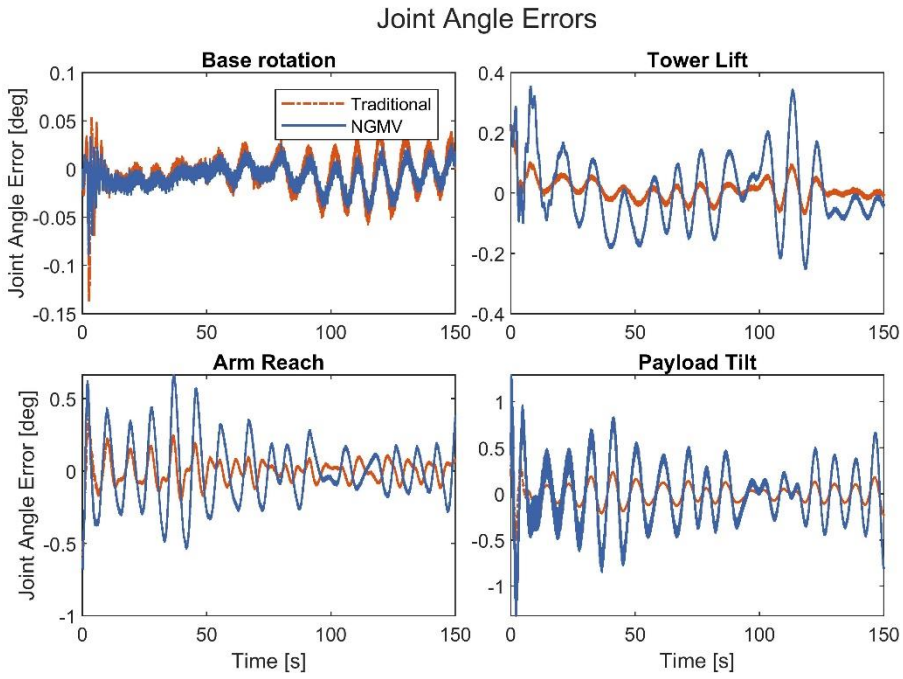

Figure 4.17: Errors in each of the four joint angle rotations tracking

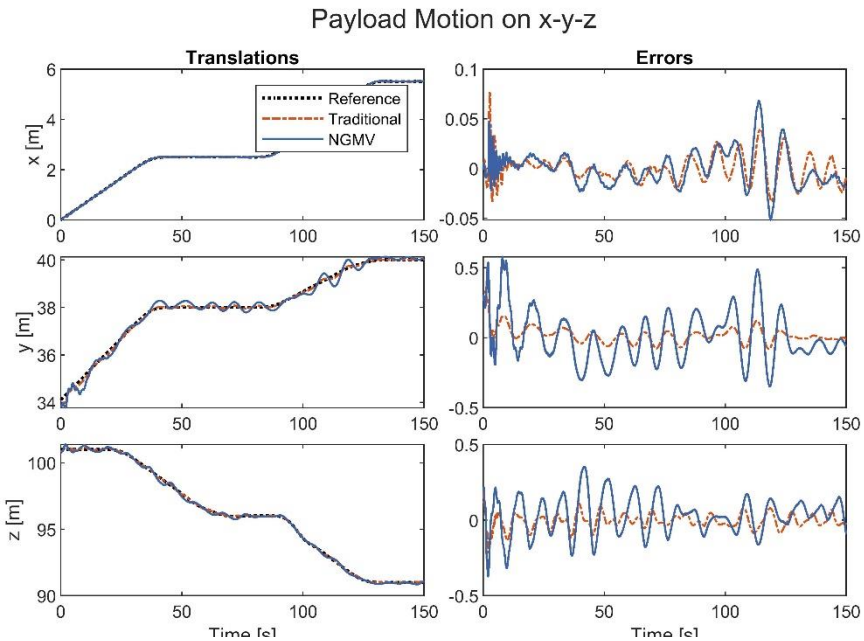

Figure 4.18: Payload positioning on x-y-z and errors to desired trajectory as a result of the errors in joint rotations tracking from Figure 4.17

20% mismatch above nominal case

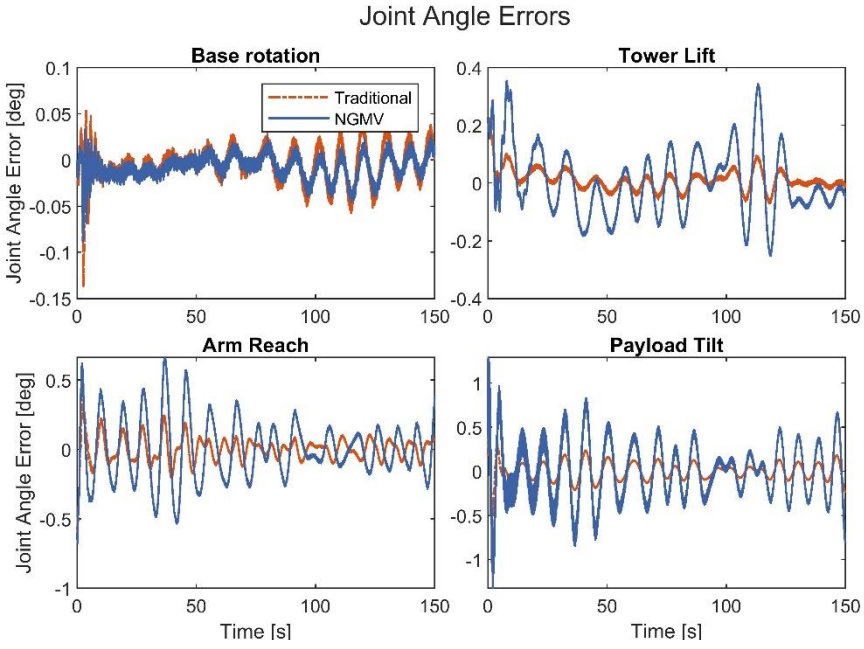

Figure 4.19: Errors in each of the four joint angle rotations tracking

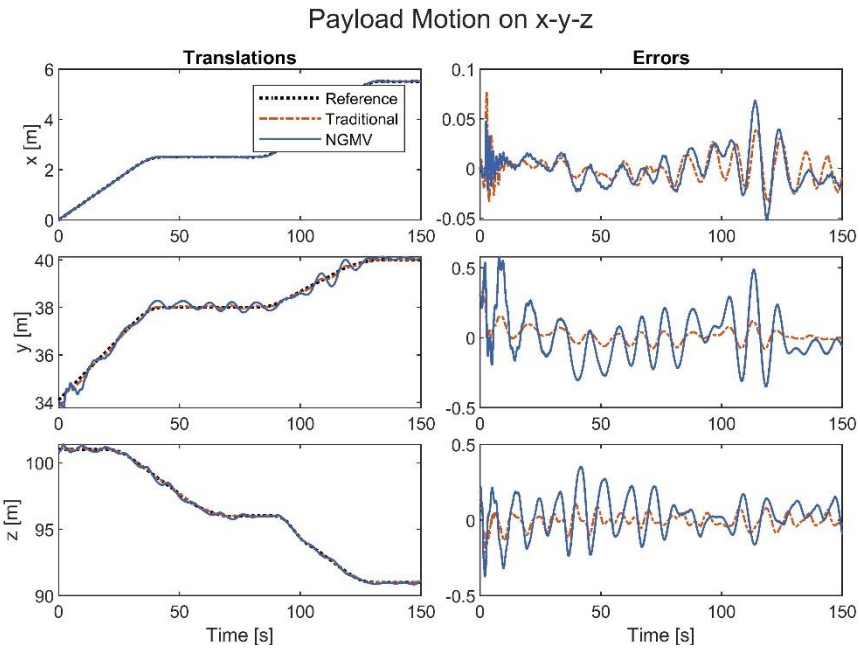

Figure 4.20: Payload positioning on x-y-z and errors to desired trajectory as a result of the errors in joint rotations tracking from Figure 4.19

Summary of results

In this case, $\mathcal{F}_{ck}$ value needed to be increased to stabilize NGMV control action by making it less aggressive when mismatch level was decreased. Similarly, when the system parameters where increased in size, the control weighting $\mathcal{F}_{ck}$ was reduced to produce a more aggressive control to actuate larger overall size of the mismatched crane plant.

4.3.4. Mismatch Level 40%

Finally, the values of hydraulic fluid bulk modulus, cylinder radius, valve area and links and payload masses were adjusted to produce a 40% mismatch above and below the nominal case. Running simulations with each controller in the loop, they produced the following results that can be observed in Figure 4.21 - Figure 4.24.

40% mismatch below nominal case

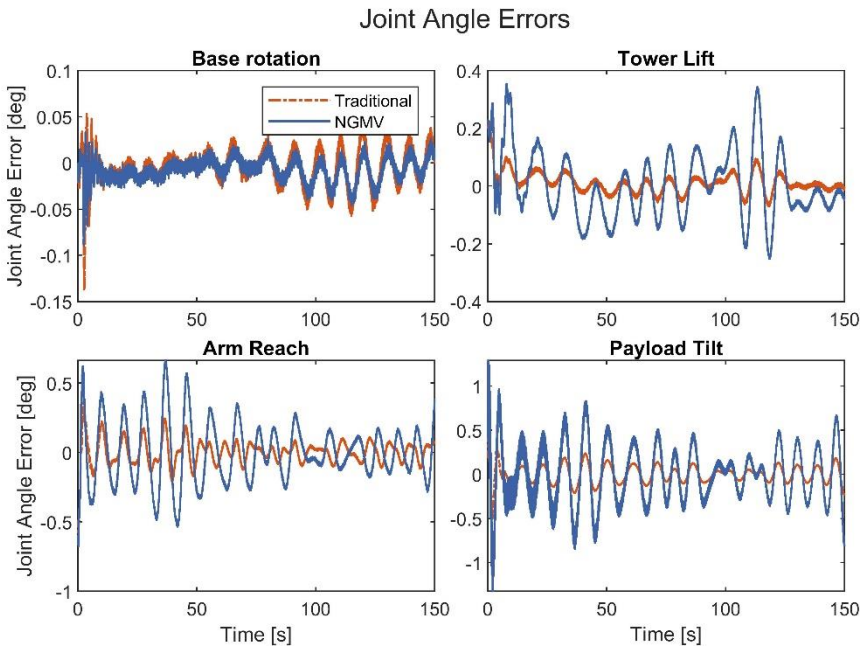

Figure 4.21: Errors in each of the four joint angle rotations tracking

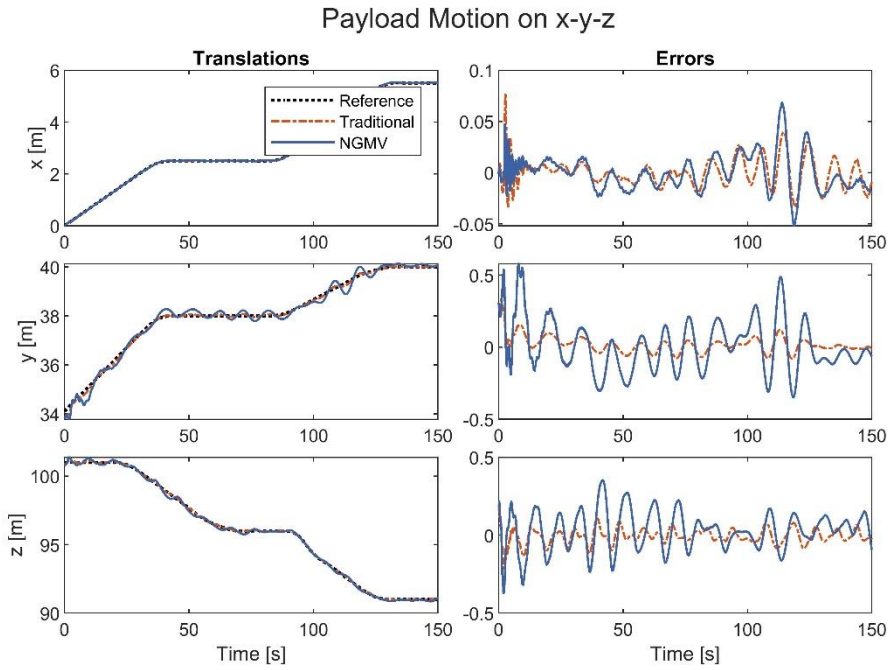

Figure 4.22: Payload positioning on x-y-z and errors to desired trajectory as a result of the errors in joint rotations tracking from Figure 4.21

40% mismatch above nominal case

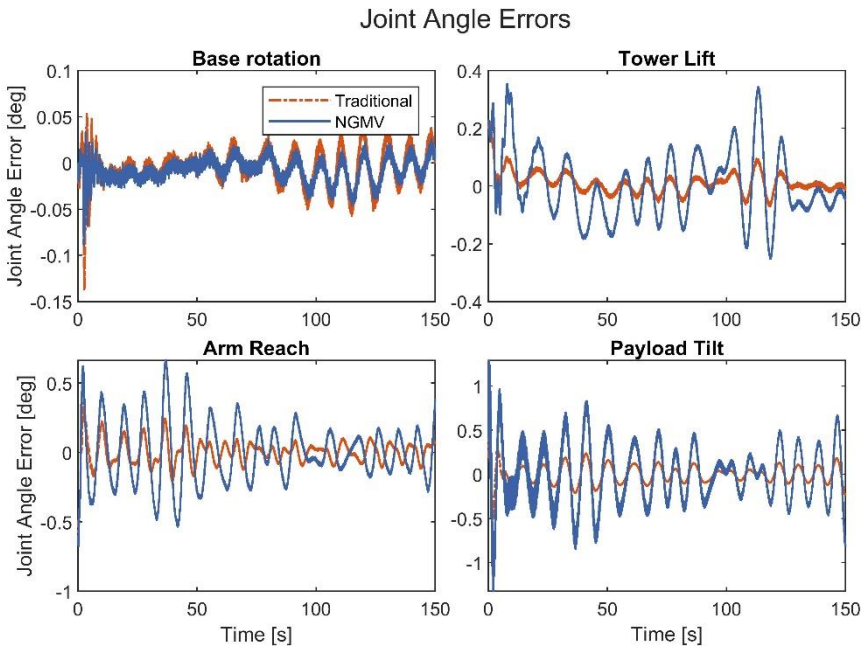

Figure 4.23: Errors in each of the four joint angle rotations tracking

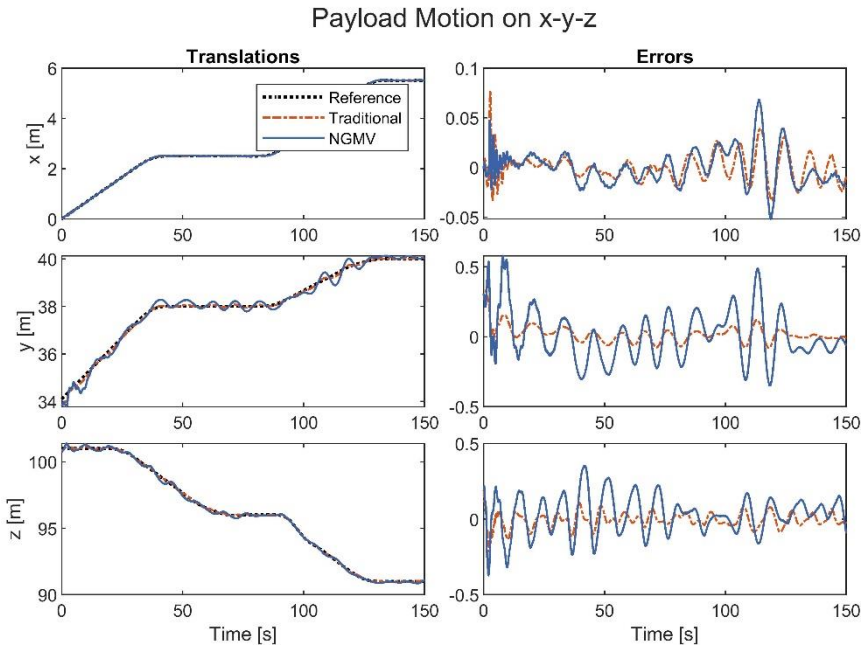

Figure 4.24: Payload positioning on x-y-z and errors to desired trajectory as a result of the errors in joint rotations tracking from Figure 4.23

Summary of results

Figure 4.21 to Figure 4.24 showed that controllers offered a degraded reference tracking when compared to previous cases, which is expectable considering the large percentage mismatch between design and actual plant parameters.

It is worth noting however that each controller performed better for the case when plant size was increased, and outputs were more oscillatory when plant size was reduced. In this case, that can be explained as the nominal hydraulic actuators have a higher natural frequency than that of a crane with an increased mismatch. This could be due to a larger size having lower natural frequency. On the other hand, in the case when mismatch was decreased by 40%, plant's natural frequency was faster than that of the nominal plant. Therefore, controller tuning could compensate better for the situation in which the control design was based on a system with a larger natural frequency than the frequency of the actual system.

4.3.5. Analysing the Results

The observations gathered from the previous experiments in Section 4.3 were put together in Table 4.2 and Table 4.3 as computed root mean square errors (RMSE) between measurements and expectations. The errors in reference tracking for joint rotations and the resulting payload motion on x-y-z axes were thus tabulated.

Table 4.2: Root mean square error for reference tracking of each joint given in degrees across 0%, 10%, 20% and 40% mismatch levels

		Mismatch level						
		0%	10%		20%		40%	
		Nominal	+10%	−10%	+20%	−20%	+40%	−40%
Traditional Control								
Joint	Base Rotation	0.205	0.203	0.203	0.0203	0.203	0.0203	0.0203
	Tower Lift	0.0509	0.0392	0.0293	0.0481	0.0288	0.0837	0.0871
	Arm Reach	0.0303	0.0889	0.1132	0.1116	0.1414	0.0708	0.23
	Payload Tilt	0.0663	0.1003	0.0874	0.11	0.0843	0.1327	0.3645
NGMV Control								
Joint	Base Rotation	0.0151	0.0151	0.0151	0.0151	0.0151	0.0151	0.0151
	Tower Lift	0.0699	0.1196	0.1045	0.1225	0.1187	0.0920	0.1373
	Arm Reach	0.0842	0.0898	0.1173	0.093	0.2292	0.2636	0.8258

	Payload Tilt	0.0982	0.1029	0.1159	0.1006	0.1321	0.3027	0.3068

Table 4.3: Root mean square error for the measured payload trajectory against its reference on x-y-z axes given in meters computed across 0%, 10%, 20% and 40% mismatch levels

		Mismatch level						
		0%	10%		20%		40%	
		Nominal	+10%	−10%	+20%	−20%	+40%	−40%
Traditional Control								
Axis	x	0.0127	0.0138	0.0131	0.0143	0.0127	0.0185	0.0134
	y	0.0826	0.06	0.0431	0.074	0.0434	0.1264	0.1293
	z	0.0305	0.0476	0.0596	0.0596	0.0727	0.0599	0.1348
NGMV Control								
Axis	x	0.0091	0.0163	0.0139	0.0172	0.0157	0.0142	0.0192
	y	0.1071	0.1813	0.1587	0.1852	0.1824	0.1425	0.2106
	z	0.0585	0.0882	0.0859	0.0903	0.1429	0.1388	0.4258

With the RMSE for each individual joint being tabulated in Table 4.2, the values could be plotted for a better visualisation in Figure 4.25 (on the left column). Moreover, Figure 4.25 contains, on the right column, the plotted RMSE of the payload trajectory using the values found in Table 4.3.

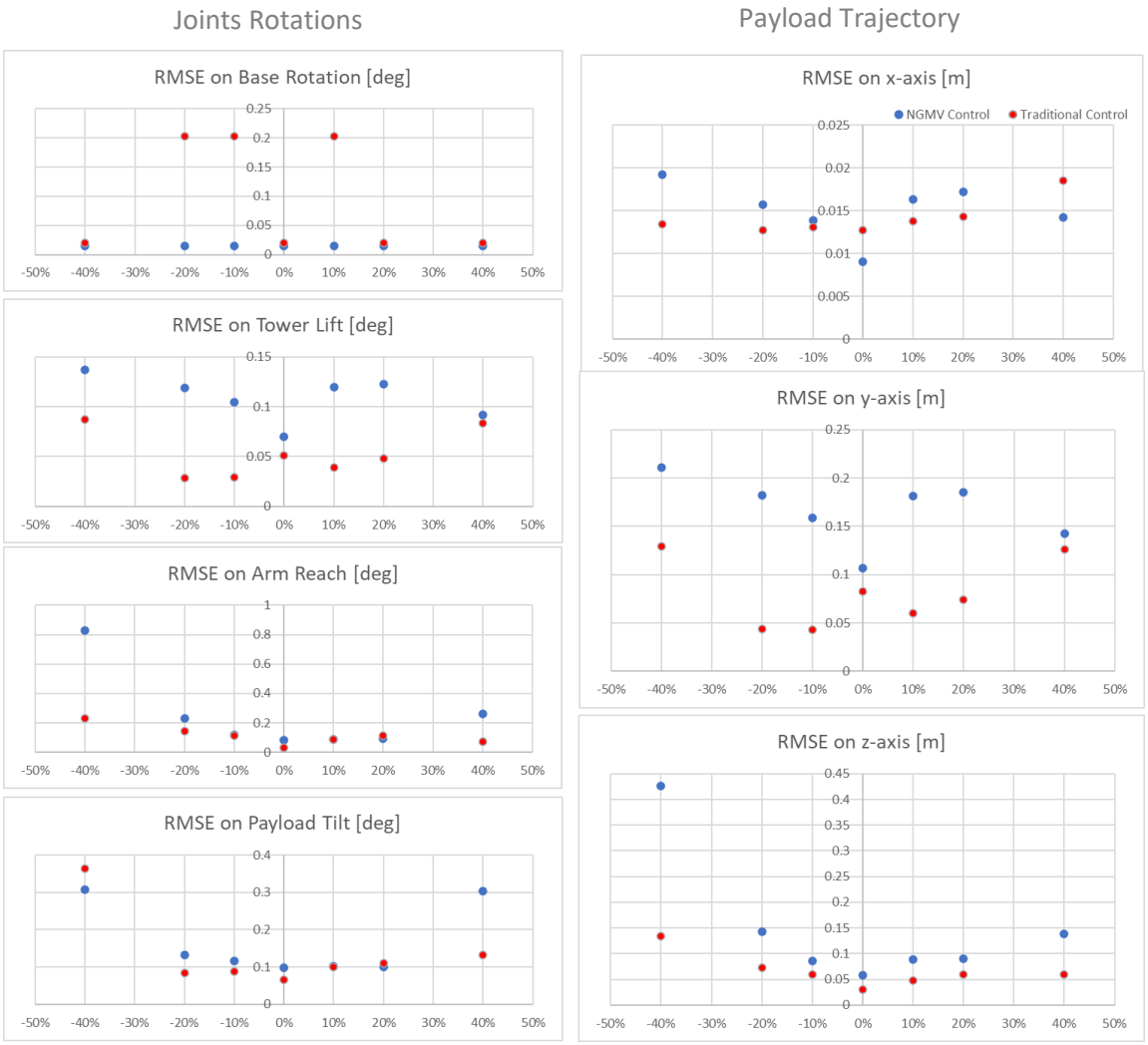

Figure 4.25: Plotted root mean square errors for joints rotations and resulting payload trajectory on x-y-z across 0%, 10%, 20% and 40% mismatch levels

Simulations performed with PIDD and NGMV controllers in the loop produced comparable regulating performance in terms of reference tracking and disturbance rejection, for the nominal case. This confirms the assertion that the PID-based NGMV weightings selection is a useful starting point for controller tuning.

Increasing the mismatch between the nominal system based on which the controllers' architectures are designed and the actual plant shows that the traditional control is more robust for the cases considered. This confirms that, in general, the less complex controllers are often more robust as they are less ambitious in their attempt to optimize performance. More complex schemes, especially model-based, are likely to be more prone to model mismatch, unless such uncertainties are handled by design.

These results are solely representative for the considered design of the crane, hydraulics and controls. If, for instance, a smaller overall crane was designated as the nominal system, the results could be different than the ones presented in this report. Moreover, the results would most likely not be simply scaled down, the reason being the high nonlinearities introduced by the crane dynamics and hydraulics.

4.4. Chapter Summary

This chapter presented the implementation of two control schemes to achieve active motion compensation for the hydraulic winch system modelled in Simulink.

Starting with the traditional control scheme, a feedforward controller was designed based on the inverted transfer function of the hydraulic system. This component was responsible to correct the most part of errors in payload positioning given model mismatch. A feedback PID with double derivative was tuned to account for uncertainties and other small modelling errors.

Then, an advanced control law suitable for highly nonlinear systems such as the crane presented in this work was considered. The choice was the NGMV because it features a model of the plant, and dynamic weightings that affect the controller performance and robustness properties. Also, it includes a Kalman filter to estimate future states of the system. A black-box model term was defined to encapsulate the main nonlinear crane dynamics which did not rely on linearization techniques.

An in-depth comparison between the two control methods was presented. With that regard, the crane system was tasked to balance out a set of given base motions on x-y-z and to achieve a desired 3D payload trajectory. This investigation tested both controllers' robustness against

various levels of mismatch. The goal was to assess which controller is more sensitive to system uncertainty.

Simulations performed with traditional and NGMV controllers in the loop showed that the controllers' performances were comparable for the nominal case. However, traditional control outperformed NGMV for most cases when mismatch was introduced. Increasing the mismatch between the nominal system based on which the controllers' architectures were designed and the actual plant shows that the traditional control was more robust in general.

These results were solely representative for the considered design of the crane, hydraulics and controls. If, for instance, a smaller overall crane was designated as the nominal system, the results could be different from the ones presented in this report. Moreover, that might not be a simple case where the results would be scaled equally to the ratio between system sizes. The reason for that was the high nonlinearities introduced by the crane dynamics and hydraulics.

5. CHAPTER 5: LOAD PLACEMENT MODELLING AND CONTROL

5.1. Introduction

The main objective that was initially set out for this project to accomplish was developing a control architecture that could provide both motion and force control while transferring and placing the payload onto the offshore stand.

The relationship between a servo valve control input (voltage or current) and actuator output force is complex, dynamic, and highly nonlinear. Moreover, hydraulic manipulation involves mechanical contact with the payload to be operated and the environment to be interacted with (Koivumäki and Mattila, 2015). The environment, in this case, refers to a floating vessel deck where the robotic manipulator would be placed. The ship deck was modelled as a moving platform based on the mathematical modelled included within the MSS Toolbox, which was described in Section 2.3.

5.1.1. Contact Force Modelling

Contact force between a pair of rigid bodies is modelled using the penalty method (Rengifo et al., 2010) (Hamad et al., 2017) allowing the bodies to penetrate a small amount to compute the normal and frictional contact forces between the connected objects. These forces are computed using the force equation of the classical spring-damper system and are proportional to intersection depth and velocity. While the depth moves through a transition region, the force smoothly ramps up. At the end of the transition region, the full stiffness and damping are applied. On the rebound, both stiffness and damping forces are smoothly decreased back to zero. This smooth transition eliminates discontinuities from the force equations and eliminates zero-crossing events. The larger the transition region width, the smoother the transition trend of the contact force. In contrast, reducing transition region width to zero, results in a contact force, thus seeming like a discontinuous problem.

The diagram in Figure 5.1 shows the contact frame for the base and follower bodies.

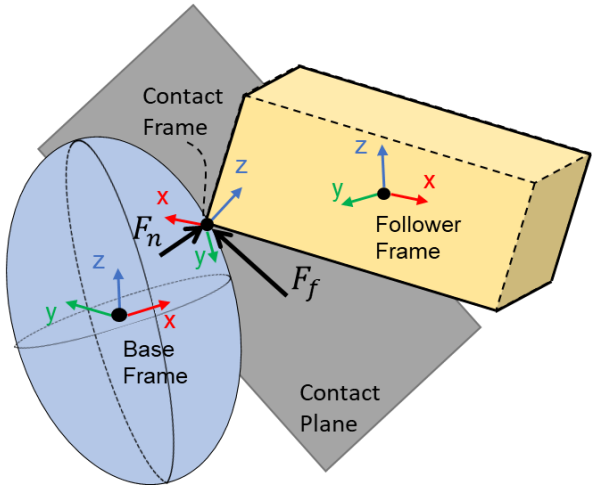

Figure 5.1: Generalised diagram describing the spatial contact force

Contact forces are applied to the two solid masses at the origin of the contact frame according to Newton's Third Law:

1. Normal force, F_n, is aligned with the z-axis of the contact frame and pushes the solid bodies apart in order to reduce contact.

2. Friction force, F_f, lies in the contact plane and opposes the relative tangential velocities between the two bodies near the area of contact. It is perpendicular to the normal force.

Force based methods with penalty formulation model the mechanical contact between two rigid bodies via the linear spring equation. The active normal/friction forces (illustrated in Figure 5.2) perform work on the environment and the physical background of the mechanical contact is not lost.

The mechanical interaction of the bodies caused by the contact is represented by the active normal and friction forces, F_n and F_f, without any additional optimization between the simulation steps.

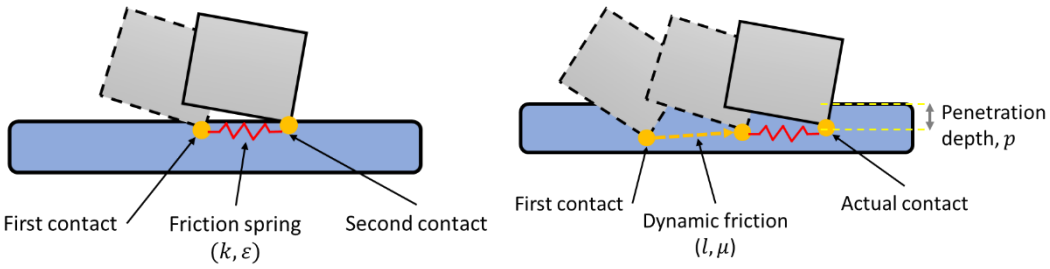

Figure 5.2: Depiction of penalty method for contact and friction forces

The equations employed for determining the normal/friction force magnitudes depend on:

Penetration depth, p

Penetration velocity defined as the rate of change of penetration depth over time, $\dot{p} = dp/dt$

friction penetration, l

effective friction coefficient, μ

Equation (5.1) below describes the magnitude of the normal force in contact and it depends on the stiffness k in the collision area and the damping coefficient ε of the materials:

$$F_n = \begin{cases} k * p + \varepsilon * \dot{p} & p > 0, \dot{p} > 0 \\ k * p & p > 0, \dot{p} < 0 \\ 0 & p \leq 0 \end{cases} \quad (5.1)$$

Note that the normal and tangential directions generally have identical stiffness. The damping coefficient is a constant value representing the lost energy from colliding solid bodies. The larger its value, the more energy is lost when geometries collide and the faster the contact vibrations are dampened. A value of zero indicate perfectly elastic collisions, which conserve energy.

Then, equation (5.2) shows the magnitude of friction (tangential) force in contact:

$$F_f = \mu * F_n \quad (5.2)$$

The coefficient of friction is a function of the relative velocity at the point of contact as given below:

$$\mu = \begin{cases} v_{poc} * \dfrac{\mu_s}{v_{th}}, & v_{poc} < v_{th} \\ \mu_s - v_{poc} * \dfrac{\mu_s - \mu_k}{0.5 * v_{th}}, & v_{th} \leq v_{poc} \leq 1.5 * v_{th} \\ \mu_d, & v_{poc} > v_{th} \end{cases} \tag{5.3}$$

where:

v_{poc}	Velocity at point of contact
v_{th}	Threshold velocity
μ_s	Static friction coefficient
μ_d	Dynamic friction coefficient

The graph in Figure 5.3 shows the relationship between the friction force is affected by the relative velocity.

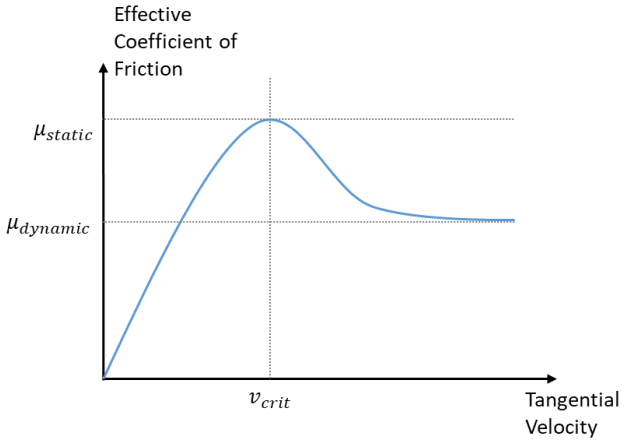

Figure 5.3:Friction coefficient vs the relative tangential velocity near region of contact

The main advantages of the penalty method are its simplicity and robustness as the approach can be implemented on both soft and stiff contacts. Moreover, it can perform reasonably well for the case when multiple contact points are detected simultaneously. However, its drawback is the integrator step size that should be reduced during contact in order to rapidly detect changing contact forces.

Each body has a contact frame with its origin located at the contact point and its *z*-axis aligned with the contact normal direction. Collision normal force is the outward surface normal at the contact point. During continuous contact, the contact frame moves around the body as the contact point moves.

5.1.2. Contact Force Control

Two major types of instability can occur in contact control tasks: dynamic (caused by robot and environment dynamics) and kinematic (caused by kinematic coordinate transformations in control implementations).

One possible solution found in literature is the hybrid force/position control algorithm was followed, which was presented in (Raibert and Craig, 1981). The work showed a conceptual method for controlling both the position of a manipulator and the contact forces generated at the hand of robots, rather than at collisions between rigid objects. Moreover, they explored the use of the hybrid technique in conjunction with data provided by a wrist-mounted force sensor. Therefore, the proposed method did not prescribe feedback control laws for error regulation, it only suggested a control architecture within which such laws could be applied.

5.2. Load Placement

When considering the contact forces during load placement, a platform was modelled to represent the follower frames, while the base frame corresponds to the cylindrical payload.

The sizes of each of the rigid body that are interacting are displayed in Figure 5.4. Figure 5.7 displays the contact forces between the payload and the platform when the crane moves the payload over a specified trajectory.

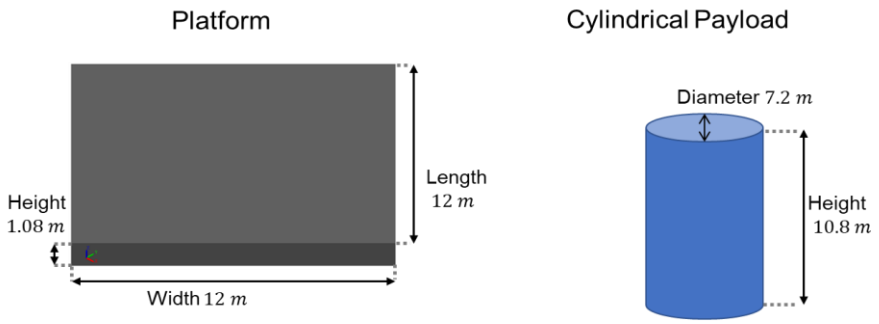

Figure 5.4: Size of the interacting objects (rigid stand and cylindrical load)

Again, it is worth noting from the dimensions of interacting blocks in Figure 5.4 that system sizing is ideal, thus neglecting particular real-life considerations such as the dynamics between the crane system and the vessel.

Initially, a simulation was run to inspect the contact force when the load (decoupled from the crane system) was directly placed on top of the platform. The results are shown in Figure 5.5.

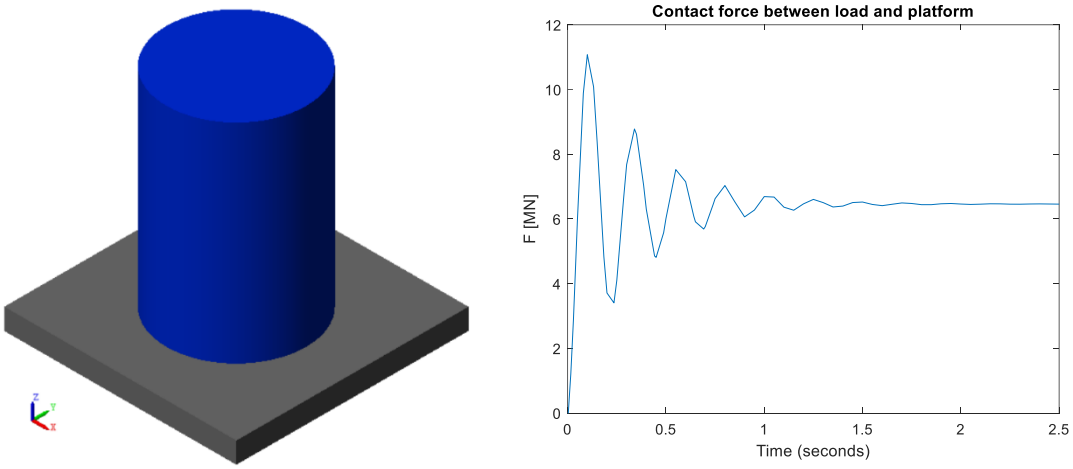

Figure 5.5: Measuring the contact force between the interacting objects being decoupled from the crane

The plot of the contact force between the objects are in agreement with the expectations as indicated by the penalty method. The normal force is damped over time (within the first couple of seconds) and reaches a steady state of $\sim 6.45\ MN$ as the design allows the cylindrical object to penetrate a small depth into the platform.

The parameters used to compute the contact force (in this case the normal force F_n) were defined as:

- Stiffness in the collision area, $k = 5 * 10^8 \frac{N}{m}$
- Damping coefficient, $\varepsilon = 4 * 10^6 \frac{N*s}{m}$

Calculations were compared against simulation results by taking an instant at 2 s where the contact depth was measured to be $p = 12.9251\, mm$ and contact velocity was determined to be $\dot{p} = -0.56 \frac{mm}{s}$. Thus, using eq (5.1), that gives $F_n = 6.46 * 10^6\, N$. Plots showing the relationship between contact depth and velocity and the resulting contact force are presented in Figure 5.6.

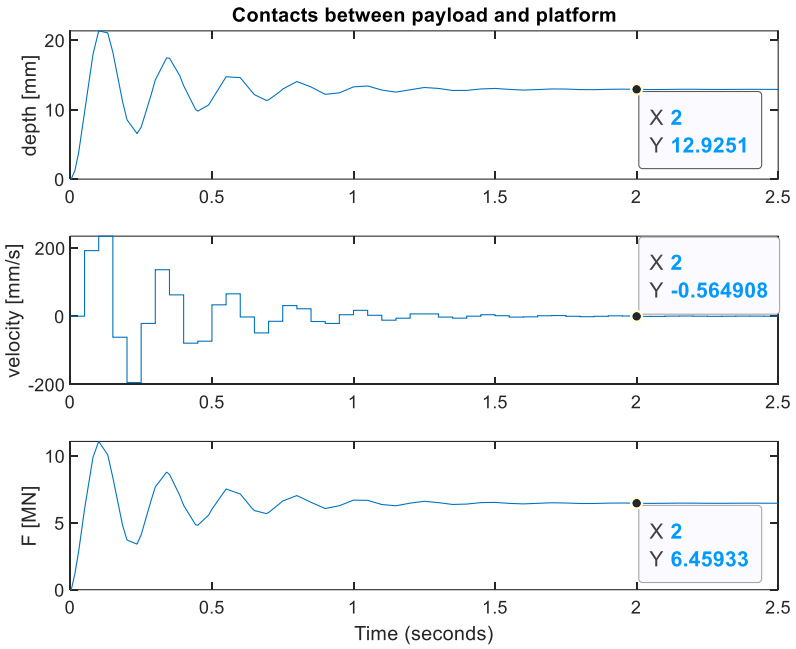

Figure 5.6: Measured contact force between payload and platform given the contact depth and collision velocity.

By analysing the graphs in Figure 5.6, it shows that indeed the simulation results matched the calculations for the contact force between the two bodies given the design parameters provided above.

The open-loop simulation results displayed in Figure 5.7 indicated that modelling of the contact forces while placing a load on the platform was successful. However, the remaining work focused on attempting to control the interaction between the objects in order to reduce the impact forces.

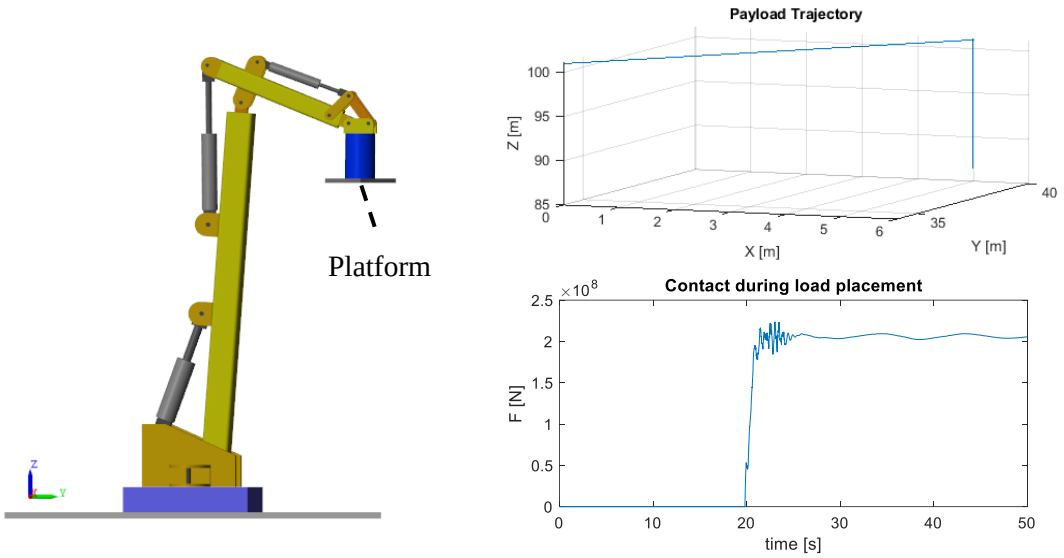

Figure 5.7: Contact force measurement during load placement following a given trajectory and considering active motion compensation

From the preliminary open-loop simulations presented in Figure 5.7, the normal force $F_n \cong 200 * 10^6\ N$, which is due to the position controller tasked to place the payload lower than the platform, thus generating more force than desired. Also, the added effect of the crane pushing down the load results in a higher contact force being sensed when the objects interacted.

The goal would be to have a feedback force controller that would stop the motion on z-axis when the payload comes in contact the platform, while gradually adjusting the contact force until it equals to the weight of the load. The weight is given as:

$$G_{payload} = m_{payload} * g \tag{5.4}$$

with payload mass $m_{payload} = 660\ tons$, therefore $G_{payload} = 6.47 * 10^6$ N

Next section will present the contact force control algorithm that corrects the forces during placement in addition to the positioning algorithm. This will form the hybrid motion/force control architecture.

5.3. Hybrid Motion to Contact Force Control

A switching algorithm between position and force control should be developed to trigger either a motion or a force command going to the actuators. Otherwise, both tasks acting concomitantly would result in robot singularity, meaning a configuration in which the robot end-effector becomes blocked in certain directions.

Payload placement task is automated by using an external hybrid force/position control. The proposed block diagram in Figure 5.8 enables position control on x and y axes, while removing motion on z-axis and applying only force regulation on this vertical axis. The procedure used in the present work for switching between position and force control was detailed in (Rabenorosoa et al., 2010).

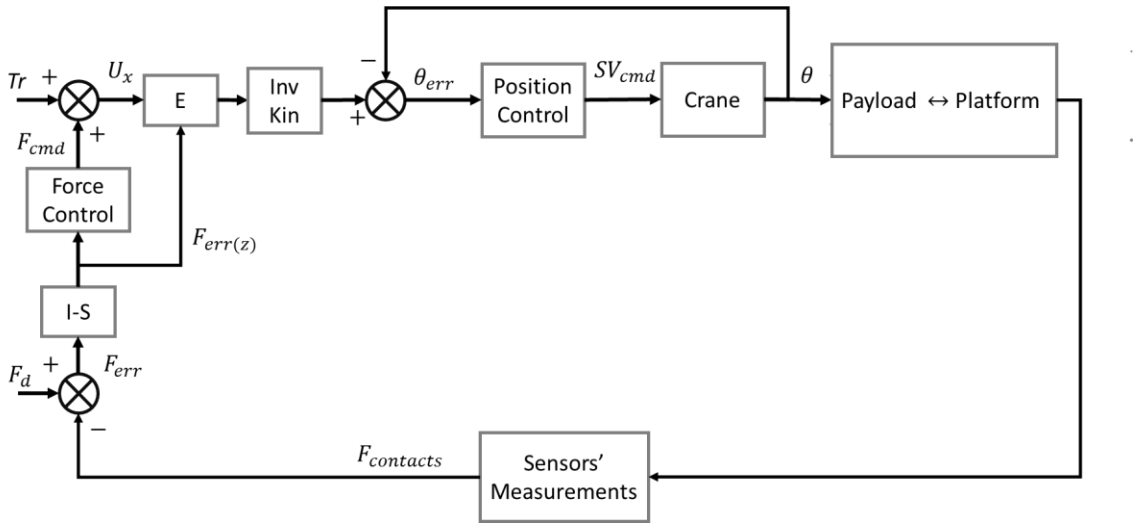

Figure 5.8: Block diagram describing the external hybrid motion to force control during load placement

With respect to Figure 5.8, the reference trajectory of the crane system is denoted by Tr moving on x-y-z, and the reference contact force is $F_d = 0$, meaning no contact is desired, so $F_{err} = -F_{contact}$. The matrix selection $S = \begin{bmatrix} 1 & 0 & 0 \\ 0 & 1 & 0 \\ 0 & 0 & 0 \end{bmatrix}$ enables position control on x and y and removes

motion on z-axis when contact is sensed. Therefore, the block denoted by the difference $I - S = \begin{bmatrix} 0 & 0 & 0 \\ 0 & 0 & 0 \\ 0 & 0 & 1 \end{bmatrix}$, with I the identity matrix.

In order to avoid sliding or rotation during contact, it is required to stop motion along x and y and reduce the contact force under a set limit. The block E is called enable control as it stops motion along x and y if vertical motion is bigger than the desired limit. The architecture of the enable control block is displayed in Figure 5.9.

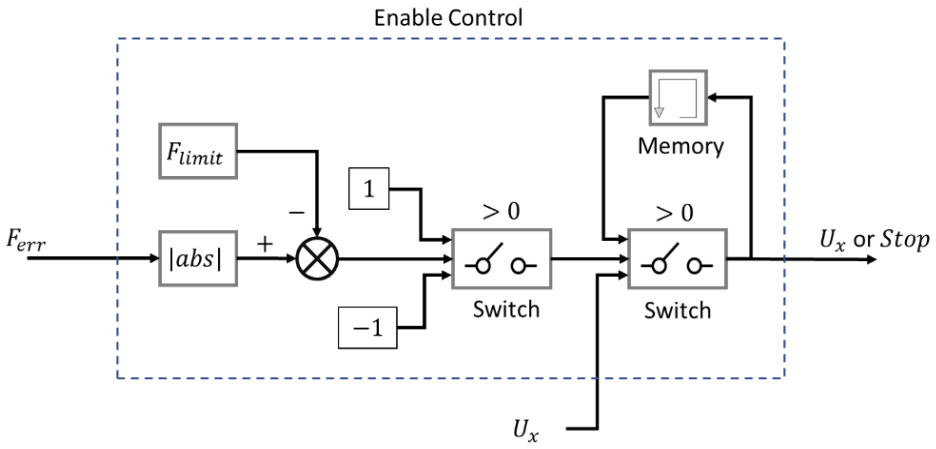

Figure 5.9: Diagram showing the components of the enable control block, E

Enable control E in Figure 5.9 shows that as long as the contact force between the payload and platform is smaller than the set limit, the robot should maneuver the load according to the desired payload trajectory. Otherwise, once that threshold is exceeded, the force control is enabled while maintaining the previous payload position on that given axis, in this case z-axis.

Note that the chosen limit was $F_{limit} = G_{payload} = 6.47 * 10^6$ N.

The use of incremental force control enables easy and fast set up of parameters and reduces risks of damaging the payload or manipulator. It features a dead zone for rejecting sensor noise measurement, a sign operator to indicate the direction of increment, and the memory operation enables the relative positioning. This controller sets the correction in increments through the PID controller. This force control architecture is presented in Figure 5.10.

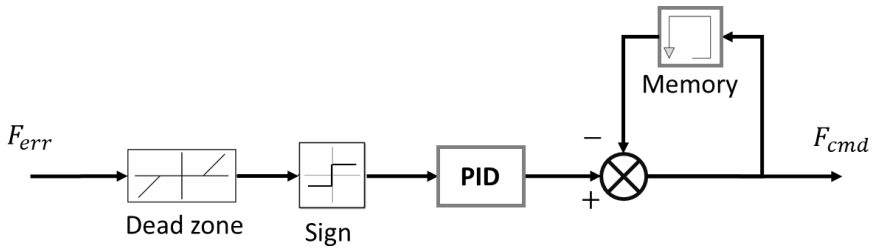

Figure 5.10: Block diagram describing incremental control for contact force task

For position control, the traditional controller architecture developed in the previous Section 4 was employed, with respect to the nominal case where no mismatch was considered.

Simulation of the crane system was performed with the hybrid motion/force controller in the loop, and the results were displayed in Figure 5.11. This proves that the controller was able to reduce the contact forces between the objects and improved overall system stability during load placement.

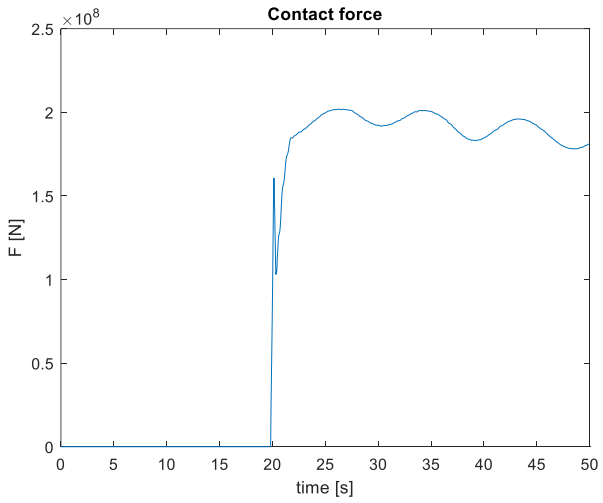

Figure 5.11: Normal force between payload and platform during placement with the hybrid motion/force controller

As it can be seen in Figure 5.11, the contact force does not actually drop down to the expected weight force of the payload mass, i.e. $G_{payload} = 6.47 * 10^6 N$.

One reason for that could be the coupling effect between the crane and the load, which increases the overall sensed contact force. However, compared to the open loop case presented in Figure 5.7, the hybrid motion/force control algorithm reduced contact oscillations. Future work would

look into modelling the decoupling between crane and load to further validate the method presented in this section.

Another reason for the results observed in Figure 5.11 could be due to the implementation of the incremental force control algorithm described in Figure 5.10. As the control scheme being adapted from a research study performed at a micro scale robot (Rabenorosoa et al., 2010), it could not be appropriate for the current task, which is at macroscale. However, more work should be carried out to reach a clearer conclusion that explains the above findings.

5.4. Summary

A hybrid architecture inspired by the work presented in (Rabenorosoa et al., 2010) was implemented for the current crane system. The proposed solution enabled position control on x and y axes, while removing motion and therefore contact on z-axis.

A control enabler determined that if the contact force between the payload and platform was smaller than the set limit, the robot would maneuver the load according to the desired payload trajectory. Otherwise, once that threshold was exceeded, the force control would be triggered motion was stopped for the axis of interest. Incremental force control reduced risks of damaging the payload or the manipulator by correction in increments through a PID controller. Preliminary results of implementing this method showed that the contact force was not minimised to the expected weight force of the payload. One explanation for that could be the added effect of the crane being directly connected to the load pushing down on the platform. At the same time, the incremental force control algorithm might need to be re-evaluated for this case, as it was adapted from the above-mentioned research paper which considered a microscale robot. Therefore, the same logic might not be applied to the present project.

6. CHAPTER 6: DISCUSSION

6.1. Sea State and Vessel Motions Modelling

The sea state selected for the purpose of this work features a 5 m significant wave height H_s and is a superposition of independent random harmonics with maximum wave frequency of 1 rad/s or approximately 6.3 seconds period T_p. The reason behind choosing this set of parameters was to provide a worst-case scenario for the sea state and ensure the crane design can satisfy these requirements. However, in real-life the sea state would be different depending on the location of the wind farm. Thus, it would be impractical to carry out O&M when waves have a significant height of 5 m, and a H_s=1.5 m might be usually the case.

6.2. Hydraulic Crane Design

The hydraulic crane considered in the present work features a 90 m tall hydraulic crane robot holding a 660-ton payload placed on a moving base with 4 degrees of freedom (DoF) that can achieve payload translations along the x, y and z axes, as well as rotation about z-axis. The design choices were arbitrary, as the initial purpose was placing the load (nacelle) on top of the wind turbine tower, therefore the need to model such a tall structure. An important aspect to note is that real-life considerations of implementing this particular crane design were not accounted for. Thus, it might be impractical and impossible to manufacture a crane this size for the considered vessel size, and instead a smaller crane could be used. However, a crane of reduced dimensions would imply re-designing the hydraulics and control architecture. Doing that is not trivial and can prove to be a lengthy process until system stability could be ensured. Thus, such work could be covered in a future project due to time constraints. As a final remark on implementing the system in real-life, scaled prototypes should be built and tested on land and on water to determine whether the control approach is viable. A thorough risk analysis would also be required to establish the insurances, certification and regulations before commercialization. However, development for production of such a system is outside the scope of the present project.

6.3. Motion Control Design

Delving into controller design, it is generally desired to implement a controller that deals with real systems features such as model mismatch, which occurs when the real system is different to the modelled system the controller was designed for.

Looking at the traditional feedforward control and given a desired angle reference, its velocity, acceleration and jerk components (i.e. the first, second and third derivatives) are computed. They are essential to achieve active motion control by removing most of the setpoint and (measurable) disturbance error before it ever gets to the feedback controller. In this way, the feedback controller can be tuned to correct for uncertainties and other small modelling errors. Using the double derivative term in the feedback path, we can adjust the actuators natural frequency and damping thus allowing more control over how fast each piston moves. That would otherwise be dictated by mechanical or hydraulic design only.

However, when it comes to model mismatch, a control law suitable for highly nonlinear systems such as the crane presented in this work was considered. The choice was the NGMV because it features a model of the plant, and dynamic weightings that affect the controller performance and robustness properties. Also, it includes a Kalman filter to estimate future states of the system. A black-box model term can be defined to encapsulate the main nonlinear crane dynamics and therefore does not rely on linearization techniques.

An in-depth comparison between the two control methods was presented. With that regard, the crane system was tasked to balance out a set of given base motions on x-y-z and to achieve a desired 3D payload trajectory. This investigation tested both controllers' robustness against various levels of mismatch. The goal was to assess which controller is more sensitive to system uncertainty.

Simulations performed with traditional and NGMV controllers in the loop showed that the controllers' performances were comparable for the nominal case. However, traditional control outperformed NGMV for most cases when mismatch was introduced. Increasing the mismatch between the nominal system based on which the controllers' architectures were designed and the actual plant shows that the traditional control is more robust in general.

These results are solely representative for the considered design of the crane, hydraulics and controls. If, for instance, a smaller overall crane was designated as the nominal system, the results could be different from the ones presented in this report. Moreover, that might not be a simple case where the results would be a scale of equal to the ratio between system sizes. The reason for that was the high nonlinearities introduced by the crane dynamics and hydraulics.

6.4. Hybrid Motion/Force Control

Having modelled the contact forces between the payload and the offshore platform, a feedback force control algorithm was required to minimise the interaction between the two objects. However, this implementation was not straightforward as it was required to merge it with the positioning controller. Therefore, a hybrid architecture inspired by the work presented in was designed for the current crane system. The proposed solution enabled position control on x and y axes, while removing motion and therefore contact on z-axis.

A control enable determined that if the contact force between the payload and platform was smaller than the set limit, the robot would maneuver the load according to the desired payload trajectory. Otherwise, once that threshold was exceeded, the force control would be triggered motion was stopped for the axis of interest. Incremental force control reduced risks of damaging the payload or the manipulator by correction in increments through a PID controller. Preliminary results of implementing this method showed that the contact force was not minimised to the expected weight force of the payload. One explanation for that could be the added effect of the crane being directly connected to the load pushing down on the platform. At the same time, the incremental force control algorithm might need to be re-evaluated for this case, as it was adapted from the above-mentioned research paper which considered a microscale robot. Therefore, the same logic might not be applied to the present project.

6.5. Summary

This chapter outlined the outcomes and achievements presented in the report. The first section covered the hydraulic crane design requirements which were based on the wave-induced vessel motions for a sea state of 5 m. Then, a 90m tall crane model was developed in Matlab/Simulink (Section 6.2) and controlled via two motion algorithms to achieve active motion compensation on

three-axes (Section 6.3). The comparison between the two showed that the traditional PIDD-feedforward control was marginally more robust than the NGMV controller. Lastly in Section 6.4, the traditional controller was combined with a contact force control algorithm to switch between maneuvering and placing a load onto a fixed platform. Preliminary results did not meet expectations and more work should be carried out to improve the current algorithm.

7. CHAPTER 7: CONCLUSIONS

The offshore wind energy sector faces multiple economical and climate challenges during Operation and Maintenance. A literature survey revealed a strong incentive transitioning towards floating vessels as a substitute of jack up rigs when performing heavy equipment transfers, which depend on multiple degrees-of-freedom, high performance control. This issue is yet to be solved as the most recent study in this sector produced a viable solution only in the case of technicians and equipment transfers (David Salzmann, 2010).

The present research aimed to determine whether such heavy lifts are viable and to develop a control methodology to optimise the process via a simulation based in Simulink. The envisioned scenario consisted of a hydraulic handler located on the deck of the vessel affected by environment wave motions. The crane should maneuver and place the load on an offshore wind turbine platform.

This report presented two control methods to achieve 3D active motion compensation for a hydraulic crane situated on a floating vessel. Given an arbitrary design of the crane, the wave-induced ship motions were determined via the Marine System Simulator toolbox in Simulink. Then, the hydraulics and dynamics of the crane were presented, followed by the design of two controllers. Initially, a traditional control, PIDD and feedforward, was implemented showing an acceptable performance of less than 20 cm error from setpoint at steady state. However, when accounting for model mismatch, a more robust control law was required. Thus, NGMV control was selected in that regard, also due to its ability to compensate for high system nonlinearities and ease of implementation based on tuning the previously determined PID parameters.

The results showed that NGMV control performance degraded in the presence of model mismatch. The traditional controller offered a more consistent performance, being able to reduce motion oscillation while compared with the NGMV architecture. However, a PIDD controller is unlikely to be very practical in the presence of high frequency measurement noise.

An in-depth investigation of controllers' robustness against model mismatch was carried out. Thus, various levels of uncertainty were introduced to the hydraulic fluid bulk modulus and links masses (which influence actuators' natural frequency) to assess system sensitivity. The outcome

of the investigation determined that traditional and NGMV controllers produce comparable regulating performance in terms of reference tracking and disturbance rejection, for the nominal case. This confirmed the assertion that the PID-based NGMV weightings selection is a useful starting point for controller tuning. Increasing the mismatch between the nominal system based on which the controllers' architectures are designed and the actual plant showed that the traditional control was more robust in general.

Contact force modelling was also covered in this report, and the open-loop simulation of the crane system showed a successful implementation. Thus, the interaction between the payload maneuvered by the robot and a platform could be computed. The penalty method was considered to define the normal and friction forces between the two rigid bodies. Then, a control architecture was required to feature a switch between motion to force control. The hybrid motion/force controller showed that indeed contact was minimised on z-axis while lowering the payload onto the stand. This was achieved by removing vertical motion altogether and applying step increments in force through PID control.

As a general conclusion, it is worth re-stating that the present work only considered the modelling and simulation of an ideal prototype in the given scenario of offshore wind maintenance. There were many overlooked aspects, which include the realistic sizing of the robot and how it would fit and on a real ship and any dynamics between the two. To clarify, that would mean the forces the winch mechanism would act upon the floating vessel and vice versa while moving a mass in three-dimensional space. Such considerations were deemed outside the scope of the project as designing from scratch a functional prototype and then implementing the control algorithms were the focus of the research. Thus, the goal of this project was to provide proof-of-concept without the need to consider its real-life implementation. Of course, the simulation stages of the model could be further developed. There is still work to be done to resize the Simulink model and then to improve the control algorithms for motion compensation and contact force control. However, this project aimed to provide a good starting basis for future work that could potentially lead to a more complex model.

Then moving on to implementing such system in real-life, scaled prototypes, which usually are five times smaller, should be first built. Prototype tests should be carried out on land and water (such as an indoor pool) to validate the integrity of the control approach. Based on the industrial

partners' expertise, the costs for such experiments could be too high for PhD research and would involve a larger scale project. A thorough risk analysis would also be required to establish the insurances, certification and regulations before commercialization. Therefore, development for production of such a system was beyond the scope of the present project.

REFERENCES

Advani, S.K., 1998. The Kinematic design of flight simulator motion bases. TU Delft.

Anders Lohmann Madsen, Søren Giessing Kristensen, 2012. Design of Stewart Platform for Wave Compensation (Masters Thesis). Aalborg University.

Andersen, T.O., 2003. Fluid Power Systems - Modelling and Analysis, 2nd ed. Aalborg University.

Angeles, J., 2014. Dynamics of Serial Robotic Manipulators, in: Angeles, J. (Ed.), Fundamentals of Robotic Mechanical Systems: Theory, Methods, and Algorithms, Mechanical Engineering Series. Springer International Publishing, Cham, pp. 281–351. https://doi.org/10.1007/978-3-319-01851-5_7

Balchen, J.G., Jenssen, N.A., Mathisen, E., Saelid, S., 1980. Dynamic positioning of floating vessles based on Kalman filtering and optimal control, in: 1980 19th IEEE Conference on Decision and Control Including the Symposium on Adaptive Processes. pp. 852–864. https://doi.org/10.1109/CDC.1980.271924

Baldock, N., Sevilla, F., Redfern, R., Storey, A., Kempenaar, A., Elkinton, C., 2014. Optimization of Installation, Operation and Maintenance at Offshore Wind Projects in the U.S.: Review and Modeling of Existing and Emerging Approaches (No. 701216- UKBR- R- 01- F). Garrad Hassan America, Inc., San Diego, CA (United States). https://doi.org/10.2172/1333103

Brudniok, S., Maischberge, J., Schreiber, G., 2009. Linear-motion telescopic mechanism and robot arm having linear-motion telescopic mechanism. DK2508308T3.

Camacho, E.F., Bordons, C., 2007. Nonlinear Model Predictive Control: An Introductory Review, in: Findeisen, R., Allgöwer, F., Biegler, L.T. (Eds.), Assessment and Future Directions of Nonlinear Model Predictive Control, Lecture Notes in

Control and Information Sciences. Springer, Berlin, Heidelberg, pp. 1–16. https://doi.org/10.1007/978-3-540-72699-9_1

Christoph Kost, Shivenes Shammugam, Verena Jülch, Thomas Schlegl, Huyen-Tran Nguyen, 2018. Levelized Cost of Electricity - Renewable Energy Technologies.

David Salzmann, 2010. Ampelmann, Development of the Access System for Offshore Wind Turbines (PhD Thesis). TU Delft.

De Zeeuw, W.A., 2012. Ship Motion Compensation Platform for High Payloads Dynamic Analysis and Control (Master of Science Thesis). Delft University of Technology.

Findeisen, R., Allgöwer, F., 2002. An Introduction to Nonlinear Model Predictive Control.

Goda, Y., 2018. A Comparative Review on the Functional Forms of Directional Wave Spectrum. Coast. Eng. J. https://doi.org/10.1142/S0578563499000024

Goodwin, G.C., Rojas, O., Takata, H., 2001. Nonlinear Control VIA Generalized Feedback Linearization Using Neural Networks. Asian J. Control 3, 79–88. https://doi.org/10.1111/j.1934-6093.2001.tb00047.x

Grimble, M.J., 2006. Design of generalized minimum variance controllers for nonlinear multivariable systems. Int. J. Control Autom. Syst. 4, 281–292.

Grimble, M.J., Majecki, P., 2020. Nonlinear Industrial Control Systems: Optimal Polynomial Systems and State-Space Approach. Springer-Verlag, London. https://doi.org/10.1007/978-1-4471-7457-8

Grimble, M.J., Majecki, P., 2015. Non-linear predictive generalised minimum variance state-dependent control. IET Control Theory Appl. 9, 2438–2450. https://doi.org/10.1049/iet-cta.2015.0356

Grimble, M.J., Patton, R.J., Wise, D.A., 1980. The design of dynamic ship positioning control systems using stochastic optimal control theory. Optim. Control Appl. Methods 1, 167–202. https://doi.org/10.1002/oca.4660010207

Hamad, F., Giridharan, S., Moormann, C., 2017. A Penalty Function Method for Modelling Frictional Contact in MPM. Procedia Eng., Proceedings of the 1st International Conference on the Material Point Method (MPM 2017) 175, 116–123. https://doi.org/10.1016/j.proeng.2017.01.038

Heinrichs, B., Sepehri, N., Thornton-Trump, A.B., 1996. Position-based impedance control of an industrial hydraulic manipulator, in: Proceedings of IEEE International Conference on Robotics and Automation. pp. 284–290 vol.1. https://doi.org/10.1109/ROBOT.1996.503791

Heybroek, K., Sjöberg, J., 2018. Model Predictive Control of a Hydraulic Multichamber Actuator: A Feasibility Study. IEEEASME Trans. Mechatron. 23, 1393–1403. https://doi.org/10.1109/TMECH.2018.2823695

Holthuijsen, L.H., 2007. Waves in Oceanic and Coastal Waters. Cambridge University Press. https://doi.org/10.1017/CBO9780511618536

Hovland, V., Vatn, A., 2006. Helicopter landing platform having motion stabilizer for compensating ship roll and/or pitch. US20100224118A1.

Isidori, A., 1995. Nonlinear Control Systems, 3rd ed. Springer London.

Journée, J.M.J., Massie, W.W., 2000. Offshore Hydromechanics, 3rd ed. TU Delft, 2000.

Koivumäki, J., Mattila, J., 2015. Stability-Guaranteed Force-Sensorless Contact Force/Motion Control of Heavy-Duty Hydraulic Manipulators. IEEE Trans. Robot. 31, 918–935. https://doi.org/10.1109/TRO.2015.2441492

Koppert, P.M., 2009. Motion compensation device for compensating a carrier frame on a vessel for water motion. EP2414218B1.

Küchler, S., Sawodny, O., 2010. Nonlinear control of an active heave compensation system with time-delay, in: 2010 IEEE International Conference on Control Applications. pp. 1313–1318. https://doi.org/10.1109/CCA.2010.5611119

Kucuk, S., Bingul, Z., 2006. Robot Kinematics: Forward and Inverse Kinematics. Ind. Robot. Theory Model. Control. https://doi.org/10.5772/5015

Lee, W., Chung, W.K., 2017. Position-based PD control design for hydraulic robots using passive subsystems in multi-time scales, in: 2017 IEEE International Conference on Robotics and Automation (ICRA). pp. 71–78. https://doi.org/10.1109/ICRA.2017.7988693

Leira, B.J., Sørensen, A.J., Larsen, C.M., 2004. A reliability-based control algorithm for dynamic positioning of floating vessels. Struct. Saf. 26, 1–28. https://doi.org/10.1016/S0167-4730(03)00018-3

Lipkin, H., 2008. A Note on Denavit-Hartenberg Notation in Robotics. American Society of Mechanical Engineers Digital Collection, pp. 921–926. https://doi.org/10.1115/DETC2005-85460

Maciejowski, J.M., 2002. Predictive control: with constraints. Prentice Hall, Harlow, England; New York.

Mokhatab, S., Poe, W.A., 2012. Chapter 14 - Process Control Fundamentals, in: Mokhatab, S., Poe, W.A. (Eds.), Handbook of Natural Gas Transmission and Processing (Second Edition). Gulf Professional Publishing, Boston, pp. 473–509. https://doi.org/10.1016/B978-0-12-386914-2.00014-5

Peng, X., Yuan, J., Zhang, W., Yang, Y., Song, Y., 2012. Kinematic and dynamic analysis of a serial-link robot for inspection process in EAST vacuum vessel. Fusion Eng. Des., Tenth International Symposium on Fusion Nuclear Technology (ISFNT-10) 87, 905–909. https://doi.org/10.1016/j.fusengdes.2012.02.041

Perez, T., Smogeli, O., Fossen, T., Sorensen, A.J., 2006a. An overview of the Marine Systems Simulator (MSS): A Simulink Toolbox for Marine Control Systems. Model. Identif. Control 27, 259–275.

Perez, T., Smogeli, O., Fossen, T., Sorensen, A.J., 2006b. An overview of the Marine Systems Simulator (MSS): A Simulink Toolbox for Marine Control Systems. Model. Identif. Control 27, 259–275.

Poh, A.K., Tang, C.H., Kang, H., Lee, K., Siow, C., Malik, A.M.A., Mailah, M., 2017. Gyroscopic stabilisation of rolling motion in simplified marine hull model, in: 2017 IEEE 7th International Conference on Underwater System Technology: Theory and Applications (USYS). pp. 1–6. https://doi.org/10.1109/USYS.2017.8309458

Powell, T.E., 1995. Motion compensated apparatus. US5822813A.

Raadal, H.L., Vold, B.I., Myhr, A., Nygaard, T.A., 2014. GHG emissions and energy performance of offshore wind power. Renew. Energy 66, 314–324. https://doi.org/10.1016/j.renene.2013.11.075

Rabenorosoa, K., Clévy, C., Lutz, P., 2010. Hybrid force/position control applied to automated guiding tasks at the microscale, in: 2010 IEEE/RSJ International Conference on Intelligent Robots and Systems. Presented at the 2010 IEEE/RSJ International Conference on Intelligent Robots and Systems, pp. 4366–4371. https://doi.org/10.1109/IROS.2010.5649216

Rademakers, L., 2003. Assessment and Optimisation of Operation and Maintenance of Offshore Wind Turbines.

Rademakers, L., Braam, H., Obdam, T., 2007. Estimating costs of operation & maintenance for offshore wind farms.

Raibert, M.H., Craig, J.J., 1981. Hybrid Position/Force Control of Manipulators. J. Dyn. Syst. Meas. Control 103, 126–133. https://doi.org/10.1115/1.3139652

Reimers, B., Özdirik, B., Kaltschmitt, M., 2014. Greenhouse gas emissions from electricity generated by offshore wind farms. Renew. Energy 72, 428–438. https://doi.org/10.1016/j.renene.2014.07.023

Renewable Energy Statistics [WWW Document], 2019. . Publ.-Energy-Stat.-2019. URL https://www.irena.org/publications/2019/Jul/Renewable-energy-statistics-2019 (accessed 4.11.22).

Renewable Power Generation Costs in 2012 An Overview [WWW Document], 2013. URL https://www.irena.org/publications/2013/Jan/Renewable-Power-Generation-Costs-in-2012-An-Overview (accessed 4.30.23).

Rengifo, C., Aoustin, Y., Christine, C., Plestan, F., 2010. A penalty-based approach for contact forces computation in bipedal robots. Presented at the 9th IEEE-RAS International Conference on Humanoid Robots, HUMANOIDS09, pp. 121–127. https://doi.org/10.1109/ICHR.2009.5379590

Richter, M., Schaut, S., Walser, D., Schneider, K., Sawodny, O., 2017. Experimental validation of an active heave compensation system: Estimation, prediction and control. Control Eng. Pract. 66, 1–12. https://doi.org/10.1016/j.conengprac.2017.06.005

Röckmann, C., Lagerveld, S., Stavenuiter, J., 2017. Operation and Maintenance Costs of Offshore Wind Farms and Potential Multi-use Platforms in the Dutch North Sea, in: Buck, B.H., Langan, R. (Eds.), Aquaculture Perspective of Multi-Use Sites in the Open Ocean: The Untapped Potential for Marine Resources in the Anthropocene. Springer International Publishing, Cham, pp. 97–113. https://doi.org/10.1007/978-3-319-51159-7_4

Sandino, L.A., Bejar, M., Ollero, A., 2011. On the applicability of linear control techniques for autonomous landing of helicopters on the deck of a ship, in: 2011 IEEE International Conference on Mechatronics. pp. 363–368. https://doi.org/10.1109/ICMECH.2011.5971312

Schmidt, O., Melchior, S., Hawkes, A., Staffell, I., 2019. Projecting the Future Levelized Cost of Electricity Storage Technologies. Joule 3, 81–100. https://doi.org/10.1016/j.joule.2018.12.008

Shi, B., Xian, L., Wu, Q., Zhang, Y., 2014. Active heave compensation prediction research for deep sea homework crane based on KPSO - SVR, in: Proceedings of the 33rd Chinese Control Conference. Presented at the Proceedings of the 33rd Chinese Control Conference, pp. 7637–7642. https://doi.org/10.1109/ChiCC.2014.6896273

Stewart Platform - MATLAB & Simulink - MathWorks [WWW Document], n.d.

Sugihara, T., 2009. Solvability-unconcerned inverse kinematics based on Levenberg-Marquardt method with robust damping, in: 2009 9th IEEE-RAS International Conference on Humanoid Robots. pp. 555–560. https://doi.org/10.1109/ICHR.2009.5379515

Šulc, B., Jan, J.A., 2002. Non Linear Modelling and Control of Hydraulic Actuators. Acta Polytech. 42. https://doi.org/10.14311/354

Tafazoli, S., Salcudean, S.E., Hashtrudi-Zaad, K., Lawrence, P.D., 2002. Impedance control of a teleoperated excavator. IEEE Trans. Control Syst. Technol. 10, 355–367. https://doi.org/10.1109/87.998021

Thomson, C., Harrison, G., 2015. Life cycle costs and carbon emissions of wind power: Executive Summary.

U.S. Energy Information Administration, 2020. Annual Energy Outlook 2020.

van Bussel, G., Bierbooms, W., 2003. The DOWEC Offshore Reference Windfarm: Analysis of Transportation for Operation and Maintenance. Wind Eng. 27. https://doi.org/10.1260/030952403322770986

Votrubec, R., 2014. Stabilization of Platform Using Gyroscope. Procedia Eng., 24th DAAAM International Symposium on Intelligent Manufacturing and Automation, 2013 69, 410–414. https://doi.org/10.1016/j.proeng.2014.03.006

Wilkie, J., Johnson, M., Katebi, R., 2002. Control Engineering: An Introductory Course. PALGRAVE Houndmills, United Kingdom.

Wind energy in Europe in 2018, WindEurope.

Woodacre, J.K., Bauer, R.J., Irani, R.A., 2015. A review of vertical motion heave compensation systems. Ocean Eng. 104, 140–154. https://doi.org/10.1016/j.oceaneng.2015.05.004

Ying, J., 2013. Helicopter landing pad. US9296492B2.

Young, I.R. (Ed.), 1999. Chapter 5 - Fetch and Duration Limited Growth, in: Elsevier Ocean Engineering Series, Wind Generated Ocean Waves. Elsevier, pp. 83–131. https://doi.org/10.1016/S1571-9952(99)80007-5

APPENDIX

Experimental procedure for a hydraulic cylinder design and traditional control

1. Preliminary design of the double acting hydraulic cylinder

2. Perform the open loop test to extract natural frequency and damping of the hydraulic cylinder from the velocity plot:

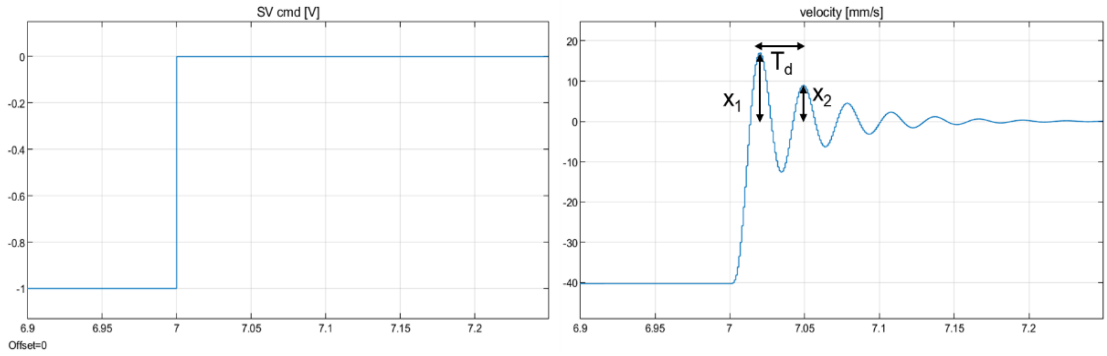

Hydraulic cylinder piston velocity from servo valve input voltage.

The natural frequency is given as:

$$\omega_n = 2\pi f_n = 2\pi \frac{f_d}{\sqrt{1-\zeta^2}} = 2\pi \frac{1}{T_d\sqrt{1-\zeta^2}}$$

and the damping is

$$\zeta = \frac{\delta}{\sqrt{\pi^2 + \delta^2}}$$

where

$$\delta = \ln \frac{x_1}{x_2}$$

Systems with high natural frequency f_n are easier to control and as a rule of thumb it should be at least 4 times the required frequency of acceleration. f_n can be increased through adjusting the following:

$$\omega_n = \sqrt{\frac{4\beta A^2}{VM}}$$

Parameters that affect the natural frequency of a hydraulic cylinder.

Symbol	Name	Action to increase natural frequency
β	Fluid bulk modulus	Choose quality clean oil
A	Cylinder surface area	Large cylinders → larger and slower valves
V	Hose volumes	Minimise
M	Payload Mass	Reduce

3. Validate the correct design of the hydraulic actuator. An example of such test is displayed below, where the lift actuator of the crane was investigated.

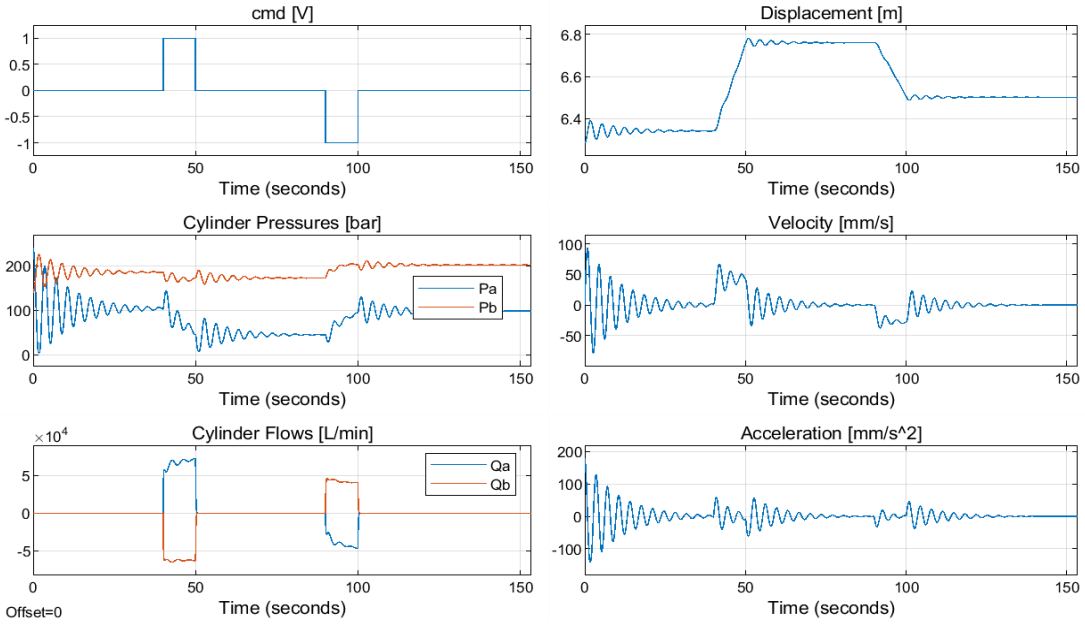

Open-loop test of a hydraulic cylinder actuator in a crane design

An important thing to note in the design is the cylinder pressures, which need to be within the interval (0, P_s). In this case, the supply pressure was set as $P_s = 300\ bar$, and therefore the design was validated from this point of view.

Monitoring the pressures gives an idea of the forces as:

$$F_{cyl} = P_a S_a - P_b S_b$$

where:

F_{cyl}	Force acting on the cylinder to extend/retract
P_a	Chamber A pressure
P_b	Chamber B pressure
S_a	Chamber A area
S_b	Chamber B area

F_{cyl} needs to overcome or act in the direction of the static load F_{load} (due to gravity), depending which way the load should move. In general, the force acting on the piston is:

$$F_{pist} = F_{cyl} - F_{load}$$

and this then determines the acceleration, velocity, and position, with the effective inertia and force varying with the pose. Too small F_{cyl} creates cavitation in the cylinder (check if either P_a or P_b go down to zero, and the other to supply pressure Ps) and the system is not controllable but just 'falls' due to gravity.

Solution: increase cylinder size (S_a and S_b), supply pressure P_s, or simply reduce the mass of the machine (which will reduce F_{load})

4. Approximate the hydraulic cylinder with a second order transfer function:

$$H_{hcyl}(s) = \frac{displacement}{V_{in}} = \frac{K * \omega_n^2}{s * (s^2 + 2\zeta w_n s + \omega_n^2)}$$

5. Extract the ideal feedforward control gains from the inverted transfer function of the hydraulic cylinder:

The servo valve input voltage can be expressed in terms of output piston displacement as follows:

$$u_{FF} = G^{-1}(s)y_r = \frac{s(s^2 + 2\zeta\omega_n s + \omega_n^2)}{K\omega_n^2} y_r =$$

$$= \frac{1}{K} s y_r + \frac{2\zeta}{K\omega_n} s^2 y_r + \frac{1}{K w_n^2} s^3 y_r$$

where

$K_v = \frac{1}{K} y_r$ feedforward velocity

$K_a = \frac{2\zeta}{K\omega_n} y_r$ feedforward acceleration

$K_j = \frac{1}{K w_n^2} y_r$ feedforward jerk

and K is the feedforward steady-state (ss) slope gain and it is the ratio of the ss velocity over ss input voltage:

$$K = \frac{V_{ss}}{U_{ss}}$$

therefore

$$u_{FF} = \frac{1}{K} v_{ref}$$

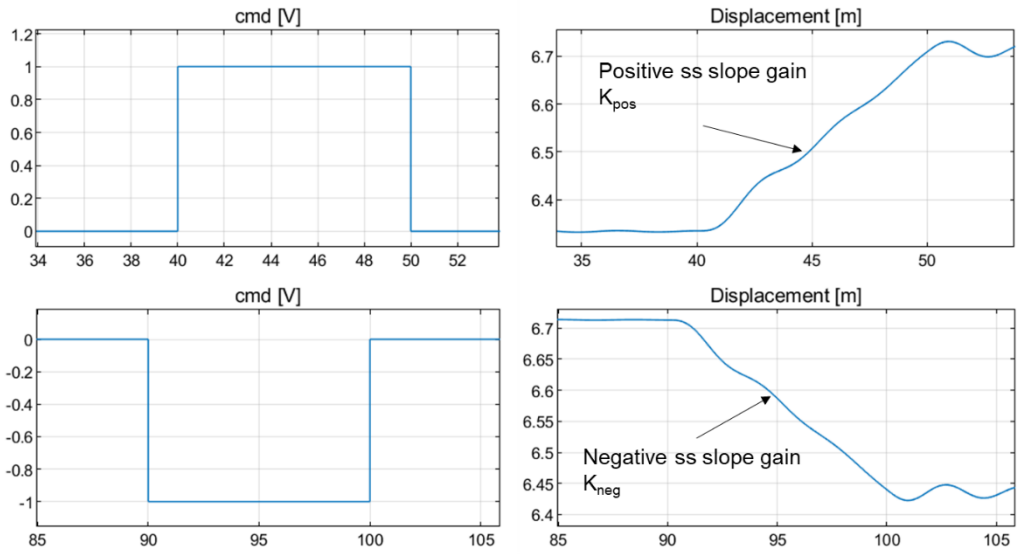

Locating the positive and negative steady-state slope gains for the feedforward controller

Steady-state slope gains are usually equal in magnitude, so will consider the absolute value of one of them in calculations:

$$K = K_{pos} = |K_{neg}|$$

6. Design the PID With Double Derivative (PIDD) Feedback Control

The unfiltered controller transfer function of the PIDD is given as:

$$C(s) = K_p + \frac{1}{s}K_i + sK_d + s^2K_{dd}$$

and the plant from before, $G = \frac{K\omega_n^2}{s(s^2+2\zeta\omega_n s+\omega_n^2)}$

The closed loop transfer function is:

$$H(s) = \frac{GC}{1+GC}$$

$$H(s) = \frac{(sK_p + K_i + s^2K_d + s^3K_{dd})K\omega_n^2}{s^4 + (2\zeta\omega_n + K\omega_n^2 + K_{dd})s^3 + (\omega_n^2 + K_dK\omega_n^2)s^2 + K\omega_n^2K_ps + K\omega_n^2K_i}$$

Note that the desired characteristic equation will not overshoot, and the response will be that of a low-pass filter's in series. The poles are placed as far as possible to the left on the z-plane so that errors and transients decay to zero as fast as possible.

- Case 1 – Fast response with PIDD

Compare the denominator of the transfer function $H(s)$ to a 4th order polynomial:

$$(s + \lambda)^4 = s^4 + 4\lambda s^3 + 6\lambda^2 s^2 + 4\lambda^3 s + \lambda^4$$

Equating the coefficients for each power of s between the actual characteristic equation and the desired characteristic equation gave the PIDD gains:

$$K_i = \frac{\lambda^4}{K\omega_n^2};\ K_p = \frac{4\lambda^3}{K\omega_n^2};\ K_d = \frac{6\lambda^2 - \omega_n^2}{K\omega_n^2};\ K_{dd} = \frac{4\lambda - 2\zeta\omega_n}{K\omega_n^2}$$

Note that the double derivative (DD) term was used to place 4 poles. The four gains are all a function of $\lambda,\ K$ and ω_n; increasing λ makes the response faster. If the open-loop gain changes, the closed-loop gains can be scaled accordingly.

The gains can be calculated to give the desired response by moving the closed loop poles to the left on the negative axis in the s plane but there are limitations.

Limitations: Control effort (saturation); Noise due to quantization, sample jitter, disturbances due to quantisation (cannot have too large K_d and K_{dd}, require filtering); Gains must be positive (limiting λ), TF zeros may give overshoot; In reality $G(s)$ is not ideal – will need retuning.

- Case 2 – Slow response with PIDD

The desired characteristic equation can be changed to two pairs of real poles (at $-\lambda$ and $-\mu$) for a slower response:

$$(s+\lambda)^2 * (s+\mu)^2 = s^4 + 2s^3(\mu+\lambda) + s^2(\mu^2 + 4\mu\lambda + \lambda^2) + 2s(\mu^2\lambda + \mu\lambda^2) + \mu^2\lambda^2$$

As before, comparing the coefficients for each power of s between $H(s)$ and the characteristic equation above, gave:

$$K_i = \lambda^2 \frac{\mu^2}{K\omega_n^2}; \quad K_p = 2\lambda\mu \frac{\mu+\lambda}{K\omega_n^2}; \quad K_d = \frac{2\lambda\mu^2 + 2\lambda^2\mu - \omega_n^2}{K\omega_n^2};$$

$$K_{dd} = 2\frac{\mu+\lambda-\zeta\omega_n}{K\omega_n^2}$$

Condition: $\lambda + \mu \geq \zeta * \omega_n$

If λ is small, μ should be large enough so that K_d and K_{dd} are not negative. However, $e^{-\lambda t}$ will take longer to decay to 0 so the response will be slower given changes in target positions and disturbances. If λ increases, then μ should decrease; the fastest response will occur when $\lambda = \mu = \frac{\zeta\omega_n}{2}$.

Generally, the slow case response gives slightly more flexibility to the design, handling some cases that would otherwise result in negative control gain.